CIRCULATION AT THE DELAWARE BAY MOUTH FROM THE LAGRANGIAN AND EULERIAN PERSPECTIVES

by

Philip A. Muscarella

A dissertation submitted to the Faculty of the University of Delaware in partial fulfillment of the requirements for the degree of in Doctor of Philosophy in Marine Studies

Spring 2011

CIRCULATION AT THE DELAWARE BAY MOUTH FROM THE LAGRANGIAN AND EULERIAN PERSPECTIVES

by

Philip A. Muscarella

Approved: _____
Charles E. Epifanio, Ph.D.
Director of the School of Marine Science and Policy

Approved: _____
Nancy M. Targett, Ph.D.
Dean of College of Earth, Ocean, and Environment

Approved: _____
Charles G. Riordan, Ph.D.
Vice Provost for Graduate and Professional Education

I certify that I have read this dissertation and that in my opinion it meets the academic and professional standard required by the University as a dissertation for the degree of Doctor of Philosophy in Marine Studies.

Signed: _____

A.D. Kirwan Jr., Ph.D.
Professor in charge of dissertation

I certify that I have read this dissertation and that in my opinion it meets the academic and professional standard required by the University as a dissertation for the degree of Doctor of Philosophy in Marine Studies.

Signed: _____

B.L. Lipphardt Jr., Ph.D.
Member of dissertation committee

I certify that I have read this dissertation and that in my opinion it meets the academic and professional standard required by the University as a dissertation for the degree of Doctor of Philosophy in Marine Studies.

Signed: _____

F. Veron, Ph.D.
Member of dissertation committee

I certify that I have read this dissertation and that in my opinion it meets the academic and professional standard required by the University as a dissertation for the degree of Doctor of Philosophy in Marine Studies.

Signed: _____

K.C. Wong, Ph.D.
Member of dissertation committee

I certify that I have read this dissertation and that in my opinion it meets the academic and professional standard required by the University as a dissertation for the degree of Doctor of Philosophy in Marine Studies.

Signed: _____

P.M. Kosro, Ph.D.
Member of dissertation committee

ACKNOWLEDGMENTS

Support for this research came from the Delaware Sea Grant, the University of Delaware College of Marine and Earth Studies, and the Mary A. S. Lighthipe endowment to the University of Delaware. Operation of the Delaware Bay HF radars is supported by the National Oceanic and Atmospheric Administration and the Mid–Atlantic Coastal Ocean Observing Regional Association. I would like to thank M. Whitney for providing M2 tidal ellipse data from his Delaware Bay model, and for insightful discussions regarding comparisons with HF radar tidal fits. In addition, I thank J. Kirby for providing parallel computing resources for the WRF calculations. The WRF input data for this study are from the Research Data Archive (RDA) which is maintained by the Computational and Information Systems Laboratory (CISL) at the National Center for Atmospheric Research (NCAR). NCAR is sponsored by the National Science Foundation (NSF). The original WRF input data are available from the RDA (http://dss.ucar.edu) in dataset number ds609.2. I would like to acknowledge Neil P. Barton, Christopher Hughes, and Dana Veron for running the WRF model and freely providing the data. We also thank Rich Pawlowicz for providing the freely available M_MAP and T_TIDE Matlab toolboxes used here. Finally, we are pleased to acknowledge insightful discussions with F. Pimenta, Ana E. Rice, James Mueller, Lauren Brown, and Joseph Senne. Thank you to my advisors Bruce and Denny who have provided me with direction over the last five years. I must also give the a huge thank you to my parents who always encouraged me to ask as many questions as possible. Lastly, let me thank my wife,

Lyndsey, whose words have given me support and whose love has brightened my days.

TABLE OF CONTENTS

LIST OF FIGURES

LIST OF TABLES

ABSTRACT

A consistent picture of the circulation of the Delaware Bay estuary and adjacent inner shelf established in the literature is based on a synthesis of mooring and hydrographic data complemented by elegant theoretical analyses. Because of the highly variable and episodic nature of the flow at the Delaware Bay mouth, a synoptic picture of the flow has been elusive. The advent of high-frequency (HF) radars for routine monitoring of coastal surface currents (developed over the past twenty years) offers a unique opportunity to provide synoptic descriptions of complex time-dependent flows like those that exist at estuarine mouths. Synoptic measurements lend themselves to examinations from a dual perspective, taking advantage of Lagrangian and Eulerian methods.

Here we analyze synoptic, high-resolution surface winds and currents in the Delaware Bay mouth. Two high-frequency radars measured the surface currents while the surface winds were extracted from a data-assimilating regional wind model. The large-scale characteristics noted by previous workers are clearly corroborated. Specifically the M2 tide dominates the surface currents, and the Delaware Bay outflow plume is clearly evident in the low frequency currents. Several new aspects of the surface circulation were also identified. These include a map of the spatial variability of the M2 tide (validating an earlier model study), persistent low-frequency cross-mouth flow, and a rapid response of the surface currents to a changing wind field. However, strong wind episodes did not persist long enough to set up a sustained Ekman response.

In addition to the Eulerian results presented here, several Lagrangian analyses were conducted. The approach used here calculates simulated trajectories from an archive of gridded synoptic velocities from HF radar measurements. Lagrangian methods are the best tool for examining the advective transport at the Delaware Bay mouth. There was an observed rapid separation of progressive vector diagrams (PVDs) with trajectories implying limited utility over long time scales. Synoptic Lagrangian maps (SLMs) such as residence time, escape fate, and origin showed clear dependence on tidal forcings. Blob simulations have provided a visualization tool able to examine deformation processes on a finite area of ocean.

The most significant result might be the examination of a persistent cross-mouth sub-tidal flow that may be a result of non-local advection from the New Jersey shelf. This feature is not well documented in the literature and we make a first attempt to describe its characteristics.

Chapter 1

INTRODUCTION

1.1 Background

The Delaware Bay estuary is one of the largest along the U.S. east coast. It is 45 km wide at its widest point and approximately 210 km from the head of the Delaware River to its mouth. The bay mouth, from Cape Henlopen, Delaware to Cape May, New Jersey, is 18 km wide. The estuary has a mean depth of 7 m and a maximum depth of approximately 30 m within a deep channel at the southern side of the bay mouth. Over eight million people live within the Delaware River watershed. It also is a major shipping hub, with 4200 commercial ship visits each year spread out over nine ports in three states. Most importantly, it is responsible for a significant fraction of the transport of freshwater and associated terrestrially–derived material to the ocean along the Atlantic seaboard. Because of its economic importance and rather unique hydrological characteristics, it is important to pursue improved understanding of its circulation.

Most of what we now know about the circulation of Delaware Bay is due to R. Garvine and coworkers. In a series of papers extending over twenty years, they developed a picture of the circulation of the Bay estuary and adjacent inner shelf. Their picture was based on a synthesis of mooring and hydrographic data complemented by elegant theoretical analyses. Hence, most of the knowledge of the circulation is based on fixed-point (moorings and hydrography) ocean measurements, although there were a limited number of drifter studies, such as Pape and Garvine

(1982) and Sanders and Garvine (2001). These observations are typical of virtually all coastal zones and, for Delaware Bay, provide a consistent general picture of the circulation. However, these data do not provide synoptic pictures, either of horizontal variability scale or of sub-tidal ocean circulation features.

The most pronounced features of Delaware Bay are the semi-diurnal tides and the outflow plume. Tidal currents at the mouth of the Bay can exceed 100 cm s^{-1}. Amplification of tidal currents is typical of coastal plain estuaries, such as the Delaware and the Chesapeake. Of course, the tides are caused by precise periodic astronomical forcing. However, the currents also respond to the complex bottom topography, coastline features, and other shelf processes. This spatial structure of tidal currents is not well understood.

The primary goal of this research has been to describe the currents at the Delaware Bay Mouth using both Eulerian and Lagrangian techniques. This collaboration of perspectives allows for the understanding of spatial current structures. It is best said by Neumann (1968), "The most complete description of oceanic currents is obtained from a combination of both Eulerian and Lagrangian methods."

1.2 Circulation at the Delaware Bay Mouth

Prior work in Delaware Bay and adjacent coastal waters identified three dominant forcing mechanisms typically associated with estuarine–ocean exchange: tides, buoyancy–driven flow, and winds. From 53 current meter records, Münchow *et al.* (1992) reported that the M2 tide explains about 90% of the tidal current kinetic energy variance. Their M2 tidal ellipses showed significant spatial variability near the bay mouth with decreasing major axes and reduced ellipticity moving seaward. They also estimated the continuous M2 volume flow through the bay mouth as approximately 1.9 x 10^5 m^3 s^{-1}. The resulting ratio of M2 volume flow to average freshwater inflow is approximately 260, suggesting minimal stratification throughout most of the year. Whitney and Garvine (2008) codified these results in a model

for estimating tidal current amplitudes.

Pape and Garvine (1982) used surface and subsurface drifters near the Delaware Bay mouth to document a classical, two–layer estuarine flow (near–surface outflow and inflow near the bottom). Garvine (1991) found a strong outflow plume along the southern bay mouth and some evidence of cross-channel flow along the mouth using current meters and hydrography. Later Münchow(1992), Münchow and Garvine (1993), Wong and Münchow (1995), and Avicola and Huq (2002) reported on plume dynamics. Whitney (2003) provided an excellent review of these studies.

Whitney (2003) also made an ambitious attempt to summarize how tides, buoyant flow, and winds affect the circulation of Delaware Bay and exchange with the coastal ocean. That effort was extended by Whitney and Garvine (2006) who compared model simulations with observations from the spring of 1993 and 1994. The observations included salinity climatology, freshwater outflow from stream gauges, hydrographic observations of the salinity in the plume and coastal current, and some surface drifter data.

The complexity of the circulation of the Delaware Bay may not come out in this relatively brief background. The highly irregular coastline, rugged topography, and highly variable freshwater input all conspire to amplify the complicated nature of the circulation in this region. Figure 1.1 shows the variability of the freshwater outflow from the Delaware River. The magnitude, as well as the timing of these huge pulses of freshwater, significantly influence the buoyancy driven circulation along the length of the estuary. Notice the high amount of variance between the yearly inputs of freshwater. This episodic nature, seen as a feature in the discharge, is fundamental in characterizing the flow. Non–linear effects due to barotropic and internal tides encountering steep bottom slopes could also be affecting the flow, but this has yet to be determined.

The majority of published work related to Delaware Bay circulation was completed over the last three decades and based almost entirely on relatively short ocean time series measurements from sparse, fixed locations. Much of this work also used wind measurements, mostly over land, supplemented by measurements from a few offshore buoys near the bay, but outside its mouth. The historically sparse, intermittent ocean sampling is typical of virtually all coastal zones, and, for Delaware Bay, was sufficient to provide a consistent general picture of the ocean circulation and the role of near–surface winds. However, these historical measurements were poorly resolved in space and could only account for processes occurring when the measurements were made. Consequently, they are insufficient for addressing questions related to the scales of spatial and temporal variability. In other words, these types of historical coastal observations work fairly well when the time and space scales of the energetic motions are huge, but tend to fail in the presence of localized episodic events, such as those seen at the mouth of the Delaware Bay.

1.3 Winds Over the Delaware Bay

Understanding the effects of winds on Delaware Bay sub-tidal circulation has been guided by the early theoretical analysis of Garvine (1985). He developed a model that partitioned the ocean response into locally and remotely forced components. The local response is due to the direct influence of local wind stress on the estuary, while the remote response is driven by a sea level change set up by Ekman transport due to large–scale (non–local) atmospheric processes. He showed that for Delaware Bay the remote response dominates and is generally opposite to the local response. This analysis was extended by Münchow and Garvine (1993), Wong (1999), and Janzen (2000).

More recently, the Delaware Bay has received attention due to the presence of the Sea Breeze phenomenon. This atmospheric circulation pattern is thermally

driven by an uneven distribution of heating between the land and sea. The differences in pressure then cause the cool marine air near the surface to move landward. This effect is present mostly in the summer months. A brief summery of this process is found in Hughes and Veron (2010).

1.4 Describing Ocean Flows: Eulerian Vs. Lagrangian Perspectives

In general, there are two equivalent descriptions of the motion of a fluid: 1) Lagrangian and 2) Eulerian. The Lagrangian description depicts the trajectories of fluid particles i.e. their origin and fate while the Eulerian description describes the speed and direction of the fluid at specific locations.

The motion of a fluid particle or parcel is obviously governed by Newton's second law of motion, taken here from Dutton (1976), to be

$$\frac{\mathrm{du}}{\mathrm{dt}} = F_x, \frac{\mathrm{dv}}{\mathrm{dt}} = F_y, \frac{\mathrm{dw}}{\mathrm{dt}} = F_z. \tag{1.1}$$

Here the particle's acceleration per unit mass is acted upon by the components of force F_x, F_y, and F_z.

Figure 1.2 shows how the Eulerian and Lagrangian perspectives arise from the equations of motion. Using Newton's second law as a starting point, the first integration produces the Eulerian velocities at specific points in space. A typical Eulerian question that is applicable to the Delaware Bay is, "What are the forces (currents) that act on the piling of a wind turbine?" The second, less appreciated, integration yields particle trajectories, the Lagrangian perspective. An appropriate Lagrangian question is, "Where does an oil spill go and what path does it take?"

Euler's contribution to fluid mechanics has been referred to as the most important achievement of fluid mechanics. Truesdell (1954) describes this as "In the older researches the description of the motion is rather assumed than constructed,

but Euler before stating any physical assumptions formulated the concept of a continuous medium and analyzed the pure geometry of its motion, or kinematics, with such thoroughness that little was added to this discipline until the work of Cauchy seventy years later." In this case the Euler relation is used to expand the total derivative of equation 1.1 to apply the equation to a point in space,

$$\begin{aligned} \frac{\partial u}{\partial t} + u\frac{\partial u}{\partial x} + v\frac{\partial u}{\partial y} + w\frac{\partial u}{\partial z} &= F_x \\ \frac{\partial v}{\partial t} + u\frac{\partial v}{\partial x} + v\frac{\partial v}{\partial y} + w\frac{\partial v}{\partial z} &= F_y \\ \frac{\partial w}{\partial t} + u\frac{\partial w}{\partial x} + v\frac{\partial w}{\partial y} + w\frac{\partial w}{\partial z} &= F_z. \end{aligned} \tag{1.2}$$

Equations 1.1 and 1.2 contrast the Lagrangian and Eulerian dynamic balances respectively. Equation 1.1 allows for the tracking of particles as they move through a fluid, while equation 1.2 applies Newton's second law to a fixed position. The far reaching implications of Euler's simplification are essentially responsible for the modernization oceanographic observation. Historical measurements were made mostly at fixed points; thus it was logical to use Euler's equations of motion, even though they are in a nonlinear form. This choice meant confronting the fundamental nonlinearity rather than tracking particles.

Eulerian measurements made the earliest contributions to modern oceanography. Advances in technology have resulted in the deployment of large numbers of current measurement systems. These devices provide a time series of velocity vectors at fixed locations. The vast majority of models and observational data have been Eulerian in nature, but many users want to know where particles go and how they get there, i.e. the Lagrangian character of the flow. These transport questions are best answered with Lagrangian tools. Eulerian fields are "one integration short"

of providing path related quantities. This has become painfully clear with the occurrence of the Deepwater Horizon oil spill in 2010 where pathways and transport quantities were required.

Synoptic velocity fields are the ideal tools to look at these varying perspectives. They are simply velocity fields in x,y,z and time. We are entering a period of oceanography where more synoptic information is available than ever before. Although, Eulerian, these fields are the key to analyzing Lagrangian data.

Lagrangian measurements help physical oceanographers to provide a first–order description of the global ocean circulation. It is very appealing to track a parcel of water in order to gain insight into the processes that affect its evolution. These processes include the advective and non–advective transport of substances discharged into the ocean. The earliest Lagrangian measurements only allowed for researchers to track particles for short periods of time, but with the advancement of satellite communication the length of time for tracking drifters or submerged floats is limited only by the system's battery power.

The early development of Eulerian measurement techniques out paced the Lagrangian methods. However, in recent years, there has been wider usage of Lagrangian analysis methods. Most studies focus on either Eulerian or Lagrangian measurement tools while neglecting the other. Here, we show that the combined affect of Eulerian and Lagrangian analyses can produce new insight into ocean dynamics.

1.5 Questions to be Explored

The results presented here are divided into Eulerian and Lagrangian perspectives. These analyses will focus on a variety of questions posed here, examined in the chapters and discussed in the conclusions.

The Eulerian questions are :

1) Can we identify and characterize dynamical processes with the use of a synoptic data set?

2) What is the spatial distribution of the high and low frequency currents at the mouth of the Delaware Bay?

3) Does our 2D synoptic description of the tides fill in the spatial gaps present in other studies?

4) Is there a detectable wind response in the surface current record?

5) Is the cross–mouth current a persistent sub–tidal feature and, if so, what are some of its characteristics?

The Lagrangian questions are :

1) What is the appropriate time scale for the usefulness of progressive vector diagrams for studying coastal ocean transport?

2) What are typical forward and backward residence times, particle origins and escape fates at the Delaware Bay mouth and how do these values vary in space?

3) What are the forcing mechanisms that affect these residence time results?

4) Can we use a blob–loop method to calculate kinematic parameters of the velocity fields and does it produce results similar to a finite difference method?

5) What does the evolution of these blobs tell us about the characteristics of the velocity fields at the Delaware Bay mouth?

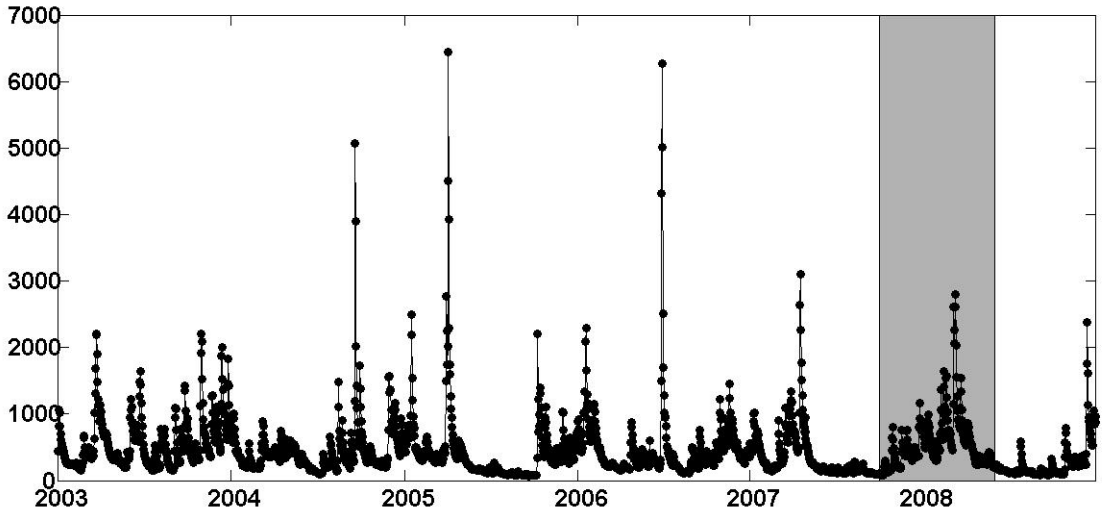

Figure 1.1: Five year long time series of Delaware River flow rate in $m^3\ s^{-1}$. Shaded region represents high–frequency radar analysis period.

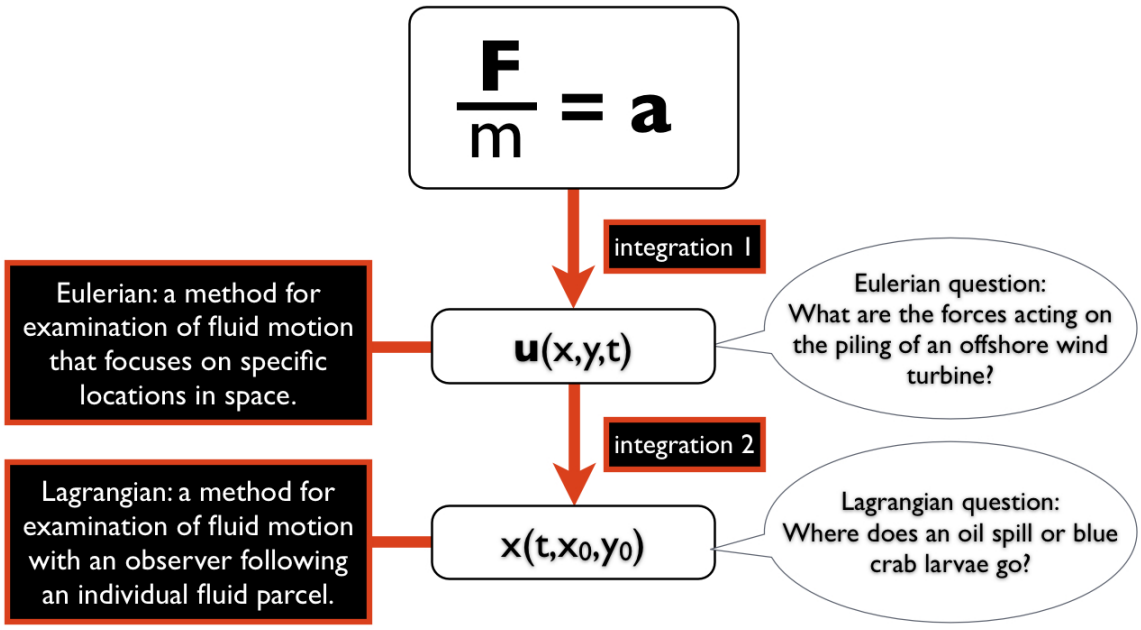

Figure 1.2: Flow chart depicting the integration steps needed to reach the Eulerian and Lagrangian flow perspectives.

Chapter 2

DATA SOURCES

2.1 Freshwater Flow at Trenton

According to Sanders and Garvine (2001) the United States Geological Survey (USGS) Delaware River discharge record (Trenton, New Jersey) provides a good measure of river flow, and is proportional to outflow at the bay mouth. The freshwater flow of the Delaware River has been measured at this location for over a hundred years. Figure 1.1 shows a five year long time series of the river discharge. This time series shows episodic events of high river outflow that are associated with spring runoff. Some years are much higher than others. This speaks to the highly episodic nature of the Delaware Bay circulation. The time period of outflow we are interested in can be seen in the shaded regions of figure 2.1. This time series of outflow is used to isolate the high and low discharge from the Delaware River. We chose two periods in order to examine the importance of freshwater flux into our study region. These time periods are a low–outflow period from 1 October to 14 November 2007 and a high–outflow period from 3 March to 16 April 2008.

2.2 Station Winds Over Water

Figure 2.2 shows two anemometer weather stations. These metrological stations report five minute wind measurements. There are stations at the Lewes and Cape May ferry terminals but these locations can cause biasing of the wind measurements when the ferries enter and exit the terminals. The offshore station is a NOAA

metrological buoy 44009 which represents the only wind measurement reasonably close to our study region. The Brandywine station is located on the Brandywine light house out in the middle of the Delaware Bay, and has periods of data loss during our analysis time intervals.

2.3 Synoptic Winds from the Weather Research and Forecasting (WRF) Model

This section on winds is taken from Muscarella *et al.* (2011).

For synoptic winds over the Delaware Bay we used the Advanced Research version of the Weather Research and Forecasting (WRF) (http://wrf-model.org) model version 2.2 (Skamarock *et al.*, 2007; Wang *et al.*, 2007). WRF is a numerical weather prediction system designed to serve both operational forecasting and atmospheric research needs at scales from 300 m to 1000 km. This regional–scale atmospheric model was jointly developed by many weather forecasting and atmospheric climate modeling communities.

WRF features modern radiation and land surface parameterizations as well as three-dimensional data assimilation. In this study, the Rapid Radiative Transfer Model (RRTM) longwave radiation parameterization (Mlawer *et al.*, 1997) and short wave radiation parameterization (Dudhia, 1989) are used to represent atmospheric radiative transfer. The planetary boundary layer (PBL) and turbulence processes are represented by the Mellor–Yamada–Janjic Yonsei (MJY) University PBL scheme (Hong *et al.*, 2006). The tendencies calculated at each location by the MYJ scheme depend only on the local properties of the flow. This PBL scheme has been shown to produce more accurate surface winds over the ocean near Korea and Japan relative to other PBL parameterizations in WRF (Kwun et al. 2009).

WRF also uses a surface layer parameterization to calculate friction velocities and exchange coefficients for surface heat and moisture fluxes. The layer next to the surface is a traditional Monin–Obukhov surface layer. Between this layer and the

first PBL layer is a surface layer parameterization that uses the National Centers for Environmental Prediction (NCEP) Eta similarity theory scheme (Janjic 1994). Land surface processes are represented by the multilayer Noah surface model (Pan and Mahrt, 1987; Chen and Dudhia, 2001; Ek *et al.*, 2003; Holt *et al.*, 2006) to provide heat and moisture fluxes to the PBL scheme.

Regional weather forecast models have been used to study the influence of surface forcing on coastal winds for at least 40 years (McPherson, 1970; Ohashi and Kid, 2002; Thompson *et al.*, 2007). Regional atmospheric models have also been used to investigate the influence of urban surfaces, or modification of land surfaces, on weather patterns (Kabat, 2004), and climate (Pielke, 2001; Klingaman *et al.*, 2008). WRF, in particular, was recently used to investigate sea breeze effects and the atmospheric impact on CO_2 fluxes (Ahmadov *et al.*, 2007), the transport of ozone (Darby *et al.*, 2007), and as a model for low–level meridional circulation (Nolan *et al.*, 2007).

Correctly simulating low–level winds along coastlines is one of the challenges of current mesoscale and regional–scale atmospheric modeling. Consequently, a coastal mesoscale atmospheric model must be carefully assessed. This can be especially challenging for wind–current interaction studies, since wind observations, while typically numerous over land, are sparse over water. Darby *et al.*(2007) used WRF and Penn State's fifth generation meso-scale model (MM5) to look at the impact of sea breeze circulation on ozone transport. Over several days, WRF predicted the onset of the sea breeze slightly early or on time when compared with lidar observations. However, both WRF and MM5 wind speeds were high relative to observations, and more significantly, both models demonstrated reduced predictive skill when local–scale meteorological events were dominant. During the Carbon Europe Regional Experiment Study (CERES), comparisons between WRF wind

profiles and radiosonde launches over southern France showed that the model accurately predicted wind speed and direction in the mornings, with some disagreement in direction in the afternoon when local forcing dominated (Ahmadov *et al.*, 2007).

Here, WRF was forced with coarse–scale information from NCEP's North American Model (NAM) which has a spatial resolution of 40 km and a temporal resolution of six hours. Our Delaware Bay simulations use three nested domains (see Fig. 2.4) with spatial resolutions of 9 km (outer nest), 3 km (middle nest), and 1 km (inner nest). The spatial resolution of the land surface is 30 seconds for the two inner nests. The outer nest (Fig. 2.4, region 1) is sized to capture synoptic storms that may affect Delaware Bay. The middle nest (Fig. 2.4, region 2) covers the entire Delaware Bay, and the inner nest (Fig. 2.4, region 3) includes the entire HF radar measurement footprint.

Overlapping five–day WRF runs covered two analysis periods: October 1 through November 14, 2007 and March 3 through April 16, 2008. The first day of each five–day run was discarded as spin–up and the start of each run overlapped the previous run by one day. Winds at 10 m were archived hourly.

2.4 ADCP Currents

Deployment	Longitude	Latitude	Depth (m)	Start	End
A	-75.0648	38.7750	9.1	Oct. 26, 2007 0000 GMT	Nov. 29, 2007 1100 GMT
B	-74.9610	38.8610	8.9	Apr. 9, 2009 1500 GMT	May 12, 2009 1200 GMT
C	-74.9260	38.8400	11.2	Apr. 9, 2009 1600 GMT	May 12, 2009 1300 GMT

Table 2.1: Table of ADCP deployments.

Three Teledyne RD Instruments 600 KHz ADCPs were deployed at the mouth of the Delaware Bay within the HF radar footprint (table 2.1, figure 2.2). These ADCPs are being used for comparison with a near surface current comparison (section 3.2) and to show the barotropic nature of the water column (section 4.2.3). For each deployment, the ADCPs used a vertical resolution (bin size) of 0.5 meters and a sampling interval of five minutes. The bin containing the free surface for each profile was determined using a received signal strength indicator bump detection algorithm to identify the spike in reflected acoustic energy. The velocities from the ADCPs are rotated by 12 degrees to account for the local magnetic declination. For comparison with the HF radar measurements, ADCP velocities from the bin one meter below the instantaneous free surface were used, since they consistently had a high signal–to–noise (SNR) ratio, and were below the surface layer susceptible to acoustic side lobe contamination (Teledyne, 2006).

2.5 High–Frequency Radar Currents

Over the last two decades, oceanographers have mapped surface currents by measuring Doppler shifted backscatter using HF radars. See Paduan and Graber (1997) for an accessible discussion of HF radar theory. These measurements have significant advantages over traditional measurements from moorings and ship mounted acoustic Doppler current profilers (ADCPs) as they provide high–resolution synoptic coverage on hourly time scales and are amenable to routine monitoring. This allows for the availability of long time series of synoptic velocities. Their chief limitation is that they only measure currents near the ocean surface.

As HF radar has emerged as the major sensor for synoptic current mapping, a number of studies have compared these measurements with ADCPs, current meters, and Lagrangian drifters (Chapman and Graber, 1997; Chapman *et al.*, 1997; Graber *et al.*, 1996; Kohut *et al.*, 2006; Paduan *et al.*, 2006; and Ohlmann *et al.*, 2007). These studies of HF radar vs. point measurements report root mean squared (RMS)

differences of 7–19 cm s^{-1}. Ohlmann *et al.* (2007) reported differences of 3–5 cm s^{-1} between HF radar measurements and velocities derived from clusters of drifter trajectories in the Santa Barbara Channel. They also present an excellent summary of published HF radar assessment studies and a detailed discussion of the possible sources of differences between HF radar measurements and those of other sensors.

Since HF radar measurements are averaged over time scales of 1–3 hours and space scales of 1-10 km (ocean areas of 1-100 km^2), the measurements include contributions from real ocean variability over these time and space scales. As a result, comparisons with independent point measurements (from ADCPs, current meters, or drifter trajectories) must be interpreted with care, since these sensors average over much smaller space and time scales.

Particularly relevant to this study is that of Skarke *et al.* (2008) who compared HF radar measurements with near–surface velocities from a bottom mounted ADCP during October–November 2007, just south of the Delaware Bay mouth near the edge of the radar analysis region. They reported complex correlation amplitudes greater than 0.9 with mean direction differences of 0.3 to 0.6 degrees and root mean squared (RMS) differences of 14–22 cm s^{-1}.

As oceanographers have gained confidence in the reliability of HF radars, a significant number of studies based on these measurements have emerged over the last decade. Shay *et al.* (2001) gave a detailed analysis of the M2 tide at the Chesapeake Bay mouth. Beckenbach and Washburn (2004) used three years of HF radar measurements to describe intermittent low–frequency waves propagating through the Santa Barbara Channel. In Monterey Bay, Lagrangian analyses of HF radar measurements have been used to study surface transport (Lipphardt *et al.*, 2006; Coulliette *et al.*, 2007).

The surface current measurements used here come from two standard–range, 25 MHz radars. These radars are both SeaSonde–type Coastal Ocean Dynamics

Applications Radars (CODAR). The southern site is located at Cape Henlopen, DE, while the northern site is on the southern tip of Cape May, NJ (see Fig. 2.5). Since a single radar measures only the surface velocity component along a radial originating from the antenna, total vector current maps require a minimum of two radars. Moreover, the velocity component perpendicular to the baseline between two antennas cannot be resolved. For this reason, surface currents near the baseline between the two Delaware Bay radars are not used here.

Ideal antenna patterns were used to produce separate maps of radial velocities at each site. These radial velocities were combined to produce total velocities on a grid with 1.5 km resolution. At each grid point, all radial velocities from both sites within a 3 km radius are objectively fit using least–squares to produce a total velocity vector. Total velocity maps were created hourly.

This network has been operational since December 2006. The data used in the subsequent analyses are from three distinct time periods seen in table 2.2. Environmental factors influence the spatial extent of the total velocity measurement footprint over time, and occasional gaps within the footprint do occur. See Paduan and Rosenfeld (1996) for a detailed explanation. To minimize the effects of temporal gaps, we restricted our analysis to grid locations that had at least 80% coverage in time over the analysis period. An example of the hourly HF radar surface current maps is shown in Figure 2.5. Several gaps are seen along the outer edge of the measurement footprint. Figure 2.6 shows the percent coverage in time for the radar grid, the grid points with at least 80% coverage in time, and the mean velocities at these locations for analysis period 1.

In addition, to the spatial gaps within the hourly maps, an equipment failure at Cape May from 3 December 2200 GMT to 20 December 1300 GMT prevented any HF radar measurements. For December 2007, then, the monthly mean flow was computed for each grid point with at least 40% coverage in time. Figure 2.7 shows

Period	Start	End
1	Oct. 1, 2007 0000 GMT	May 31, 2008 2300 GMT
2	Sep. 1, 2008 0000 GMT	Sep 30, 2008 2300 GMT
3	Apr. 9, 2009 1600 GMT	May 12, 2009 1300 GMT

Table 2.2: Table of HF radar time periods.

the temporal coverage of the radar sites throughout time period 1, the equipment failure is easily seen in the record.

2.5.1 HF Radar Errors

Several sources of uncertainty can conspire to degrade total velocities computed by combining measured radial velocities from two or more radar sites. Geometrical dilution of precision (GDOP), which increases as the look angles from multiple radars begin to deviate from orthogonality, can amplify small uncertainties in measured radials. Spatial variability within the averaging circle used to combine radials also adds to uncertainty. Spatial coverage of radials also decreases with increasing range from the antenna due to the non-uniformity of the polar coordinate grid. Temporal variability over the averaging time window can contribute errors to measurements. The isolation of these sources of error from true measurement error will remain a goal for the HF radar community in the short term.

2.5.1.1 Geometric Dilution of Precision

GDOP is well known in the radar community to be the cause of the uncertainties in the measurements in a baseline region (area between two sites). While the principle is well known, very few fully understand its influence in introducing

errors into measurements. A simple definition would state that GDOP is a dimensionless coefficient of uncertainty which relates the effect that station geometry has on current measurement.

Next, we look at an example laid out by Barrick (2002). Figure 2.8 assumes two radar measurements of vector components (m_1 and m_2) which can be radials, the total velocity is $\mathbf{w}$, and the normals along the radar-measured components ($\mathbf{n}_1$ and $\mathbf{n}_2$). Assume the baseline lies along x axis. The total velocity is unknown. We have two linear equations:

$$\begin{aligned} m_1 &= n_{1x}u + n_{1y}v, \\ m_2 &= n_{2x}u + n_{2y}v, \end{aligned} \tag{2.1}$$

with solutions of:

$$\begin{aligned} u &= \frac{n_{2y}m_1 - n_{1y}m_2}{n_{1x}n_{2y} - n_{2x}n_{1y}}, \\ v &= \frac{n_{1x}m_2 - n_{2x}m_1}{n_{1x}n_{2y} - n_{2x}n_{1y}}. \end{aligned} \tag{2.2}$$

The denominator is the sine of the angle between $\mathbf{n}_1$ and $\mathbf{n}_2$ and is related to GDOP and can be seen in a general sense as a gross measure of the stability of $\mathbf{w}$. Next, it is required to assign the same uncertainty or random error to m_1 and m_2. This is because without some measure of error, GDOP is meaningless. One can estimate u and v exactly right up to the parallel condition if there is no measurement error. After several assumptions to simplify the system the u, v and $\mathbf{w}$ variances

are:

$$\sigma_u^2 = \frac{n_{2y}^2 + n_{1y}^2}{|n_{1x}n_{2y} - n_{2x}n_{1y}|^2}\sigma^2,$$
$$\sigma_v^2 = \frac{n_{2x}^2 + n_{1x}^2}{|n_{1x}n_{2y} - n_{2x}n_{1y}|^2}\sigma^2,$$
$$\sigma_w^2 = \sigma_u^2 + \sigma_v^2 = \frac{2\sigma^2}{|n_{1x}n_{2y} - n_{2x}n_{1y}|^2}. \tag{2.3}$$

Again the denominator, or the sine of the angle between the lines from the radar sites to some observation point, can cause the GDOP to become infinite at 0 or 180 degrees. It is suggested that GDOP acceptability thresholds be setup to allow for range of uncertainty within the measurements.

Figure 2.9 shows the GDOP values for the Delaware Bay HF radar sites. The red values represent areas where the crossing angles are small so the GDOP will amplify the uncertainty in the measurements. The areas of high GDOP are isolated to the baseline region, down in the southwestern portion of the domain, and far away from the sites.

2.5.1.2 Antenna Pattern Issue

SeaSonde–type HF radar receive antennas can be sensitive to distortion from nearby objects, and the accuracy of their measurements is most often improved by measuring the antenna response pattern (Paduan *et al.*, 2006). The antenna patterns for the Cape May and Cape Henlopen sites were measured in September 2007 and found to be nearly ideal. However, when the measured pattern was used to reprocess data at the Cape Henlopen site, azimuthal gaps occurred, resulting in significant data loss. Since the cause of this spokiness in azimuthal coverage is due to small scale roughness in the measured antenna pattern, ideal antenna patterns were used for all HF radar measurements described here.

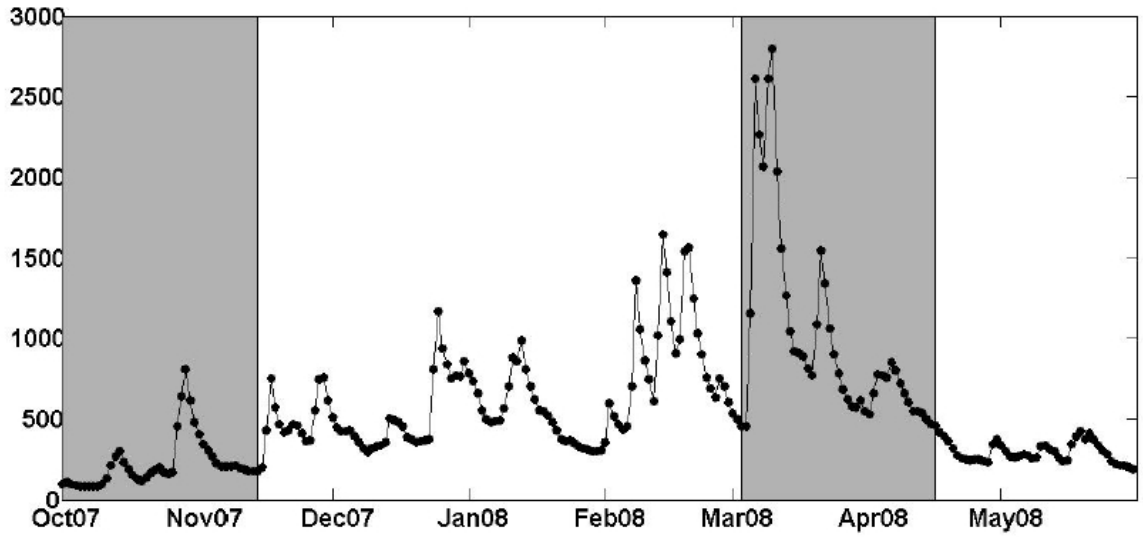

Figure 2.1: Time series of Delaware River flow ($m^3\ s^{-1}$) measured near Trenton, New Jersey for October 2007 through May 2008. The low-flow (October 2007-November 2007) and high-flow (March 2008-April 2008) periods are highlighted in grey.

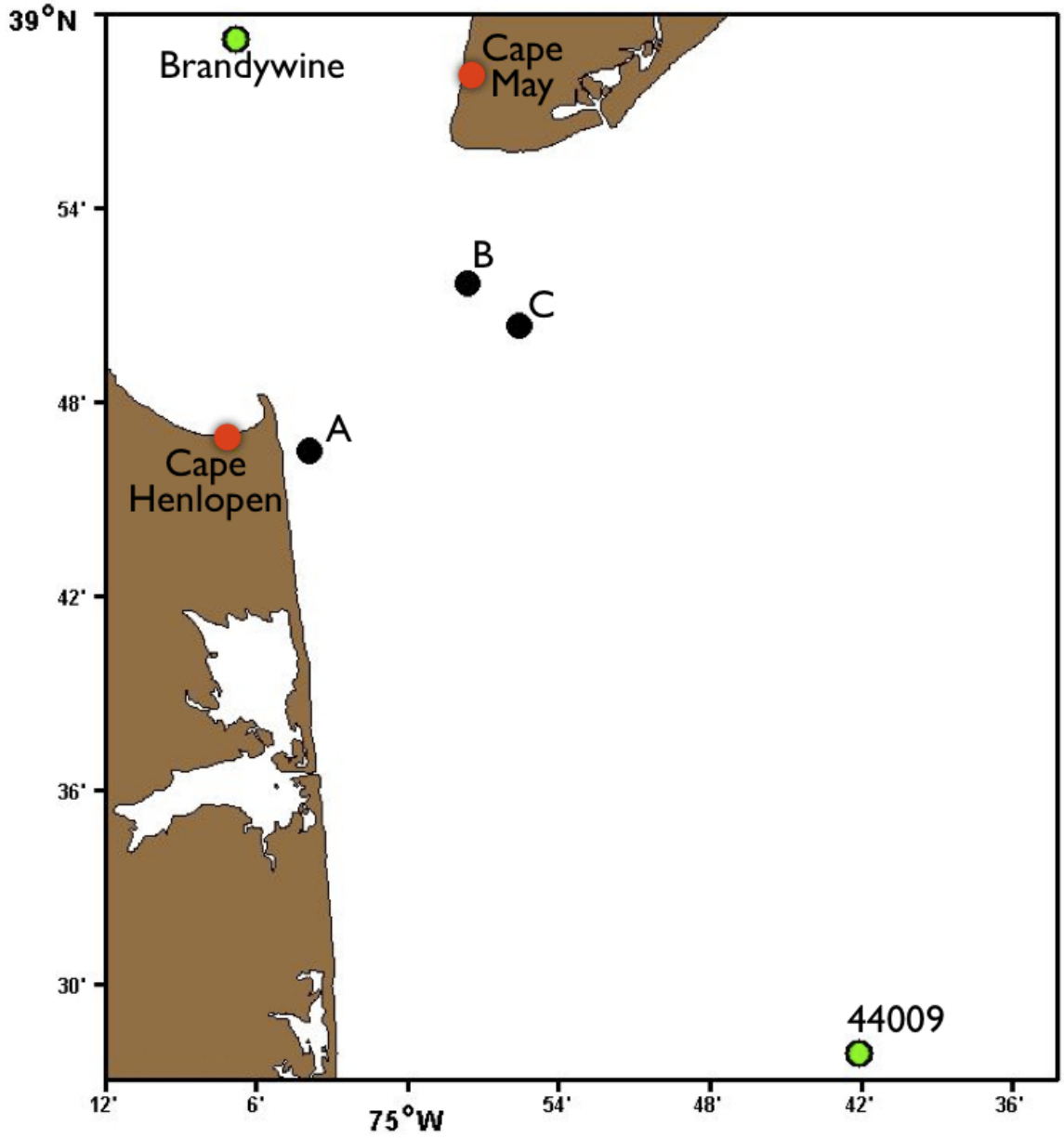

Figure 2.2: Map of ADCP deployments (black dots), wind stations (green dots), and ferry terminals (red dots).

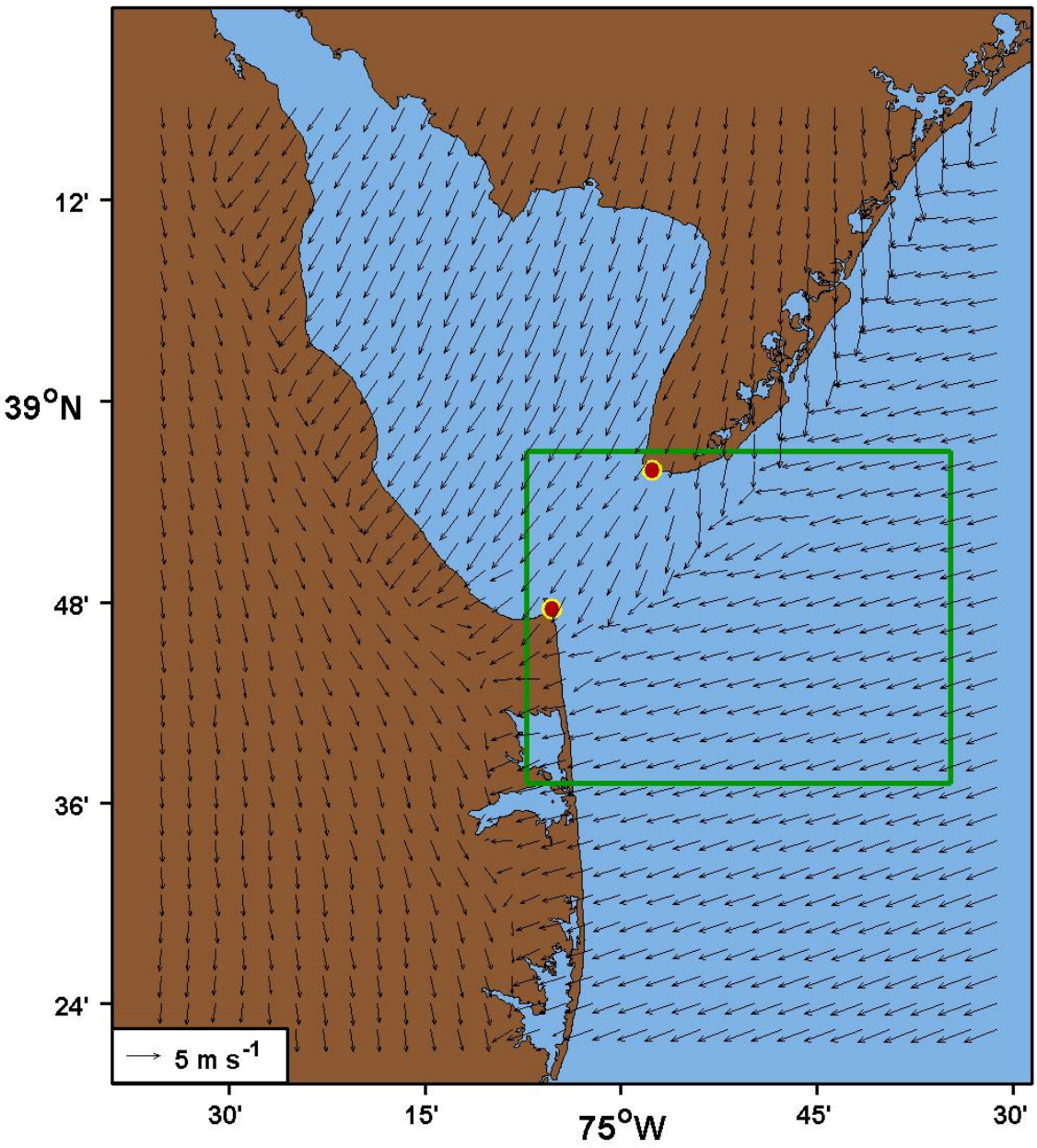

Figure 2.3: Example WRF model winds. Every third wind vector is shown, for clarity. The green box shows the limits of the geographic region relevant to this study. Here conditions are shown for 1 October 2007, 1000 GMT.

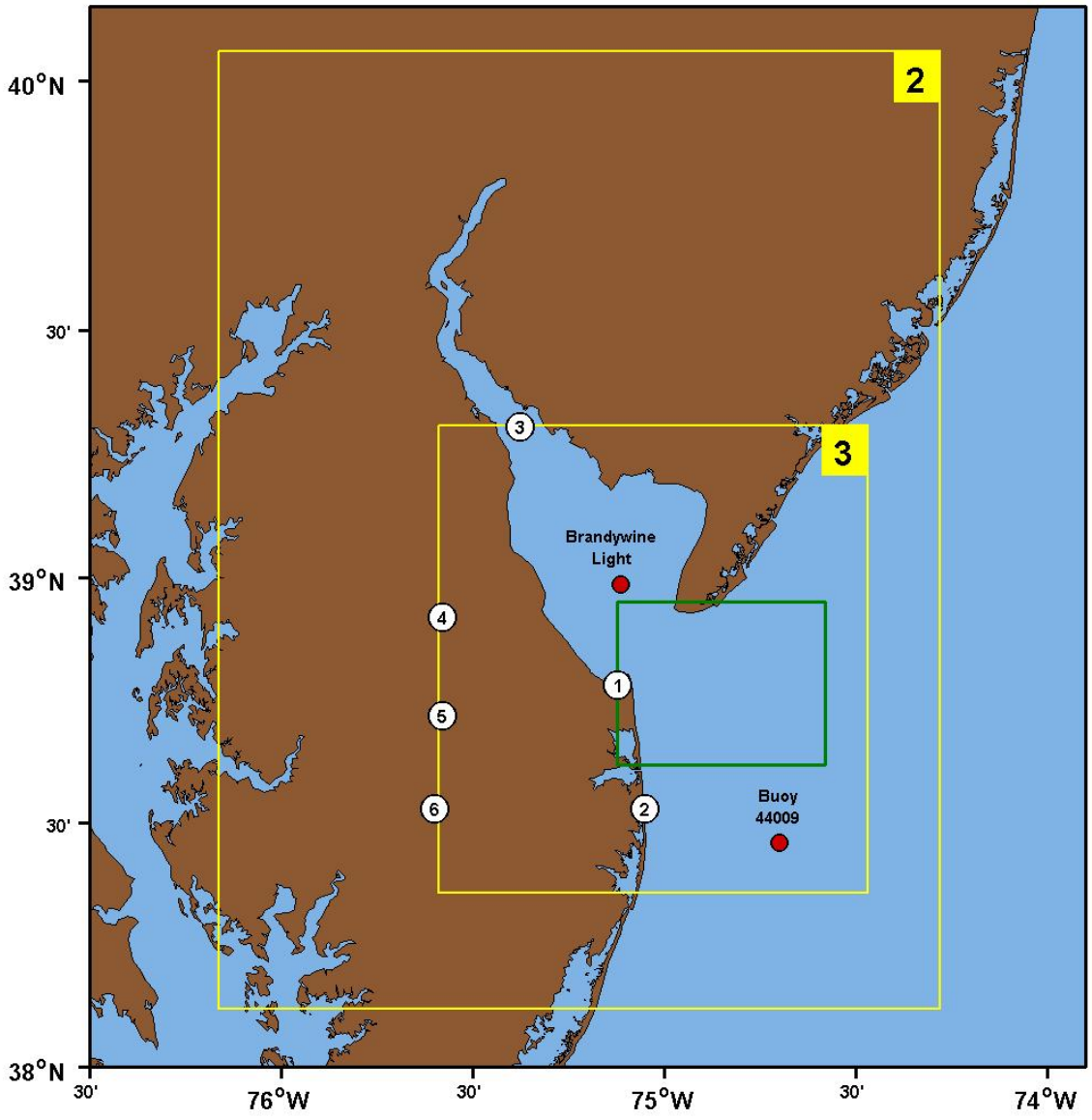

Figure 2.4: Two inner domain nests (yellow boxes, numbered 2 and 3) used for the Delaware Bay WRF model. Six wind measurement stations on or near land (white circles) and two stations over water (red circles) were used to assess the WRF model as part of this study. The region outside the bay mouth that is the focus for this study is shown as a green box. The WRF model outer nest (not shown) extends from just south of Cape Hatteras, NC northward to Long Island, NY.

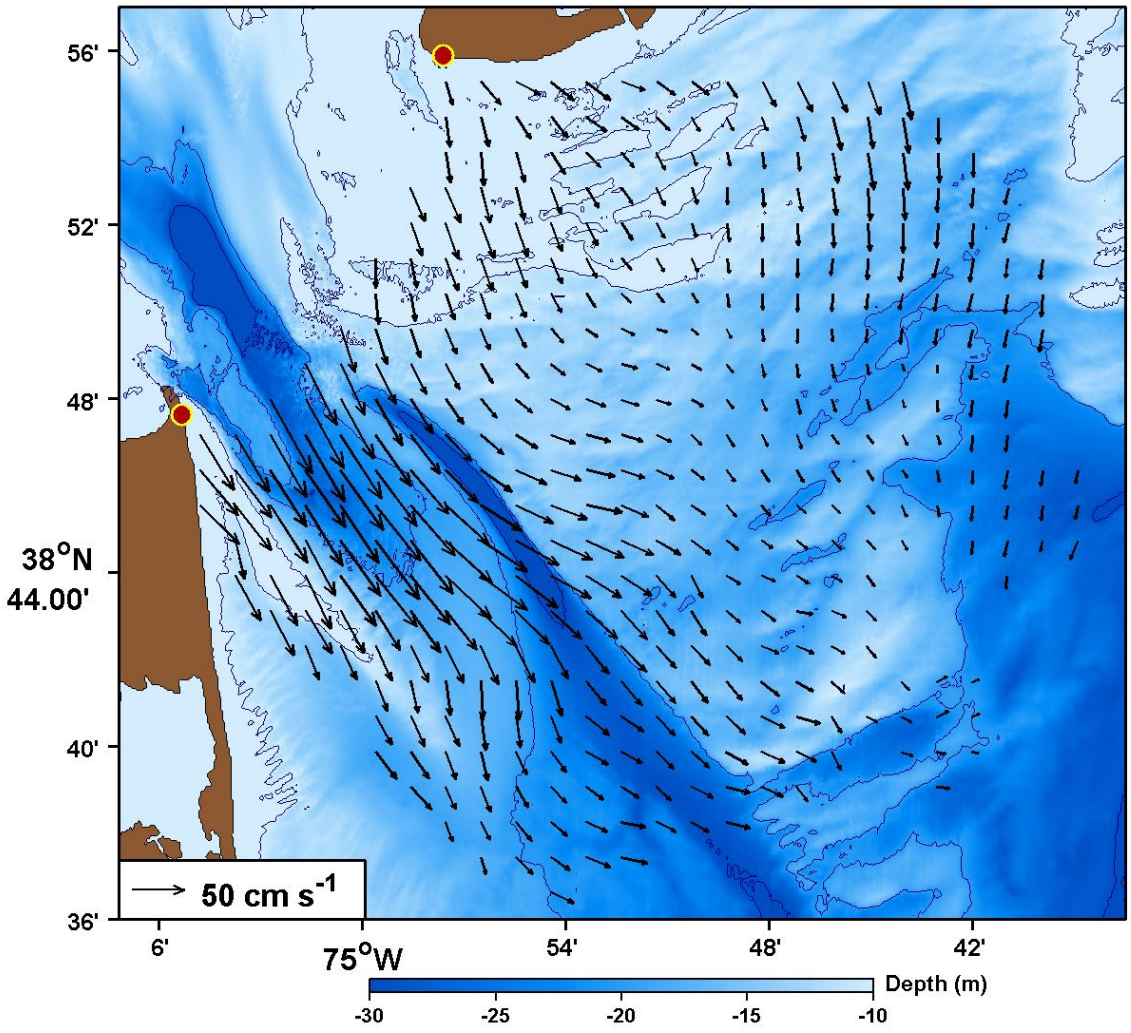

Figure 2.5: Example HF radar surface currents at the Delaware Bay mouth. Color contours show bottom topography (in m) and the two radar antenna locations are shown as red circles for 1 October 2007, 1000 GMT.

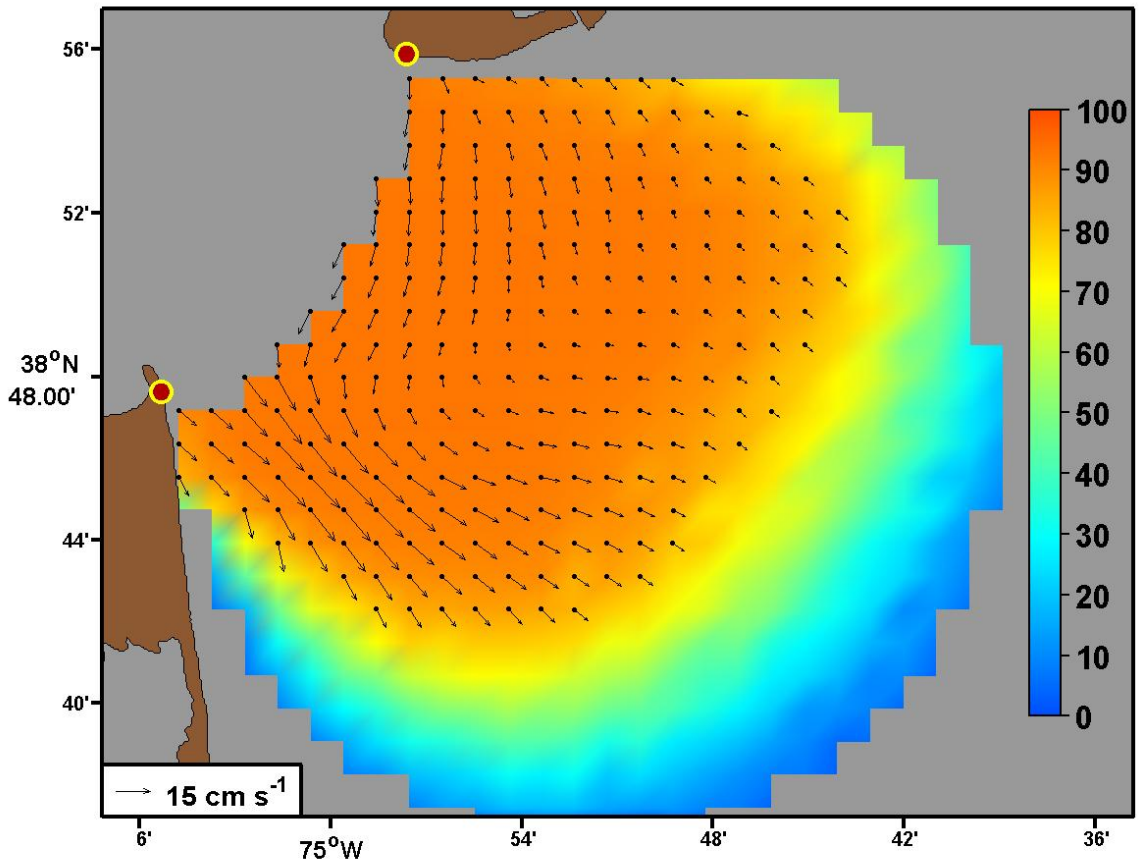

Figure 2.6: Color contours of temporal coverage (in percent) of HF radar measurements for period 1 October 2007 through 31 May 2008. The 250 grid locations with a minimum of 80% coverage are shown as black circles. At these locations, mean velocity vectors (black) for the entire analysis period are overlaid.

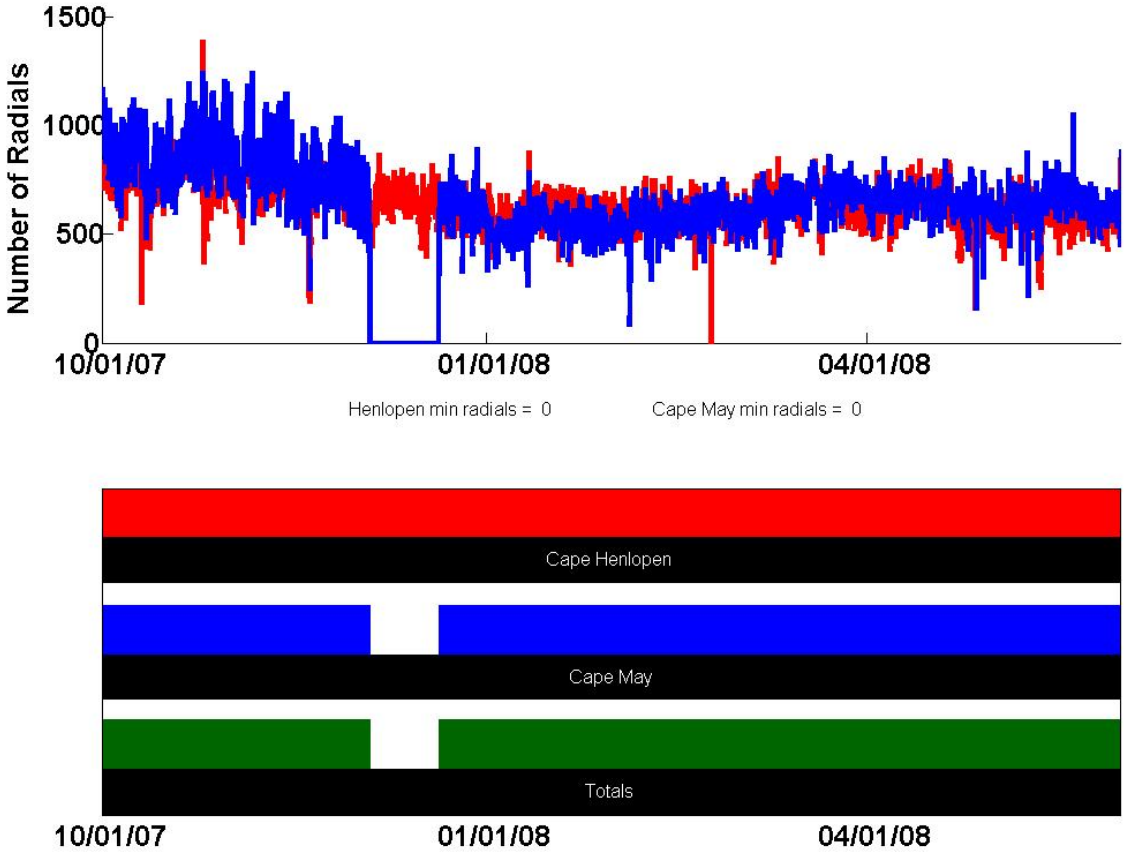

Figure 2.7: Plot on top shows the number of radials for Cape Henlopen (blue) and Cape May (red) over the time period 1 October 2007 through 31 May 2008. The bottom plot shows the status of the radar sites over the same time period. Notice the equipment failure at the Cape May site in December 2007.

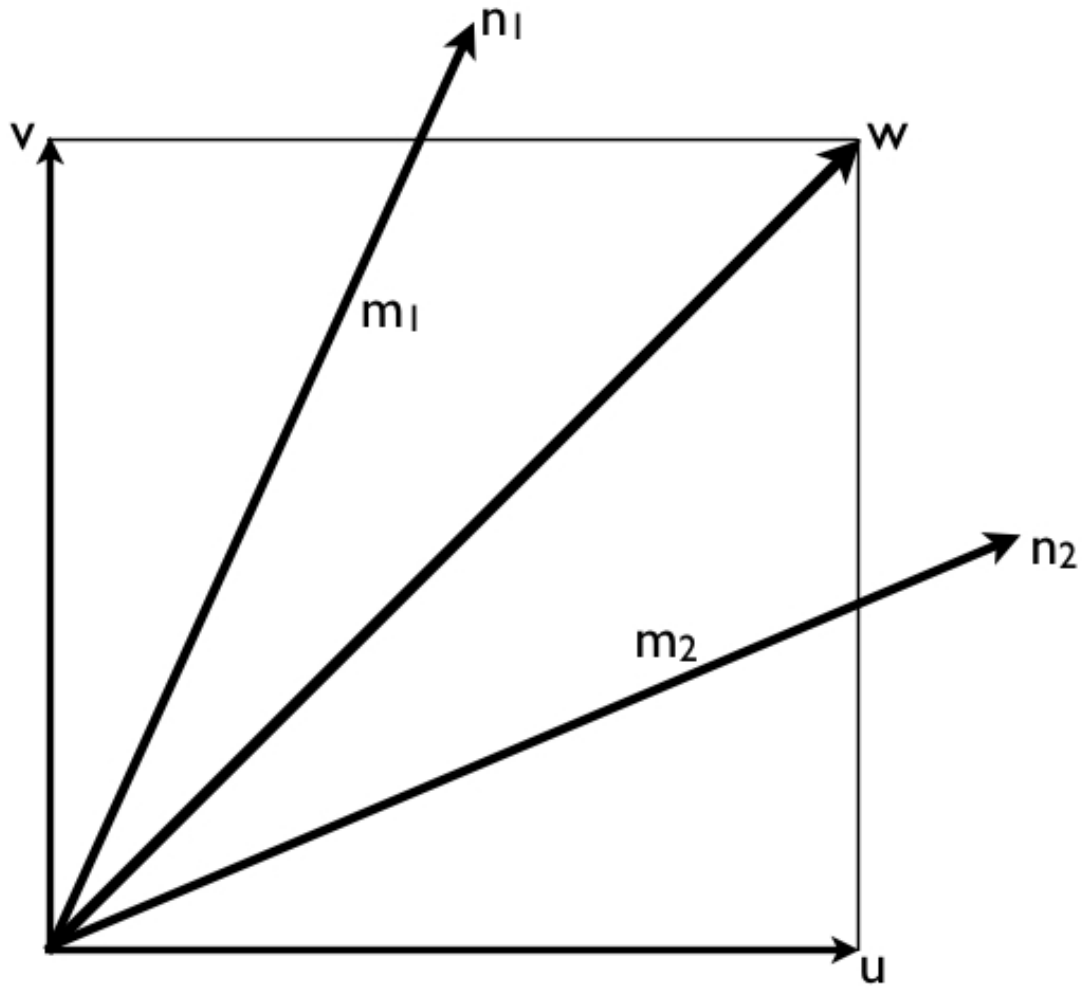

Figure 2.8: Diagram of vectors from two radar sites at a desired grid point.

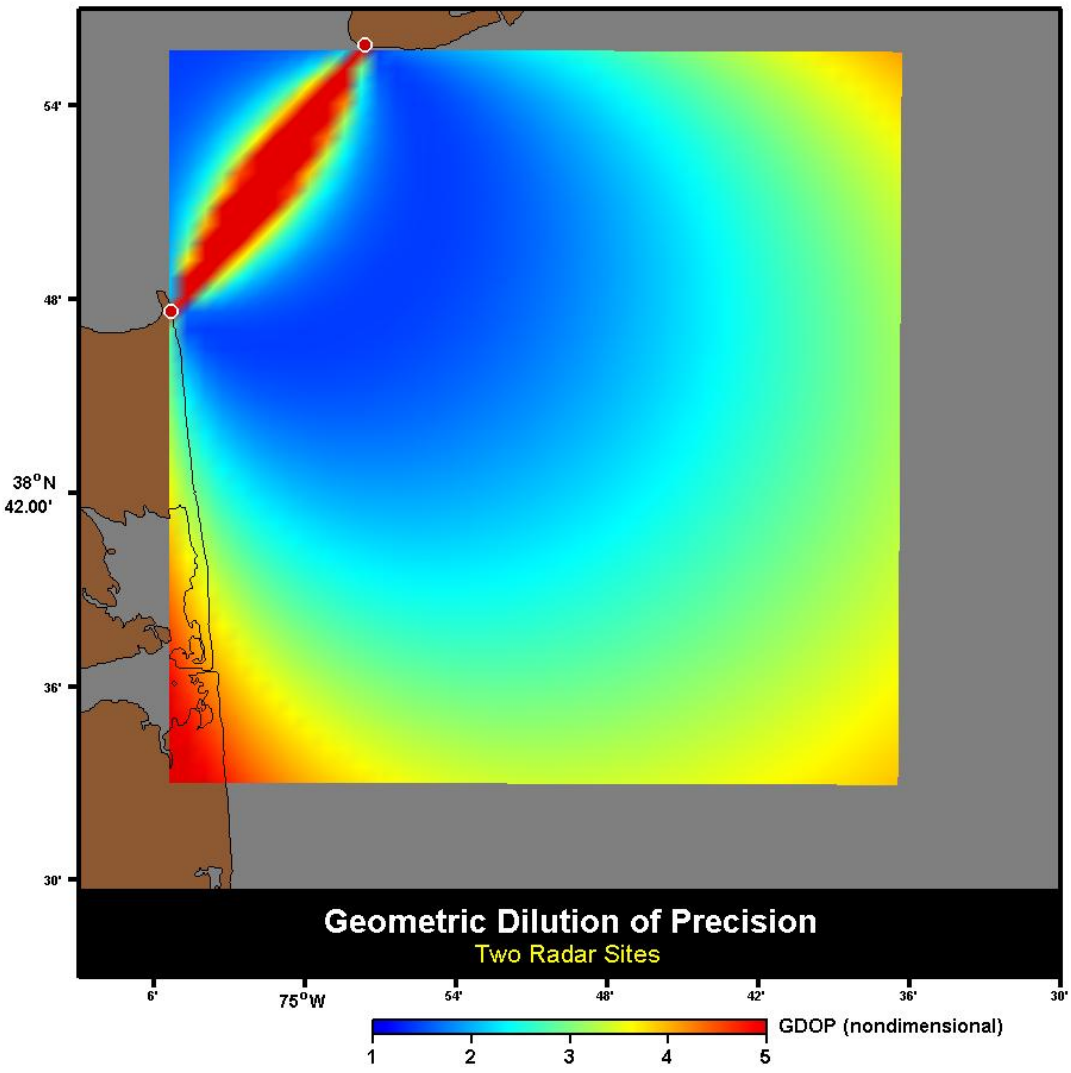

Figure 2.9: Geometric dilution of precision (GDOP) for the two site Delaware Bay HF radar network.

Chapter 3

COMPARISON OF SYNOPTIC DATA WITH POINT MEASUREMENTS

Two synoptic data sets are examined, observed surface currents with HF radar and modeled near surface winds with WRF. As noted earlier, historical circulation analyses have relied on point measurements. With the introduction of synoptic data sets, like the ones shown here, it is necessary to compare the two to provide more confidence in the newer measurements.

3.1 Statistics Used Here

The remainder of this chapter focuses on comparisons between near–surface wind and current time series. These records will be quantitatively compared using several statistics:

1) *Pearson scalar correlation* (r) - is a measure of the correlation or strength of linear dependence between two variables. This quantity is the covariance of the two variables divided by the product of their standard deviations.

2) *Vector correlation* (ρ,ω) - computes the complex correlation between two vector times series yielding an amplitude correlation (ρ) and an estimate of a mean veering angle (ω), based on Kundu (1976).

3) *RMS difference* (Δu_{RMS}) - is a measure of the magnitude of variability of the difference of two scalar time series. It is defined as:

$$\Delta \mathrm{u_{RMS}} = \sqrt{\left(\frac{1}{N}\right)\sum_{n=1}^{N}\left(u_n^{\mathrm{ADCP}} - u_n^{\mathrm{radar}}\right)^2} \tag{3.1}$$

where N is the number of samples in the vector time series.

4) *Linear regression fits* (a,b) - is an a method for modeling the relationship between two variables with linear regression though least squares fitting orthogonal residuals yielding the slope (a) and the y–intercept (b) of the component time series.

3.2 Near Surface Current Comparisons

Here, all three ADCP deployments from table 2.1 will be examined. The locations, time periods, and depth are all available in the table. The ADCP time periods span HF radar time periods one and three (see table 2.2). For the comparisons, the ADCP velocities from the near-surface bin were smoothed using a moving average (arithmetic mean) filter with a window width of one hour, to mimic the HF radar temporal averaging scheme. The ADCP velocities from the nearest HF radar grid point available were used. The first deployment (A) occurred during the fall of 2007 and was located near the western edge of the HF radar footprint (see figure 2.2). Subsequent deployments (B and C) occurred during the spring of 2009 and were located in the central portion of the HF radar footprint, where HF radar radial crossing angles are optimal. It is important to note that deployments B and C are a distance of 3.8 km apart.

Statistics are computed for both u (east–west) and v (north–south) velocity components. Radial velocities are also compared. Radial velocity (z) is defined as current velocity parallel to a line between the ADCP and the Cape Henlopen

HF radar antenna (z_1) and current velocity parallel to a line between the ADCP and the Cape May HF radar antenna (z_2) with positive values directed towards the antennas.

The ADCP is not the ideal instrument for inter–comparisons with HF radar data. The reason for this is that the ADCP averages over spatial areas on the order of centimeters to meters while the radar averages over spatial areas of several kilometers. ADCPs also can return much higher temporal resolution, on the order of minutes, compared to the hour long averaging time for our 25 MHz radars. Also, the actual physics of the scattering for both instruments is distinctly different. The radar scatters off the ocean surface and gets returns from ocean waves of half the wavelength of the transmitted wave. The ADCP, on the other hand scatters off particulate matter in the water column. The differences in spatial and temporal averaging, along with the differences in scattering mechanisms, make the measurement technologies as different as apples and oranges. Measurements are also subject to geometrical errors like GDOP (see section 2.5.1.1).

Figures 3.1, 3.3, and 3.5 (a,b) show a time series comparison between the ADCP nearest valid surface bin (blue) and the nearest HF radar measurement (red) for a four–day period of the respective deployment. There is a clear semi–diurnal tide phase agreement between the two measurements in all deployments. Figure 3.5 b shows the time series of v at location C. The speeds here seem to be slightly smaller then at the other two locations/deployments.

Figures 3.1, 3.3, and 3.5 (c,d) shows the scatter plots of all (u,v) measurements. Table 3.1 has the relevant statistics from this comparison analysis for frames A, B, and C. The ADCP speeds seem to be higher than the radar speeds for frame B in the u direction. The u direction also contains larger velocity magnitudes. Deployment C produces the best agreements with the HF radar.

Figures 3.2, 3.4, and 3.6 (a,b) depict the time series of the radial speeds from

the moored ADCP (blue), with those measured from the Cape Henlopen and Cape May radars (red) for four days during the deployment time period. The ADCP mooring location for frame A was very close to the Cape Henlopen radar and near the edge of the Cape May radar coverage footprint. This caused radial velocities from the Cape Henlopen site to be more numerous than those from the Cape May site. Again, there was a strong presence of a semi–diurnal tidal signature.

Figures 3.2, 3.4, and 3.6 (c,d) shows scatter plots of radial speed measurements at Cape Henlopen and Cape May. The statistics for frames B and C are more consistent between the two sites because of the locations of the ADCPs. These frames are essentially equidistant from both radar sites and in an area of low GDOP.

Table 3.1 presents the statistics made between HF radar currents and those from three ADCP deployments. The (u,v) velocities show RMS differences ranging from 6.74 to 23.96 cm $s^{-}1$, which is generally consistent with published results from other geographic regions. In all cases, both the scalar and complex correlations were very high.

Deployment A was part of an unrelated sediment transport study and provides "measurements of opportunity" for this analysis. Deployments B and C were part of a study designed to assess a new model being implemented at the mouth of the Delaware Bay. These locations (B and C) are essentially equidistant from both radar antenna and provides more consistent statistics.

For completeness, figure 3.7 shows the comparison between frames B and C which were approximately 3.8 km apart and deployed over the same time period. Table B shows statistics for the comparison between frames B and C. The number of valid data points is much higher than the ADCP vs. HF radar where the averaging time is one hour and as compared to the ADCP averaging time of five minutes. This comparison shows a good agreement in the u direction and weaker agreement in the v direction.

Frame		N	Δ_{RMS}	r	a	b	ρ	ω
A	u	817	14.02	0.92	1.45	-6.74	0.91	-25.34
	v		23.96	0.89	0.54	-1.45		
	z_1	742	18.55	0.92	0.90	4.31		
	z_2	455	20.92	0.65	0.70	-2.23		
B	u	771	14.53	0.96	0.82	4.65	0.97	-3.6
	v		11.5	0.98	0.73	-5.65		
	z_1	751	11.31	0.79	0.86	-2.19		
	z_2	787	10.83	0.96	0.79	-3.39		
C	u	772	8.79	0.97	0.91	0.11	0.97	6.36
	v		6.74	0.95	1.22	-0.28		
	z_1	753	10.44	0.95	0.88	1.55		
	z_2	740	8.43	0.96	1.13	-1.49		

Table 3.1: Table of ADCP vs. HF radar statistics. N is the number of samples, ΔRMS is the root mean square difference in cm s^{-1}, r is the linear correlation coefficient, a is the slope of the linear fit, b is the y–intercept of the linear fit, ρ is the amplitude of the complex correlation, and ω is the phase of the complex correlation. z_1 and z_2 denote the radial components between the ADCP and Cape Henlopen and the ADCP and Cape May respectively.

Lastly, it is necessary to examine the causes of the observed difference between the ADCP and radar comparisons. The differences in the spatial averaging areas of the two measurement technologies is examined with a Matlab toolbox capable of creating several analytic velocity fields and simulating the results that would be produced within the CODAR software. This topic is discussed in detail in appendix B. To summarize the results, a conservative estimate is that we can explain roughly 10% to 20% of ADCP vs. radar point differences.

3.3 Near Surface Wind Comparisons

Here, WRF was forced with coarse–scale information from NCEP's North American Model (NAM) which has a spatial resolution of 40 km and a temporal

	N	Δ_{RMS}	r	a	b	ρ	ω
u	9456	12.64	0.97	0.90	4.46	0.98	-20.54
v		23.09	0.82	0.44	-2.48		

Table 3.2: Table of ADCP frame B vs ADCP frame C statistics. N is the number of samples, ΔRMS is the root mean square difference in cm s^{-1}, r is the linear correlation coefficient, a is the slope of the linear fit, b is the y–intercept of the linear fit, ρ is the amplitude of the complex correlation, and ω is the phase of the complex correlation.

resolution of six hours. Our Delaware Bay simulations use three nested domains with spatial resolutions of 9 km (outer nest), 3 km (middle nest), and 1 km (inner nest). The spatial resolution of the land surface is 30 seconds for the two inner nests. Figure 2.4 shows the area covered by each of the two inner nests. The outer nest (extending from south of Cape Hatteras, NC northward to Long Island, NY) is sized to capture synoptic storms that may affect Delaware Bay. The middle nest (Figure 2.4, region 2) covers the entire Delaware Bay, and the inner nest (Figure 2.4, region 3) includes the entire HF radar measurement footprint. Overlapping five–day WRF simulations were computed for both the low and high outflow periods. The first day of each five–day run was discarded as spin–up and the start of each run overlapped the previous run by one day. Winds at 10 m were archived hourly. Figure 2.3 shows example 10 m wind vectors for 1 October 2007, 1000 GMT with every third wind vector shown, for clarity.

To assess the accuracy of the 10 m WRF winds used here, we compared them with observed winds (corrected to a height of 10 m) from eight stations around Delaware Bay during both the low and high outflow periods. Six of these stations were on or very near land (shown as numbered white circles in Figure 2.4). For these six stations, comparisons were made with the nearest WRF model grid location,

typically less than 0.5 km away, except for station 6, which was 1.5 km away from the nearest model grid point (in the WRF middle nest). The remaining two stations were over water, and the closest two stations to our study region (Brandywine Light and NOAA buoy 44009, shown as red circles in Figure 2.4). For these two stations, since the model winds were more spatially coherent over water, they were linearly interpolated in space to the station location. At all eight stations, observed winds were linearly interpolated to the nearest hour to match the WRF archiving scheme.

Note that the six stations on or near land are located along boundaries that are particularly challenging for the WRF model. Stations 1 and 2 are located very close to land–water boundary, where sharp gradients in surface properties occur. Stations 3–6 lie close to the boundary between the two inner WRF nests (nests 2 and 3 in Figure 2.4), where nested boundary conditions become important. Statistics for comparisons between observed and modeled winds at these six stations, then, represent a conservative estimate of model skill in the inner nest.

At each of the eight stations, complex correlation magnitude (σ_{mag}) and mean veering angle (σ_{phase}) were computed (Kundu, 1976). σ_{phase} is a measure of the average direction error (in degrees) between two vector time series, with negative values indicating model winds to the right of observed winds. RMS differences between observed and modeled wind components at 10 m (Δu_{rms}, Δv_{rms}) were also computed, as well as the RMS value of the observed wind magnitude ($|\vec{v}|_{rms}$). Table 3.3 shows the comparison statistics for each station during both the low and high outflow periods. Units for all RMS values are m s^{-1}. Note that no observations were available at Brandywine Light for the high outflow period.

For the two stations over water (Brandywine and buoy 44009), all σ_{mag} are 0.88 or greater, and all σ_{phase} values are less than 8°. All Δu_{rms} and Δv_{rms} values range from 2.4–3.0 m s^{-1}, with $|\vec{v}|_{rms}$ values of 6.8–8.9 m s^{-1}. At the six stations on or near land (stations 1–6), Table 3.3 shows σ_{mag} range from 0.75–0.87, with slightly

higher correlations during the high outflow period. All σ_{phase} values at stations 1–6 are less than 20°, except for station 1 during the high outflow period, when σ_{phase} increased to almost 22°. $|\vec{v}|_{rms}$ values at stations 1–6 ranged from 2.64–6.94 m s^{-1}, with (Δu_{rms}, Δv_{rms}) values typically one–half to two–thirds of the $|\vec{v}|_{rms}$ values.

Coastal wind modeling is a challenging problem, particularly in geographic regions like Delaware Bay, where the winds are typically weak and variable. Here, the low σ_{phase} values for Brandywine Light and buoy 44009 (Table 3.3) indicate WRF model skill in representing wind direction over water. Since vector correlations are insensitive to wind magnitude uncertainties (when wind direction uncertainties are small), we expect the wind–surface current correlations discussed in section 4.2.2 to be reliable indicators of surface current response to wind forcing. Additionally, we found that the 40–hour low–pass filter (applied to both winds and surface currents prior to computing vector correlations) reduced the RMS differences between observed and modeled winds at all stations by roughly 0.5 m s^{-1}.

Period	Station	σ_{mag}	σ_{phase}	$\|\vec{v}\|_{rms}$	$\Delta(u,v)_{rms}$
Low outflow	Brandywine	0.88	1.30	6.85	u 2.54 v 2.39
	Buoy 44009	0.89	7.71	7.98	u 2.85 v 2.60
	1	0.82	18.37	5.56	u 2.98 v 2.83
	2	0.83	4.72	3.26	u 2.39 v 2.39
	3	0.82	-1.04	5.41	u 2.47 v 2.28
	4	0.77	-1.31	2.64	u 1.86 v 1.63
	5	0.79	0.91	2.98	u 1.71 v 1.67
	6	0.75	16.91	3.27	u 1.84 v 1.97
High outflow	Buoy 44009	0.91	4.21	8.90	u 2.63 v 3.02
	1	0.87	21.69	6.65	u 2.97 v 3.53
	2	0.86	6.42	4.33	u 2.25 v 3.11
	3	0.85	-2.26	6.94	u 2.77 v 2.65
	4	0.83	0.79	4.04	u 2.13 v 2.07
	5	0.85	2.05	4.21	u 1.91 v 2.09
	6	0.85	17.11	5.38	u 2.25 v 2.29

Table 3.3: Statistics of comparisons between observed and WRF model winds at eight stations (shown in Figure 2.4 for the low and high outflow periods. Complex correlation magnitude (σ_{mag}) and mean veering angle (σ_{phase}) are shown. Negative σ_{phase} values indicate model winds to the right of observed winds. RMS differences between observed and modeled wind components at 10 m (Δu_{rms},Δv_{rms}) and RMS observed wind speed($|\vec{v}|_{rms}$) are also shown.

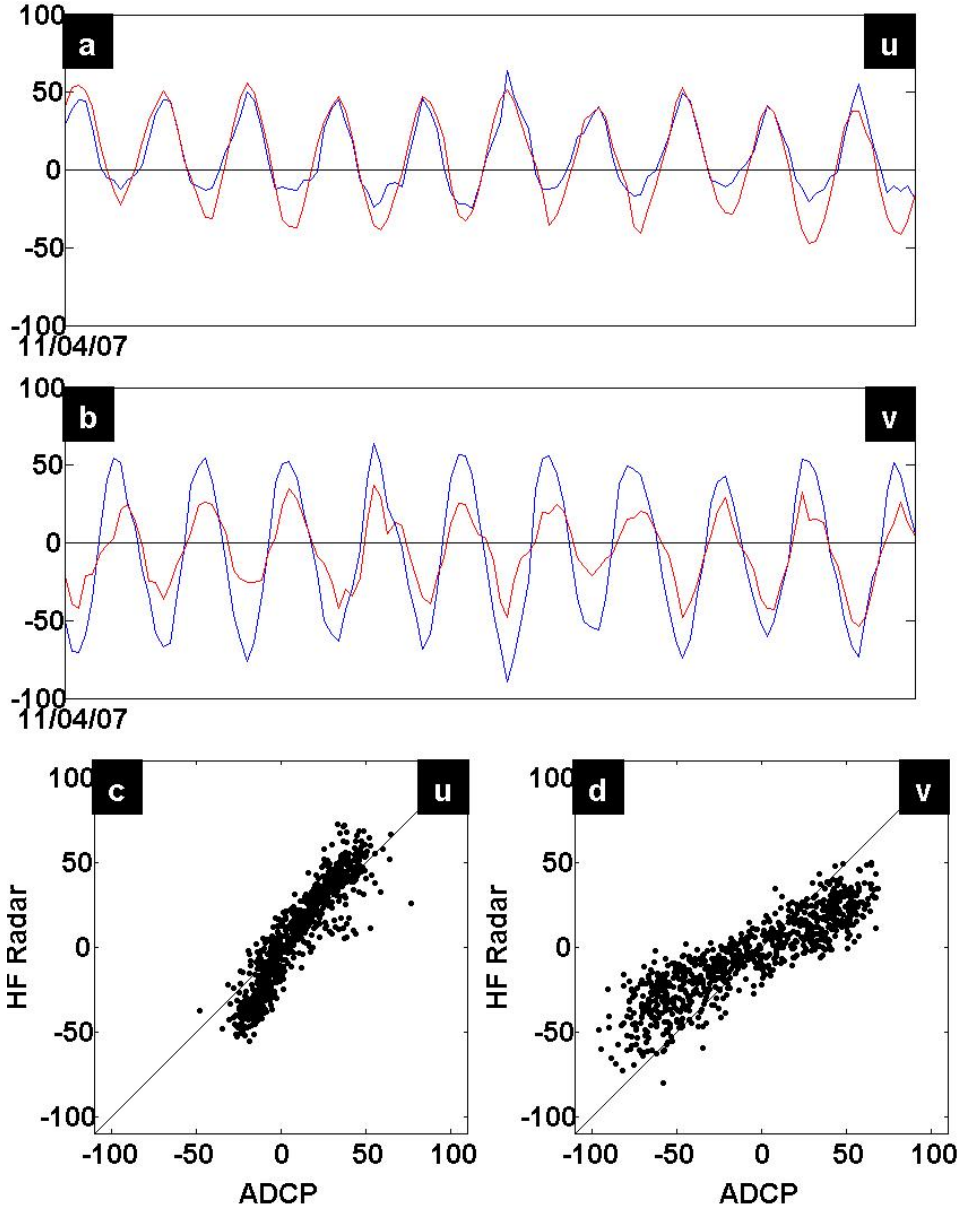

Figure 3.1: Example (u,v) time series (a and b) for 4–9 November 2007 showing moored ADCP measurements from frame A (blue) and HF radar measurements (red). Also, scatter plots for (u,v) velocities (c and d) with moored ADCP measurements along the x–axis, and HF radar measurements along the y–axis. In (c) and (d), a one to one correspondence line is also shown. All velocities are in cm s^{-1}.

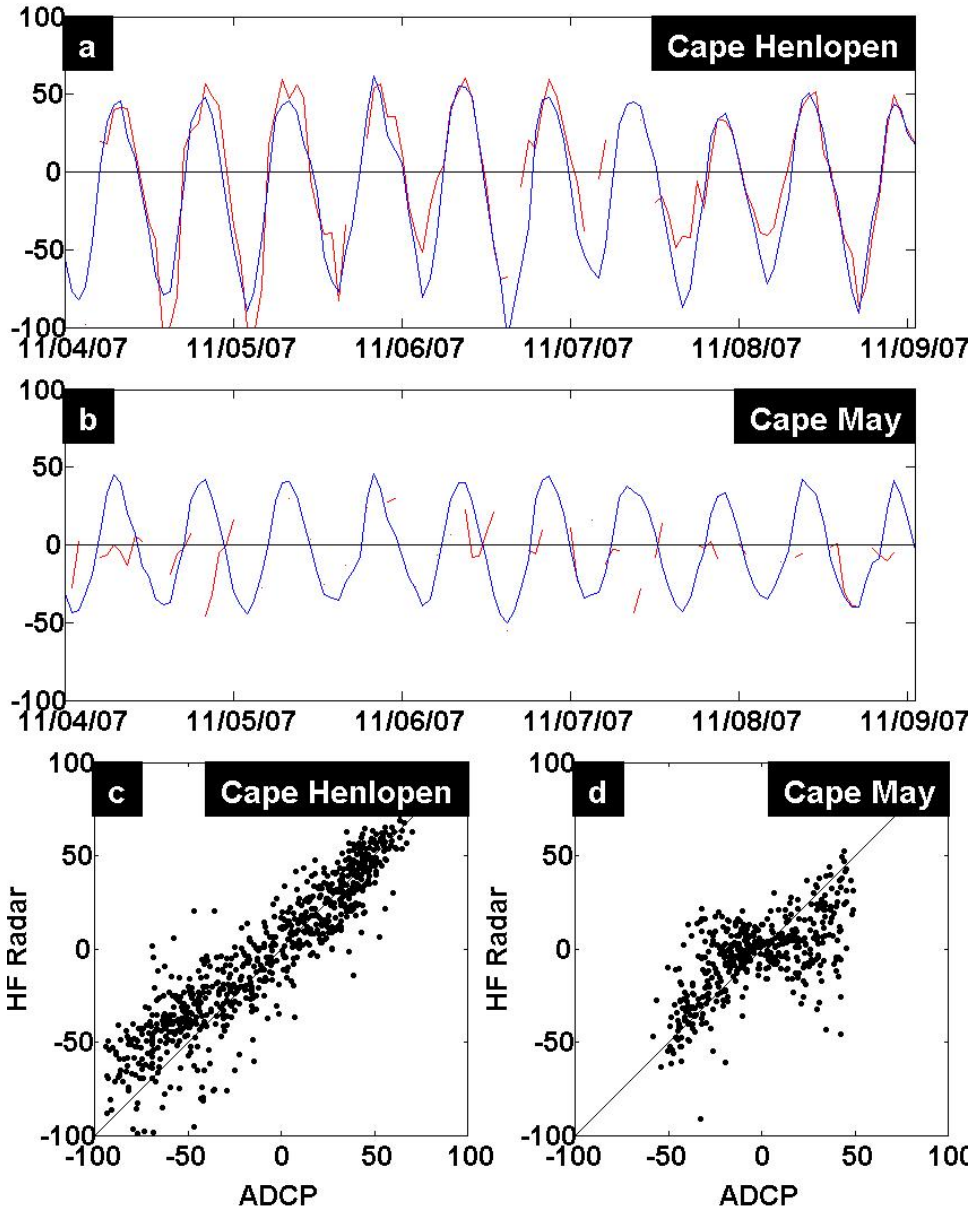

Figure 3.2: Example radial velocity time series (a and b) for 4–9 November 2007 showing moored ADCP measurements from frame A (blue) and HF radar measurements (red) referenced to Cape Henlopen radar antenna (a) and the Cape May antenna (b). Also, scatter plots showing moored ADCP radial velocities (x–axis) verses HF radar radial velocities (y–axis) referenced to the Cape Henlopen antenna (c) and the Cape May antenna (d). In (c) and (d), a one to one correspondence line is also shown. All velocities are in cm s^{-1}. Positive radial velocities are directed toward the antenna.

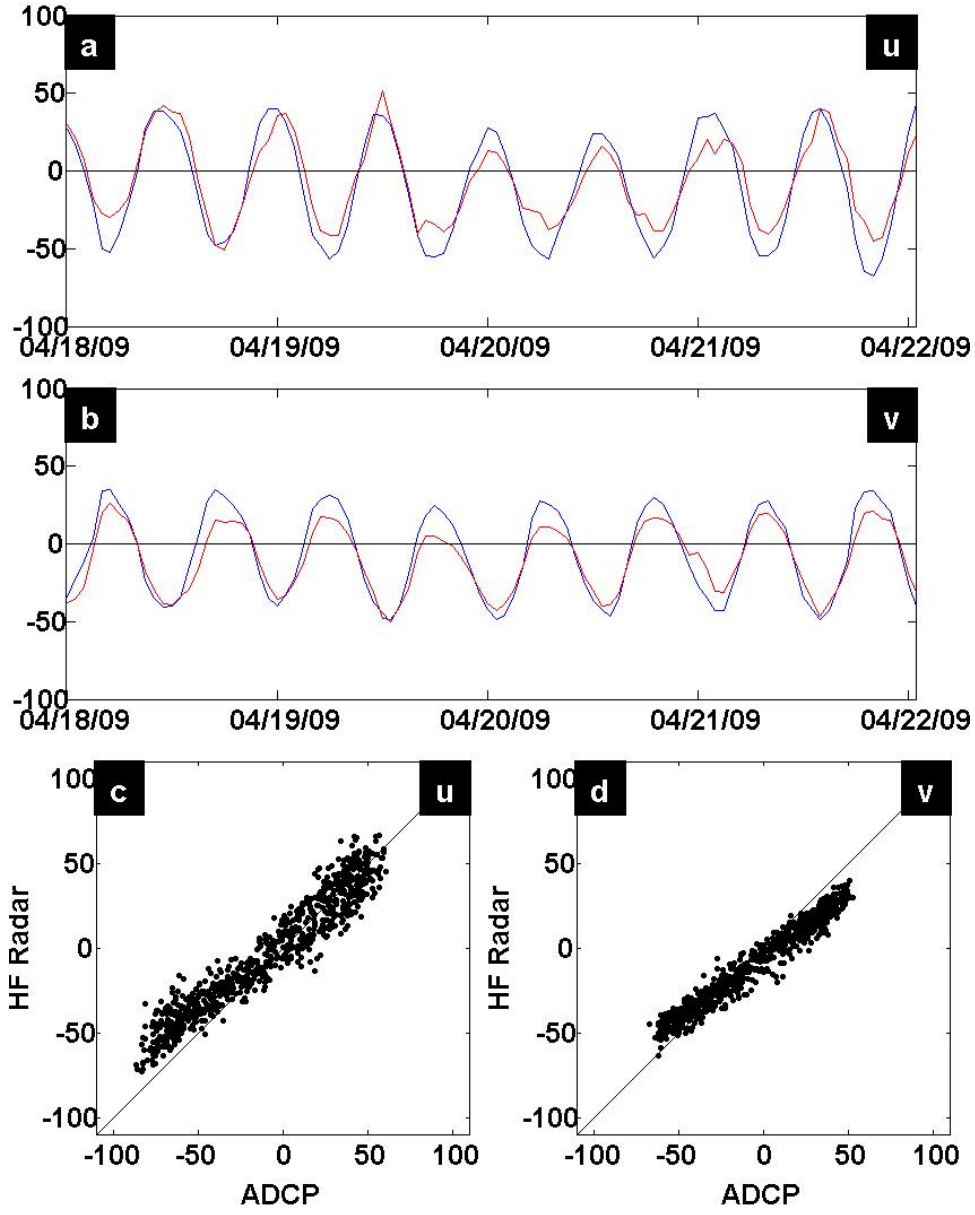

Figure 3.3: Example (u,v) time series (a and b) for 18–22 April 2009 showing moored ADCP measurements from frame B (blue) and HF radar measurements (red). Also, scatter plots for (u,v) velocities (c and d) with moored ADCP measurements along the x–axis, and HF radar measurements along the y–axis. In (c) and (d), a one to one correspondence line is also shown. All velocities are in cm s^{-1}.

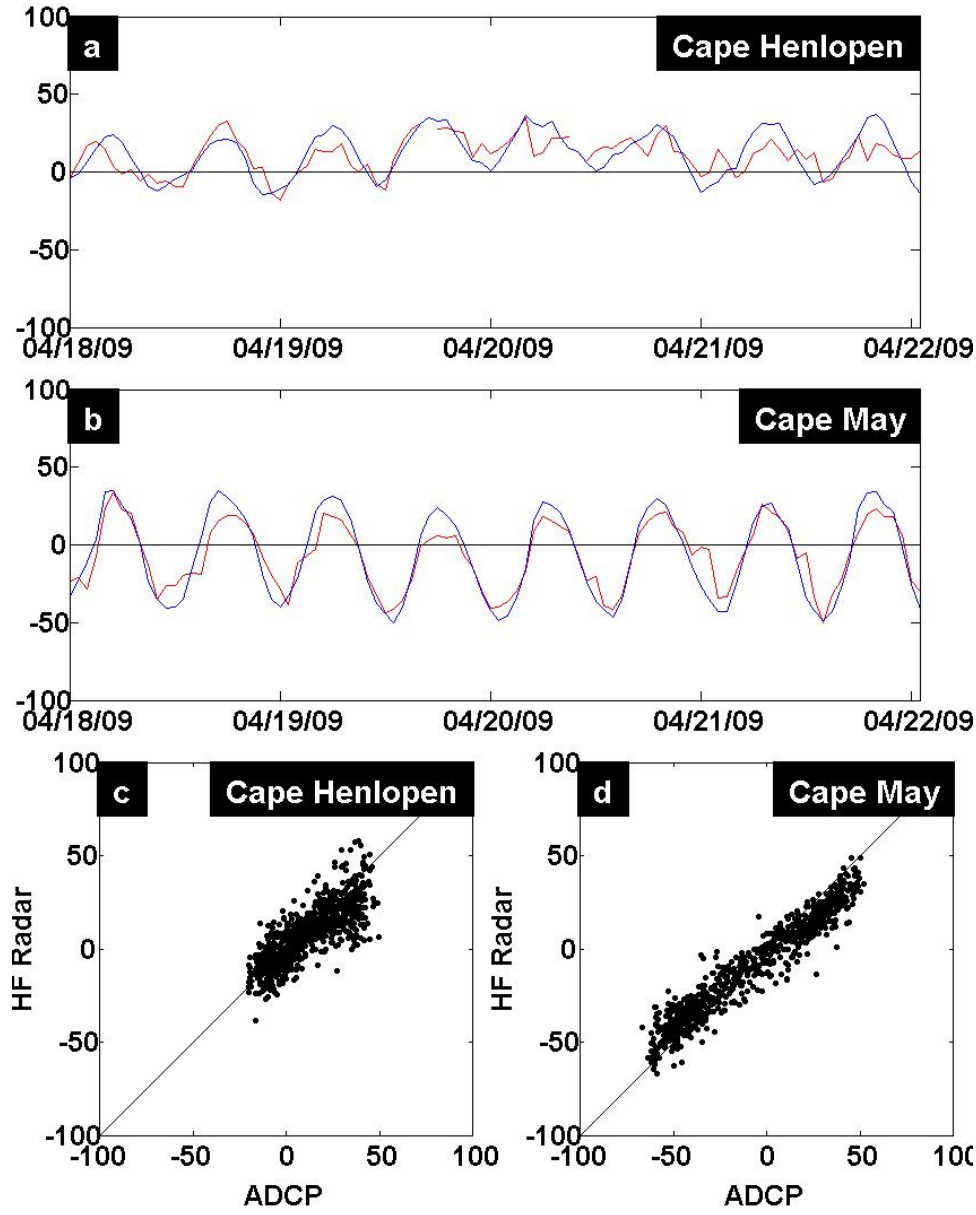

Figure 3.4: Example radial velocity time series (a and b) for 18–22 April 2009 showing moored ADCP measurements from frame B (blue) and HF radar measurements (red) referenced to Cape Henlopen radar antenna (a) and the Cape May antenna (b). Also, scatter plots showing moored ADCP radial velocities (x–axis) verses HF radar radial velocities (y–axis) referenced to the Cape Henlopen antenna (c) and the Cape May antenna (d). In (c) and (d), a one to one correspondence line is also shown. All velocities are in cm s^{-1}. Positive radial velocities are directed toward the antenna.

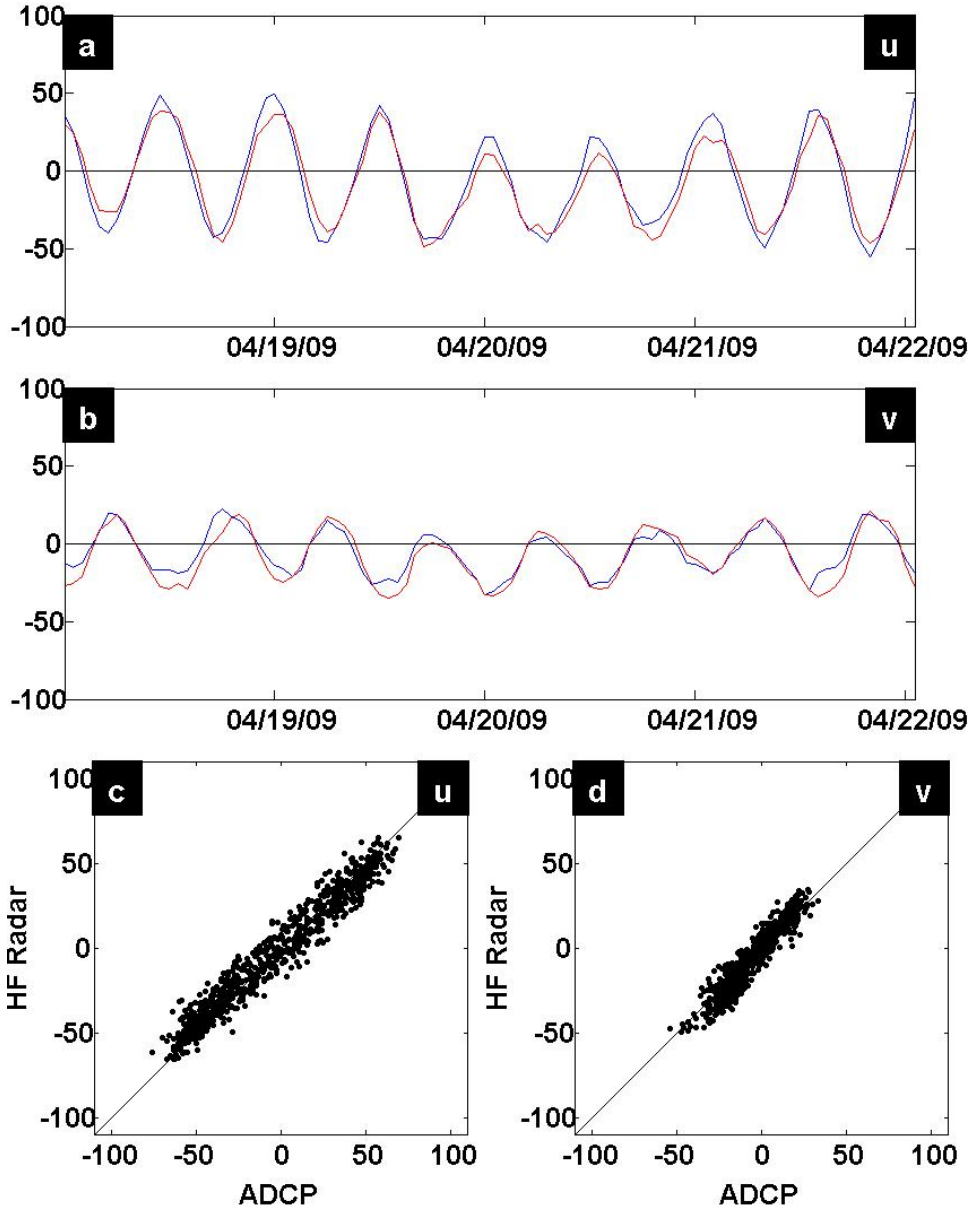

Figure 3.5: Example (u,v) time series (a and b) for 18–22 April 2009 showing moored ADCP measurements from frame C (blue) and HF radar measurements (red). Also, scatter plots for (u,v) velocities (c and d) with moored ADCP measurements along the x–axis, and HF radar measurements along the y–axis. In (c) and (d), a one to one correspondence line is also shown. All velocities are in cm s^{-1}.

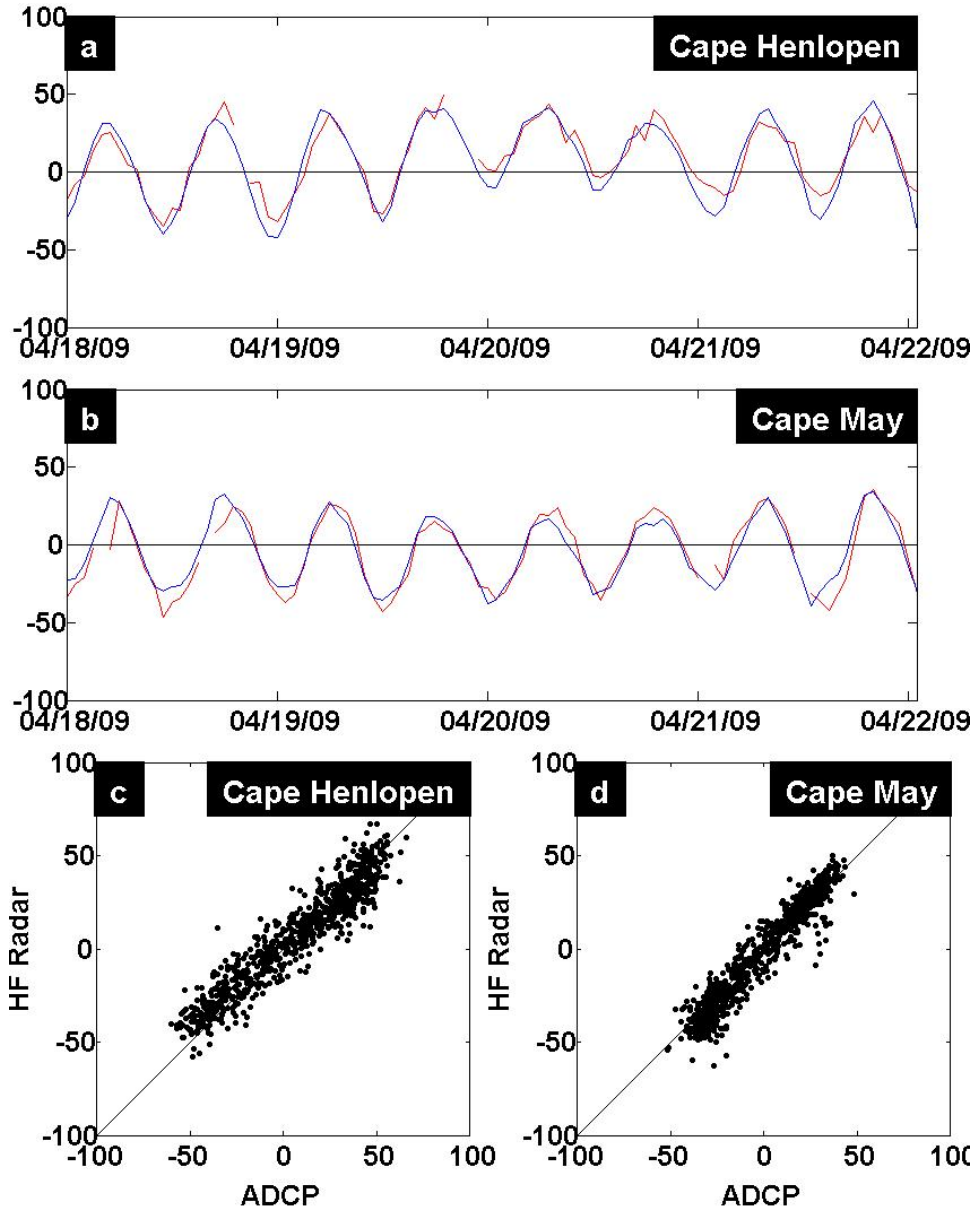

Figure 3.6: Example radial velocity time series (a and b) for 18–22 April 2009 showing moored ADCP measurements from frame C (blue) and HF radar measurements (red) referenced to Cape Henlopen radar antenna (a) and the Cape May antenna (b). Also, scatter plots showing moored ADCP radial velocities (x–axis) verses HF radar radial velocities (y–axis) referenced to the Cape Henlopen antenna (c) and the Cape May antenna (d). In (c) and (d), a one to one correspondence line is also shown. All velocities are in cm s^{-1}. Positive radial velocities are directed toward the antenna.

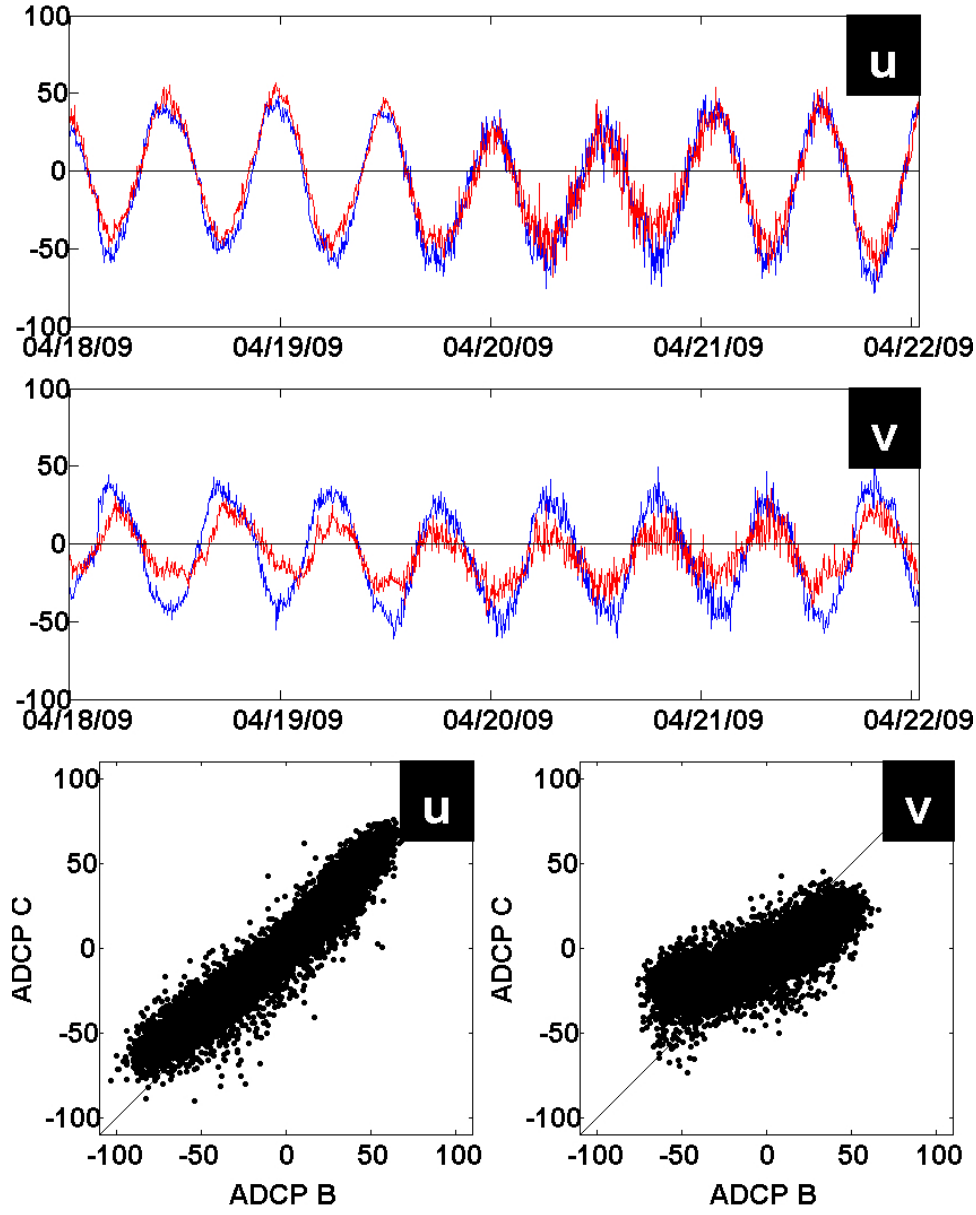

Figure 3.7: Example (u,v) time series (a and b) for 18–22 April 2009 showing moored ADCP measurements from frame B (blue) and frame C (red). Also, scatter plots for (u,v) velocities (c and d) with frame B measurements along the x–axis, and frame C along the y–axis. In (c) and (d), a one to one correspondence line is also shown. All velocities are in cm s^{-1}.

Chapter 4

EULERIAN PERSPECTIVE

In this chapter we study the spatial and temporal variability of surface currents and winds at the Bay mouth using synoptic maps. The current field can generally be partitioned into four parts:

1) Tides

2) Wind Driven

3) Freshwater Outflow

4) Residual.

These components of the velocity fields are partitioned by frequency. The spatial distribution of the tides is examined and identified as a large portion of the total variance. The wind–driven flow is a result of low–frequency winds. These low–frequency currents are more difficult to describe due to their magnitude in relation to the total currents. The two–dimensional characteristic of these Eulerian analyses is a huge improvement on the spatial resolution of historic observational experiments conducted in this region.

4.1 High–Frequency Features

The only high–frequency features examined in this section will be the tides. We will not only show the spatial distribution of the dominant semi–diurnal tide but

show its influence on the total variance of the velocities. It is important to note that that the tides, while deterministic, are a complicated forcing mechanism in coastal waters with the presence of complex coastlines and bathmetry.

4.1.1 Fitting Maps of the Tides

This section is taken from Muscarella *et al.* (2011).

Tide fits from time series of HF radar surface velocities were computed using the Matlab T_TIDE toolbox (Pawlowicz *et al.*, 2002), which fits multiple harmonics to vector time series that may include temporal gaps. A total of 45 astronomical and 101 shallow–water constituents are available. Signal to noise ratios (SNR) are estimated for each constituent using a nonlinear parametric bootstrap technique with a white noise assumption. We followed Pawlowicz *et al.* (2002) recommendation and used a minimum SNR value of two as a measure of a statistically significant fit. As a measure of tidal energy, we define a tidal ellipse magnitude, $\mathcal{M}$, as the square root of the sum of the squares of the major (r_a) and minor (r_b) tidal ellipse axes:

$$\mathcal{M} = \sqrt{r_a^2 + r_b^2}.$$

For time period 1 (see table 2.2), tidal velocity fits were computed at 250 grid locations with at least 80% temporal coverage (see Figure. 2.6). We explored the relative importance of all resolved tidal constituents by examining fits using a set of constituents selected using T_TIDE's objective criteria. For most grid locations, five constituents (M2, N2, S2, K1, and O1) were found to be the most energetic (largest $\mathcal{M}$ values). In many cases, these five constituents were also the only ones with statistically significant fits (SNR $\geq$ 2). We also computed a second set of tide fits at each grid location using only these five constituents.

Table 4.1 shows $\mathcal{M}$ and SNR statistics (minimum, maximum, mean, and standard deviation) for the five-constituent tide fits at the 250 grid locations shown

in Figure 2.6. All minimum SNR values in Table 4.1 are greater than two, and mean SNR values were approximately 20 or greater. Mean $\mathcal{M}$ values for N2 and S2 were about 8, roughly one–fifth of the M2 value. Mean $\mathcal{M}$ values for the two diurnal constituents were about 4, roughly one–tenth of the M2 value.

	Period	$\mathcal{M}_{min}$	$\mathcal{M}_{max}$	$\overline{\mathcal{M}}$	$\mathcal{M}_{SD}$	SNR_{min}	SNR_{max}	$\overline{SNR}$	SNR_{SD}
M2	12.42	28.52	84.01	43.77	10.77	986.55	5713.38	2297.70	881.07
N2	12.66	5.33	16.82	8.12	1.92	38.76	173.53	79.35	25.60
S2	12.00	5.55	15.19	8.02	1.67	38.03	199.09	81.79	23.10
K1	23.93	2.44	8.16	3.94	1.08	3.58	66.47	21.35	14.55
O1	25.82	1.94	6.26	3.56	0.53	6.79	44.45	19.69	7.42

Table 4.1: Period (hrs), $\mathcal{M}$ (cm s^{-1}), and signal–to–noise (SNR) statistics for five–constituent tide fits from HF radar measured surface currents

4.1.2 Spatial Distribution of M2

Münchow *et al.* (1992) used current meter records at various depths from 31 moorings to show that the M2 tide constituent was the dominant component on the coastal region adjacent to the Delaware Bay mouth. However, only nine of their moorings were in the immediate vicinity of our analysis region, four along the line across the bay mouth, and five southeast of our radar footprint (Figure 4.1, black ellipses). Along the bay mouth, their M2 tide ellipses were nearly rectilinear and roughly perpendicular to the line across the mouth. Offshore, M2 tidal current magnitudes decreased by at least a factor of two.

M2 tidal ellipses are shown in red in Figure 4.1. For clarity only every second ellipse is shown. Ellipses from the Münchow *et al.* (1992) analysis are also shown (in black). Note that, of the four moorings near the bay mouth, only one was within the radar footprint. Five moorings were seaward of the radar footprint, to the southeast. The overall agreement between the M2 ellipses from two data sets shown in Figure

4.1 is excellent, both showing rectilinear ellipses aligned with the local bathymetry at the bay mouth. The largest $\mathcal{M}$ values occur in the deep channel at the southern side of the mouth. M2 ellipses from the radar measurements show decreasing $\mathcal{M}$ values moving seaward, consistent with the smaller M2 current magnitudes at the five offshore Münchow *et al.* (1992) sites.

Five of the Münchow *et al.* (1992) moorings were seaward of the radar footprint, to the southeast. Of the four Münchow *et al.* (1992) moorings near the bay mouth, only one was within the radar footprint, near the southern edge of the bay mouth. At this mooring location, Münchow *et al.* (1992) reported M2 (r_a, r_b) values of (94.3, 7.5) cm s^{-1}, with the ellipse oriented at an angle of 127.0° with respect to east. These values agree very well with those computed at the nearest radar grid point (160 meters away): (r_a, r_b) = (83.5, 11.5) cm s^{-1}, with an ellipse orientation angle of 125.9°.

The sparseness of these observations motivated Whitney and Garvine (2008) to study the spatial variability of the M2 tides outside the bay mouth with a numerical model. Their M2 tidal currents, although broadly consistent with the Münchow *et al.* (1992) analysis, could not be assessed with independent observations, until now.

M2 ellipses computed from the radar measurements (Figure 4.1) provide an important validation of the depth–averaged model M2 tidal current amplitudes reported by Whitney and Garvine (2008). Differences between M2 r_a computed from the radar measurements and interpolated, depth–averaged values from the Whitney and Garvine (2008) model are shown in Figure 4.2, with colored circles showing $(r_a^{model} - r_a^{radar})$ normalized by r_a^{radar} and expressed as percentages. The model data used to compute these differences was provided by M. Whitney. Figure 4.2 shows that, except for radar grid points close to the bay mouth, the magnitudes of M2 r_a differences were typically less than 20%. Note also that the model r_a values are

depth–averaged, and likely underestimate the true near–surface values.

The r_a differences shown in Figure 4.2 are larger near the bay mouth, with the largest differences occurring in the immediate vicinity of the Cape May peninsula. This is not surprising, since the bottom topography in that area is quite rugged, with water depths varying from one to ten meters over distances of less than one kilometer. In the model, this bottom bathymetry is smoothed, and locations with depths less than 1.5 meters are considered as land. In addition, radar measurement uncertainties are higher near the baseline between the two radars, which spans the bay mouth. Near the baseline, the look angles for the two radars are nearly parallel. When radial velocities become nearly parallel, geometric dilution of precision amplifies measurement uncertainties (Chapman *et al.*, 1997).

Since Whitney and Garvine (2008) noted a steady decrease in model M2 r_a moving offshore outside the bay mouth, we compared M2 r_a values along a line originating midway across the bay mouth and extending offshore perpendicular to the bay mouth line for 25 km (black line shown in Figure 4.2). Profiles of r_a interpolated at 1 km intervals along this line are shown in Figure 4.3 for the Whitney and Garvine (2008) model (in red) and for the HF radar tidal fits (in blue). No attempt was made to extrapolate radar r_a values for locations outside the radar footprint. Figure 4.3 shows excellent agreement between the model and radar–derived r_a profiles.

Tidal ellipses for the two other energetic semi–diurnal constituents (figure 4.4) were qualitatively very similar to the M2 ellipses and also agreed quite well with a single historical ellipse from Münchow *et al.* (1992). Diurnal ellipses (figure 4.5) were much less energetic, with typical $\mathcal{M}$ values about one–tenth of those for M2. K1 and O1 ellipses agreed well with those reported by Münchow *et al.* (1992) at one location within the radar footprint.

Figure 4.6 shows a map of the percent of the velocity variance explained by the 5 constituent tidal fits. The tides account for roughly 90% of the variance at

the bay mouth. Typical maximum tidal currents are of the order of 100 cm s^{-1} in the deep channel at the southern bay mouth. However, this fraction drops to about 40% at the eastern edge of the radar footprint.

In a region like Delaware Bay, where an estuary meets the adjacent shelf, stratification during high runoff periods could conceivably amplify the nonlinear interactions among tide constituents, potentially causing a shift in tide fit parameters. We examined this possibility using monthly fits over our analysis period and found no detectable variation in tide fit parameters, even during the spring runoff in 2008.

4.2 Low–Frequency Features

The low–frequency features addressed in this section are defined as any feature with a period longer than one day. These features are the wind–driven flow and the residual flow. The residual flow (total flow minus the tides) is dominated by two key features: the outflow plume and the cross–mouth flow. The main tools used here to examine the sub–tidal flow are low pass filtering and simple temporal means. These data products reveal some interesting Eulerian results of longer period forcings.

4.2.1 Low–Frequency Currents

A lack of synoptic observations over the ocean has limited previous efforts to describe low–frequency variations of currents at the Delaware Bay mouth. This obstacle is overcome with the high–resolution hourly HF radar surface currents. We examined the low–frequency surface currents using a variety of techniques, including detiding, 40–hour low–pass filtering, and weekly and longer term averages at each radar grid point. Although the details vary somewhat depending on the type of average, the broad picture is remarkably consistent with earlier studies of Delaware Bay. Moreover, except for the high outflow period in March and April 2008, mean maps showed little variability from month to month.

Figure 4.7 shows 45–day mean surface currents for the low and high outflow periods (see Figure 2.1). Currents at grid locations with at least 80% coverage over the 45–day period are shown. The spatial coverage during the low–outflow period was better (reaching further offshore) when compared to the high–outflow period. Both periods show a clear outflow plume evident at the southern bay mouth (over the deep channel) and evidence of cross–mouth flow directed to the southwest. Maximum outflow plume currents are 10 cm s^{-1} higher during the high outflow period. Note that these maximum currents (20-25 cm s^{-1}) are still only about 20% of the M2 tidal current amplitude. Current patterns at the eastern side of the footprint differ between the two periods: low–outflow period flow is predominantly to the east, and this flow veers to the south during the high–outflow period.

Figure 4.7 also shows color contours of the ratio of the mean current speed to the standard deviation magnitude for surface currents over the two analysis periods. Small values of this ratio (yellow–orange colors) show regions where velocity fluctuations are large compared to the mean speed, indicating that the mean flow is a poor indicator of "typical" flow conditions. During both periods, regions offshore of the bay mouth and northeast of the outflow plume have large velocity fluctuations compared to the mean.

4.2.2 Wind Driven Currents

It is challenging to assess the influence of local winds on surface currents in a coastal region when both winds and currents show marked variability. In Delaware Bay, diurnal variability due to seabreeze is significant during some periods, and tides are by far the most energetic component of the surface currents. Steady wind conditions rarely persist long enough to permit a simple Ekman analysis. Here, we restrict our analysis to a single question: Once the energetic tides are removed, can a surface current response to local wind fluctuations be detected?

To address this question, we computed complex correlations (Kundu, 1976) between surface currents and wind stress at 10 m from the WRF model for both the low and high outflow periods. The surface current and wind stress vector time series were each 40–hour low–pass filtered, and the model wind stresses were linearly interpolated to the radar grid.Figure 4.8 shows maps of the complex correlation magnitude (σ_{mag}) and mean veering angle (σ_{phase}) for wind–current correlations during both analysis periods. Negative σ_{phase} values indicate currents to the right of the winds.

The general correlation patterns in Figure 4.8 are quite similar between the two periods. The highest σ_{mag} values are near the center of the radar footprint. Near the bay mouth, where energetic mean flow to the southwest persists, σ_{mag} is reduced. At the southern side of the mouth, where energetic outflow persists, σ_{mag} is also reduced. The small, negative σ_{phase} values near the center of the radar footprint indicate that the surface currents are slightly to the right of the wind. However, in the outflow plume and along the northeast edge of the footprint, the low–frequency currents are to the left of the wind. These σ_{phase} maps suggest that strong wind events do not last long enough to set up a significant Ekman response in the low–frequency circulation.

However, comparisons between wind stress and surface current time series show that surface currents do veer rapidly to the right in response to energetic wind events that persist for more than a few days. For example, Figures 4.9 (low outflow period) and 4.10 (high outflow period) show time series of WRF winds at 10 m and surface currents at point A, located in the center of the radar footprint (see Figure 4.14). Winds and surface currents have both been 40–hour low–pass filtered, and vectors are shown at six–hour intervals. Time series of the direction difference (currents minus winds) are also shown, with periods when the currents were to the right of the winds shown in red. The wind records are dominated by brief, energetic

events that typically last no more than three days. The wind veering during these events indicates that they are most likely associated with passing weather systems, like storms. During energetic events, Figures 4.9 and 4.10 show that, while surface currents clearly veer rapidly to the right of the wind, the ocean response is simply not persistent enough to be detected through complex correlation analysis.

4.2.3 Cross-Mouth Flow

When the tides are removed from measured surface currents, two persistent features are evident. One is the outflow plume which has been well described in the literature and is a well–understood feature of estuarine circulation. The second feature is the cross-mouth flow, which is not well documented. A southwesterly flow across the bay mouth was reported earlier by Garvine (1985) and Wong and Moses–Hall (1998). As their results were based on current meters at fixed locations, little attention has been paid to this feature. Our analysis, based on synoptic measurements, provides more detail. This feature appears in all the HF radar low–frequency currents. It is unusual in that the flow is oriented across the bathymetry at the mouth.

Figure 4.11 shows 45 day mean currents during the low outflow period. The outflow plume and the cross–mouth flow regions are noted. These low frequency currents are localized near the bay mouth. Note that this region is near the baseline region of the radar sites. Figures 4.12 and 4.13 show close–up views of the cross–mouth region for the low and high outflow periods. Mean cross–mouth flow is higher during the high outflow period. This indicates an amplification of the cross–mouth current due to periods of increased outflow.

The three–dimensional structure of cross–mouth flow from an ADCP record at deployment C (Figure 4.15) for high outflow, shows little variation throughout the water column. This suggests that the water column is barotropic for this time period. Note also that currents are predominantly towards the southwest. Figure

4.16 also shows the constant velocity throughout the water column for flood (blue) and ebb (red) tide. There seems to be only a difference of approximately 3 cm s^{-1} over the 8 meters of the water column. This is likely due to interaction with the bottom. The lack of three–dimensional structure again hints at outflow as the forcing behind the amplification of the flow during the two periods.

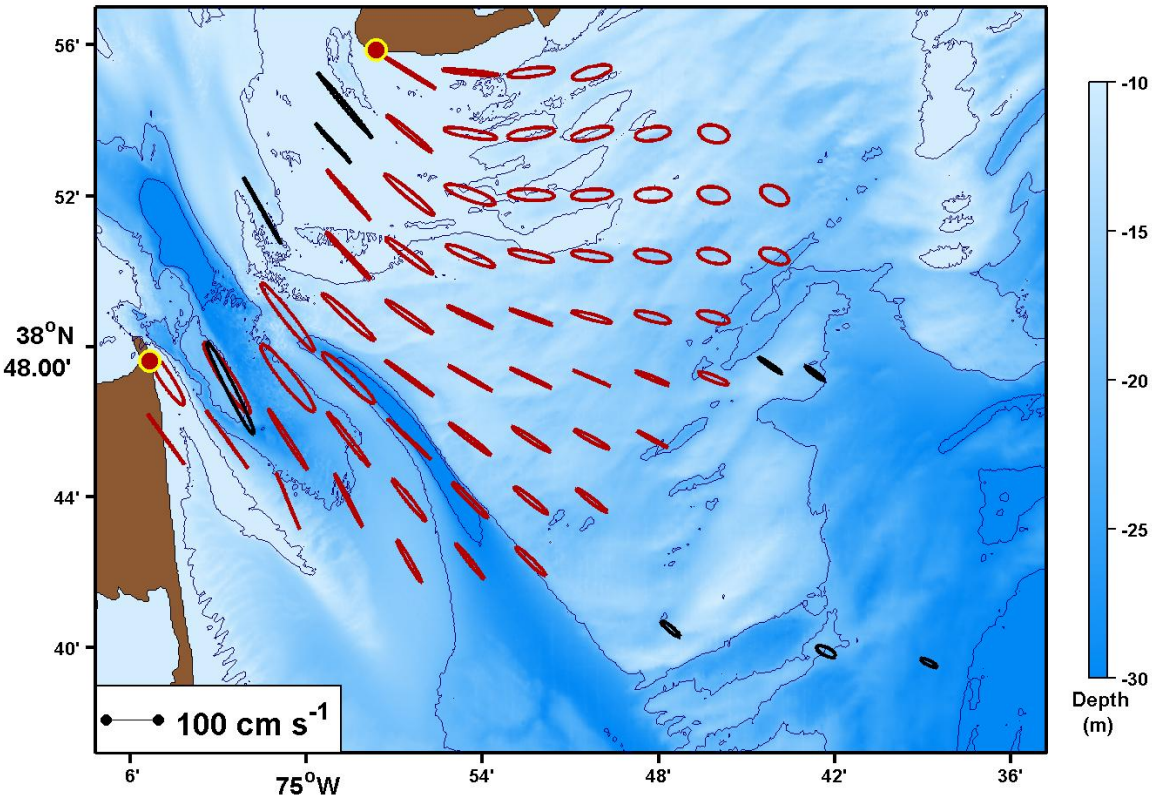

Figure 4.1: M2 tidal ellipses for the period 1 October 2007 through 31 May 2008. For clarity, only ellipses at every second analysis location are shown. Historical ellipses reported by Münchow *et al.* (1992) are shown in black.

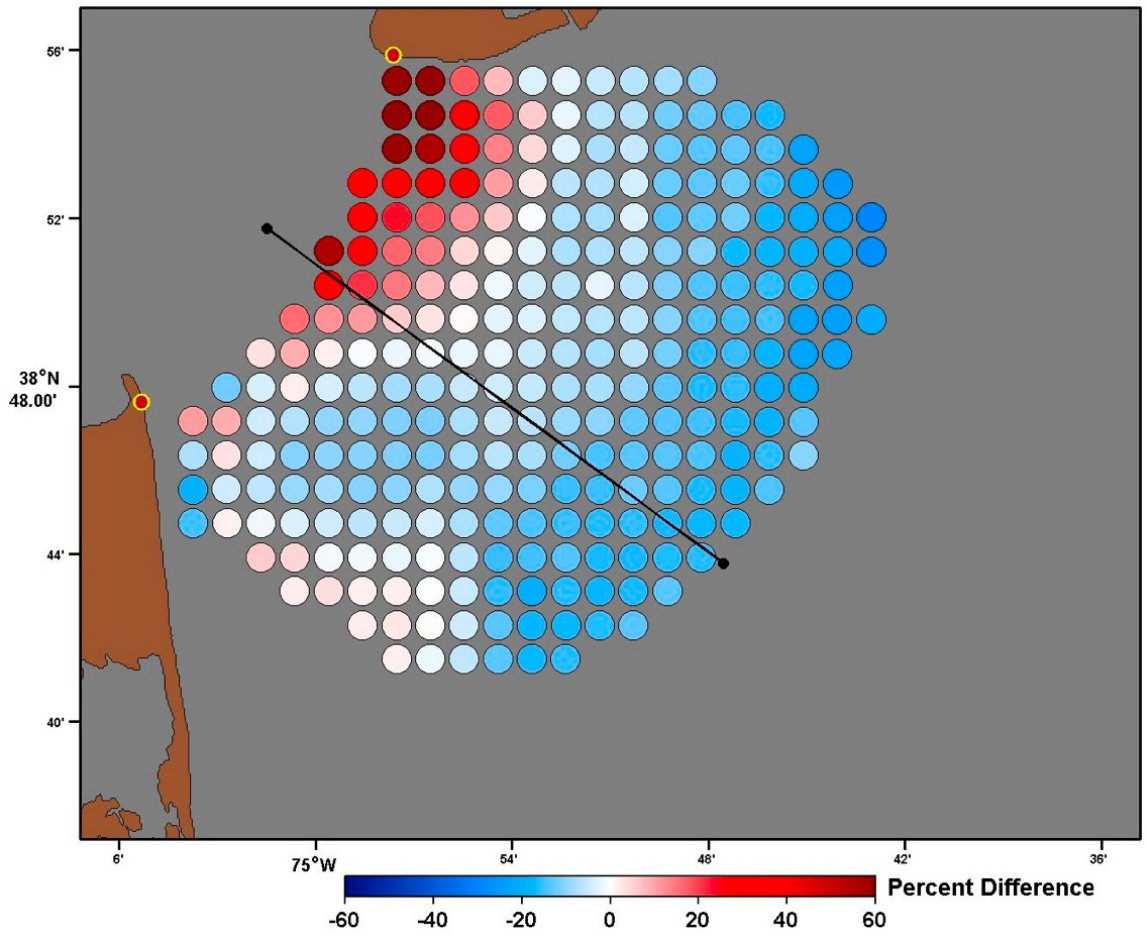

Figure 4.2: Differences between Whitney and Garvine (2008) model depth–averaged M2 r_a and near–surface HF radar M2 r_a at all radar grid locations with a minimum of 80% coverage in time. Model values were linearly interpolated to the radar grid. Circle colors show $(r_a^{model} - r_a^{radar})$ normalized by r_a^{radar} and expressed as percentages.

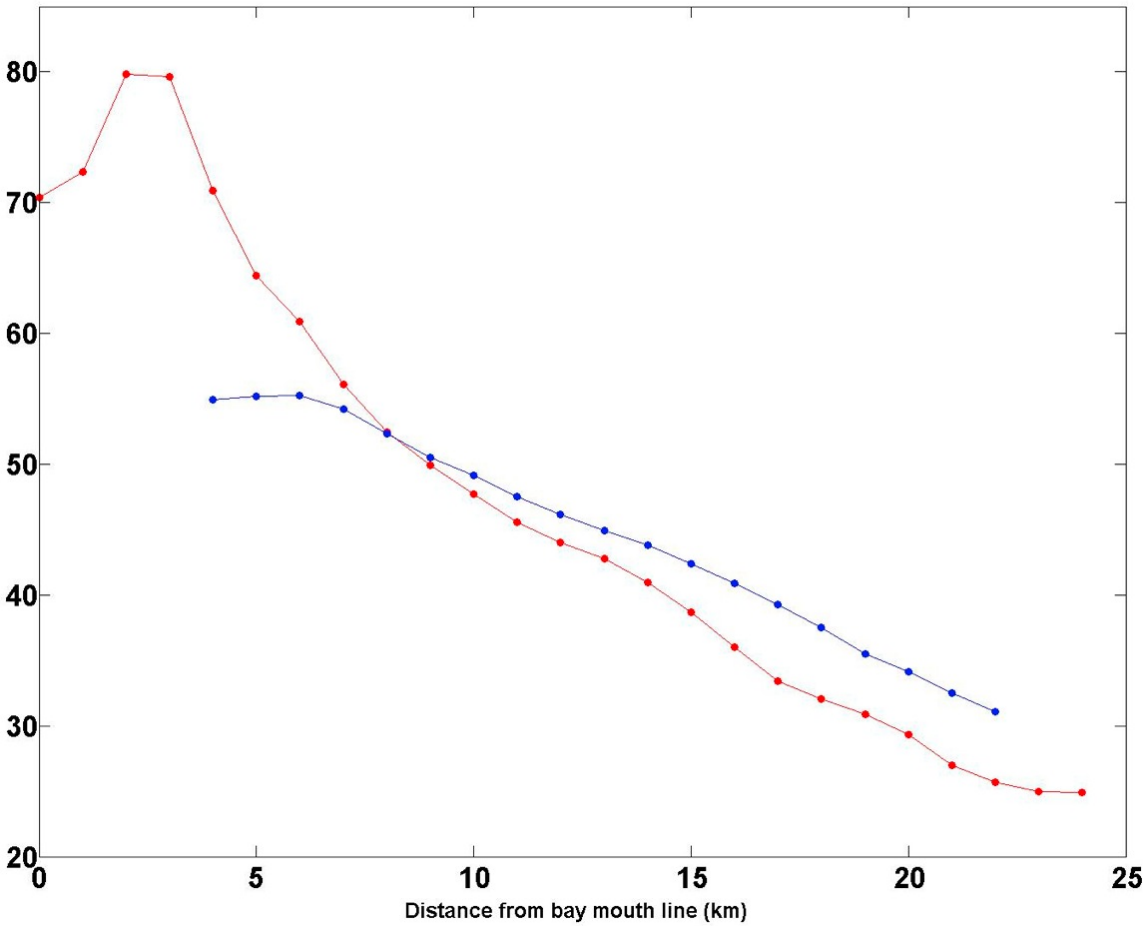

Figure 4.3: Profiles of M2 r_a along a line perpendicular to the line across the Delaware Bay mouth (black line shown in Figure 4.2) from the Whitney and Garvine (2008) model (depth–averaged, in red) and from HF radar tidal fits (near–surface, in blue). All values are in cm s^{-1} and were spatially interpolated at 1 km intervals along the profile line.

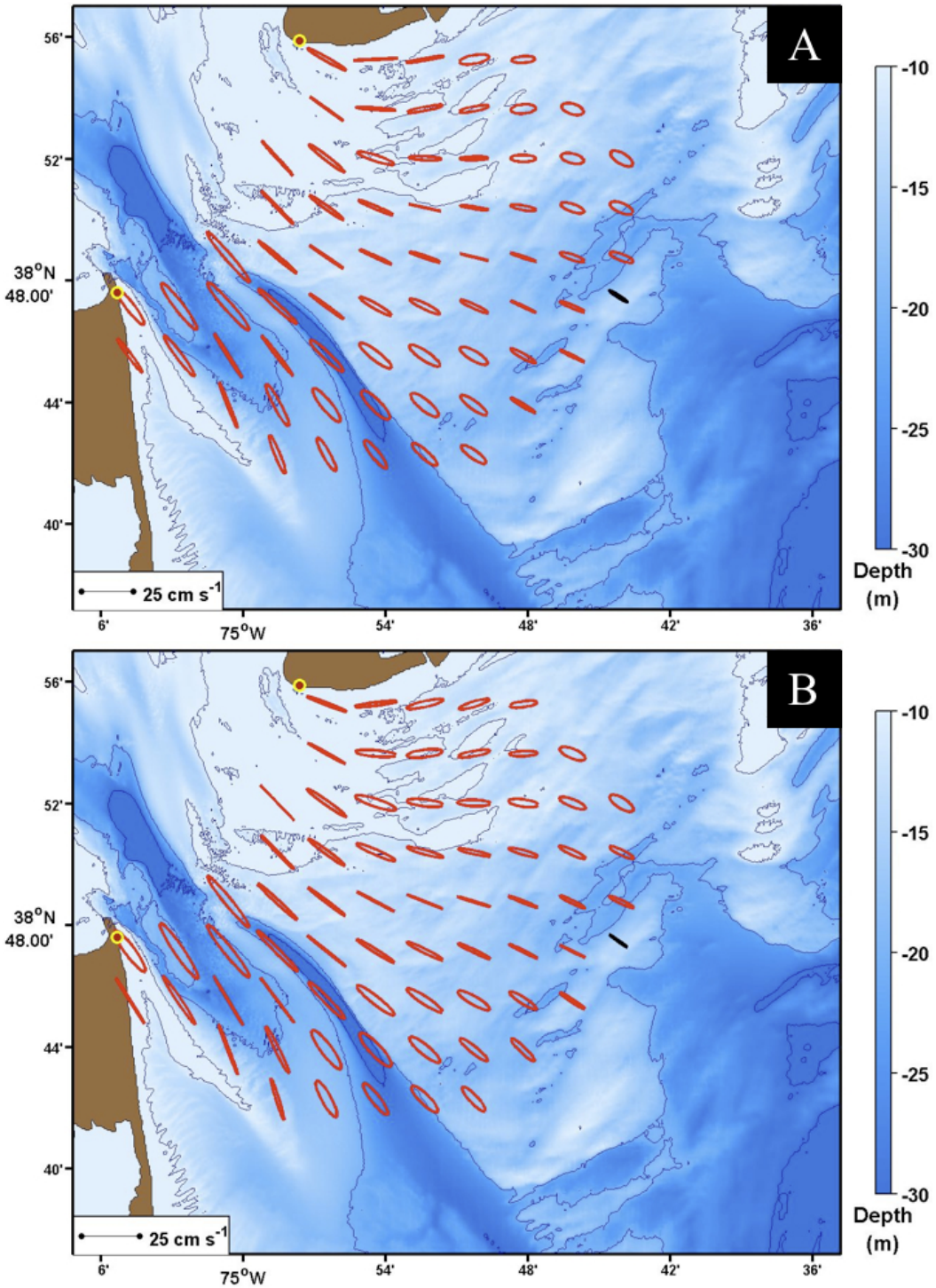

Figure 4.4: N2 (panel A) and S2 (panel B) tidal ellipses for period 1 October 2007 through 31 May 2008. For clarity, only ellipses at every second analysis location are shown. Historical ellipses reported by Münchow *et al.* (1992) are shown in black.

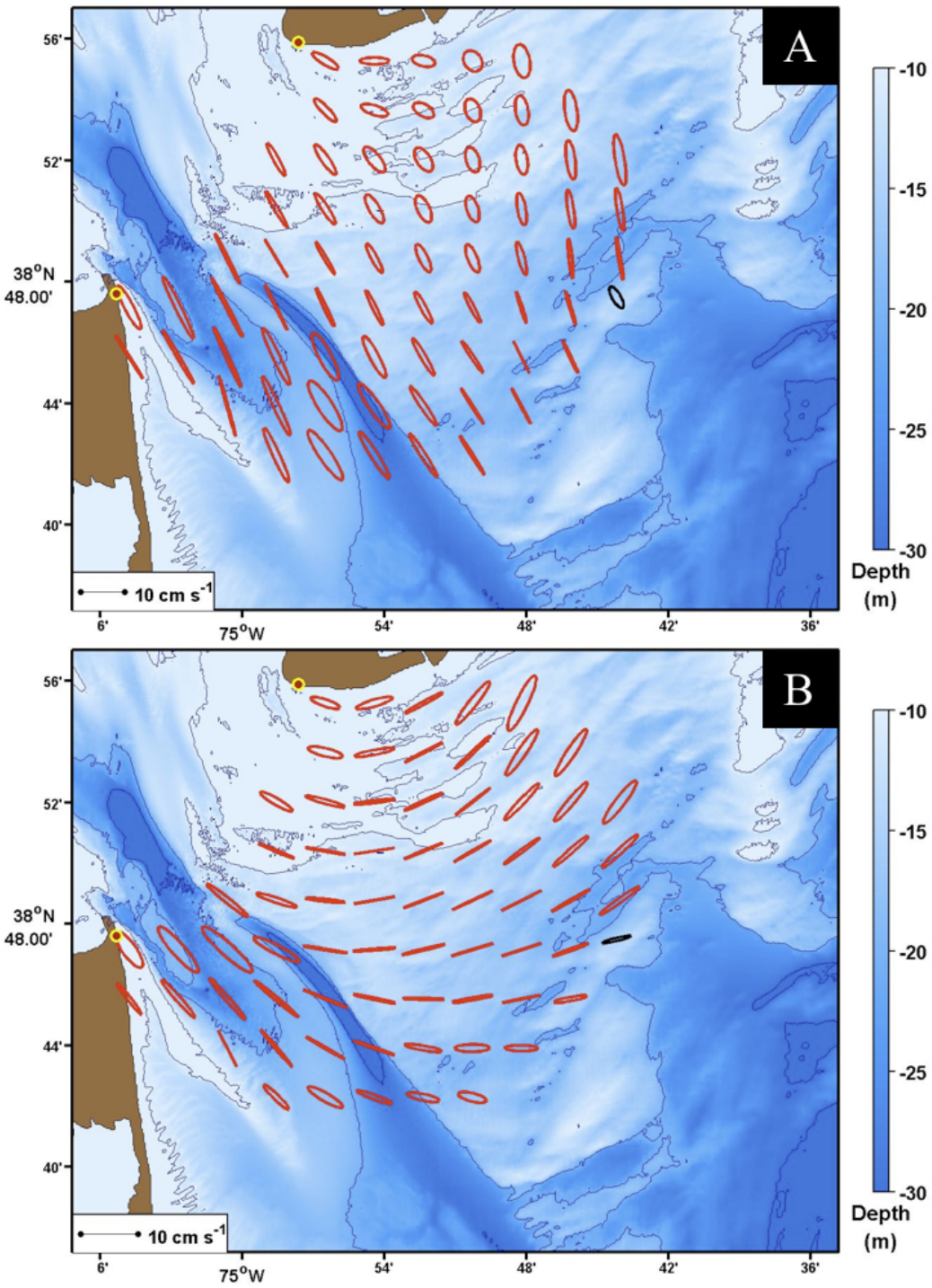

Figure 4.5: K1 (panel A) and O1 (panel B) tidal ellipses for period 1 October 2007 through 31 May 2008. For clarity, only ellipses at every second analysis location are shown. Historical ellipses reported by Münchow *et al.* (1992) are shown in black.

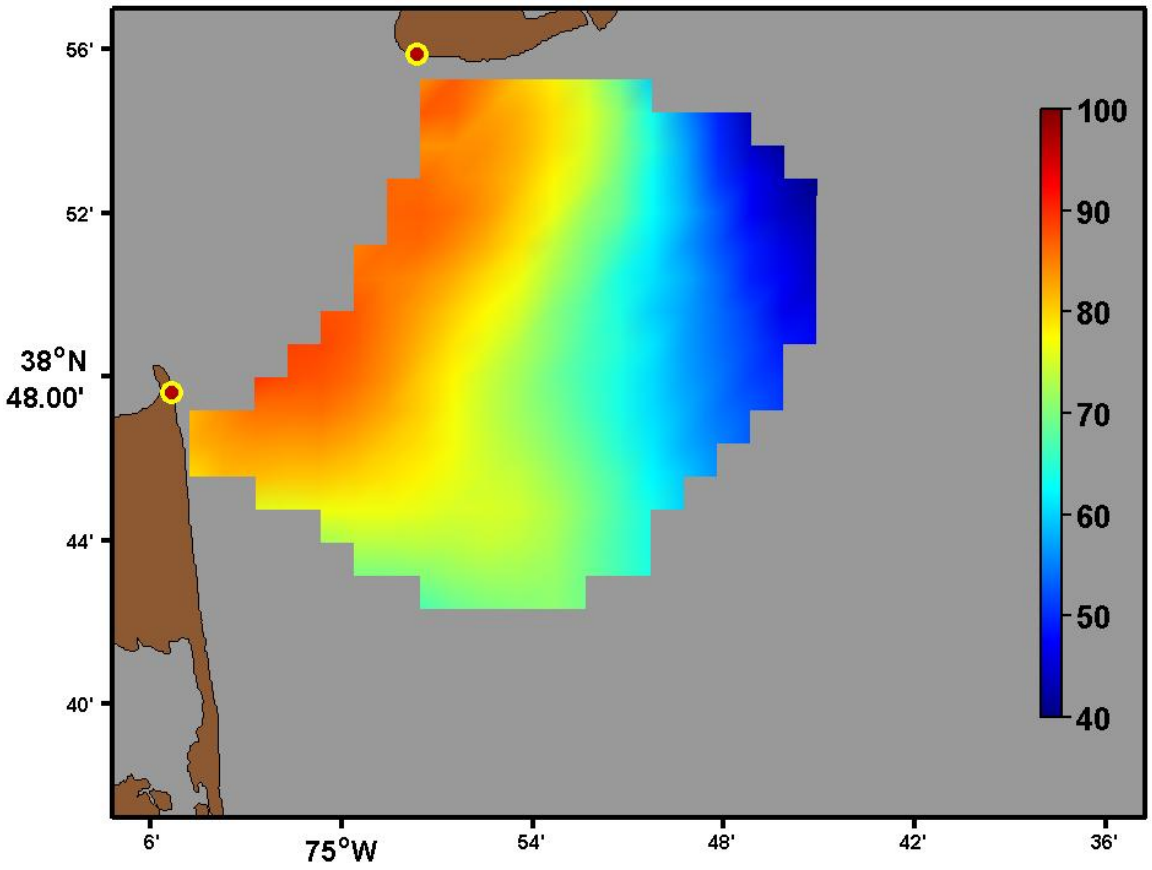

Figure 4.6: Color contours of percent variance explained by the five constituent tidal fit for the period 1 October 2007 through 31 May 2008.

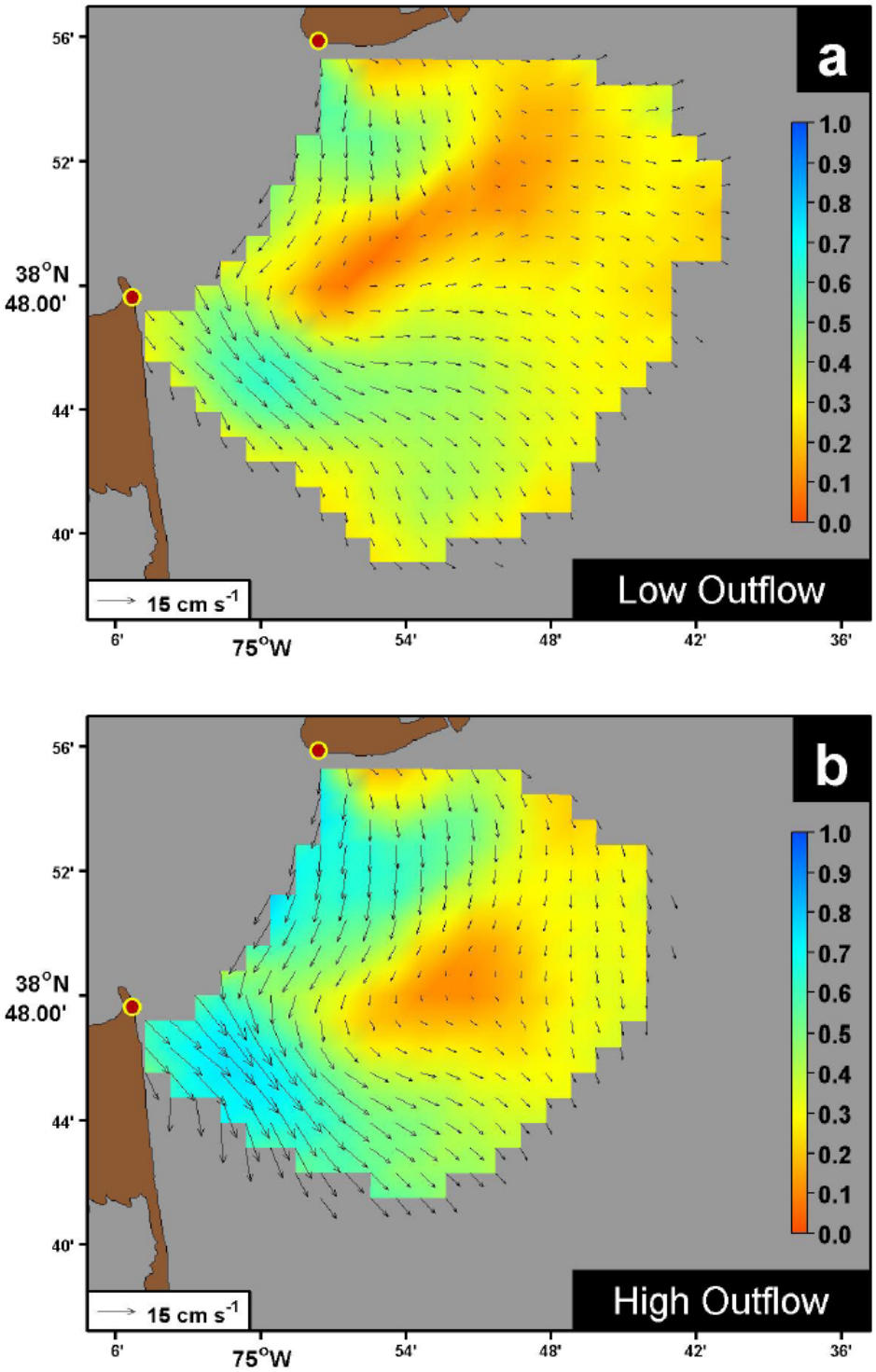

Figure 4.7: Mean HF radar surface currents (black vectors) overlaid on color contours of the ratio of the mean current speed to the magnitude of the standard deviation for (a) the low outflow period, and (b) the high outflow period.

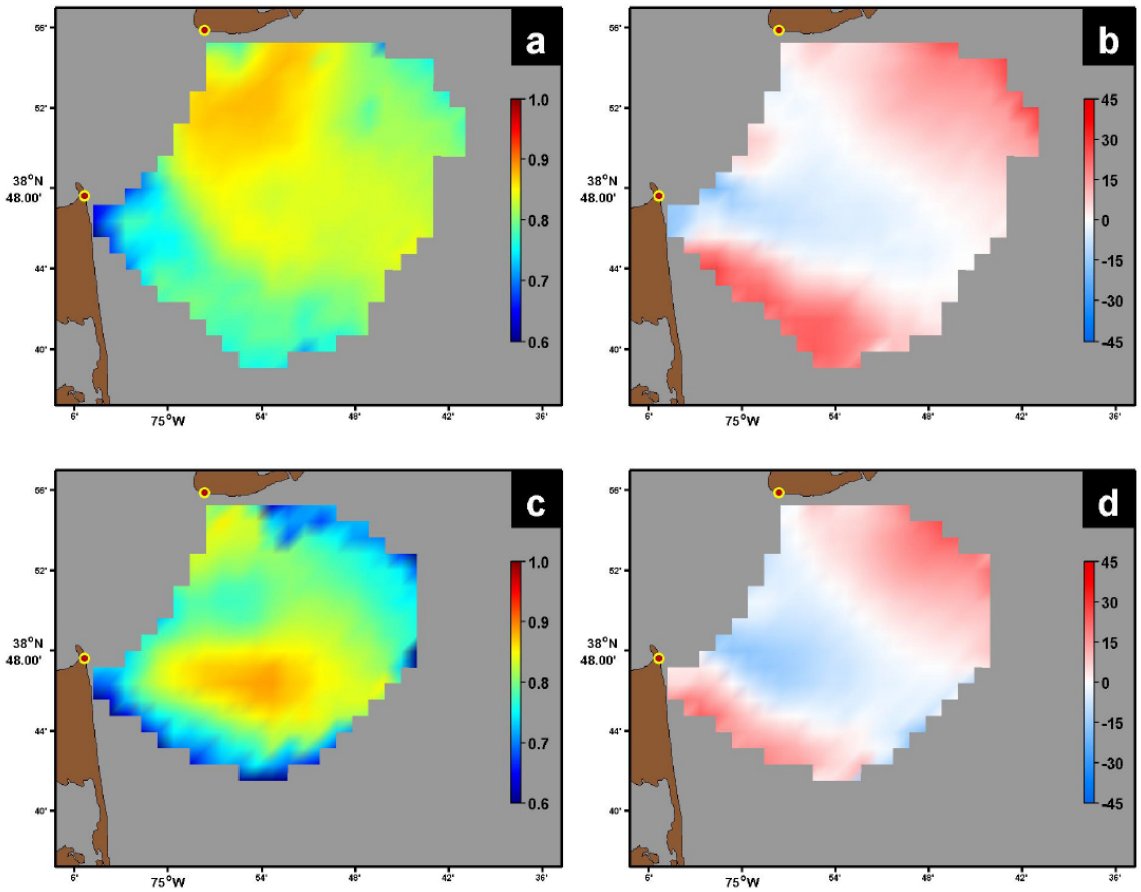

Figure 4.8: Maps of σ_{mag} and σ_{phase} (degrees) for correlations between surface currents and WRF 10 m wind stress. Surface current and wind stress vector time series were 40–hour low–pass filtered. Negative σ_{phase} values indicate currents to the right of the winds. (a) σ_{mag} for the low-outflow period ; (b) σ_{phase} for the low-outflow period ; (c) σ_{mag} for the high-outflow period ; (d) σ_{phase} for the high-outflow period.

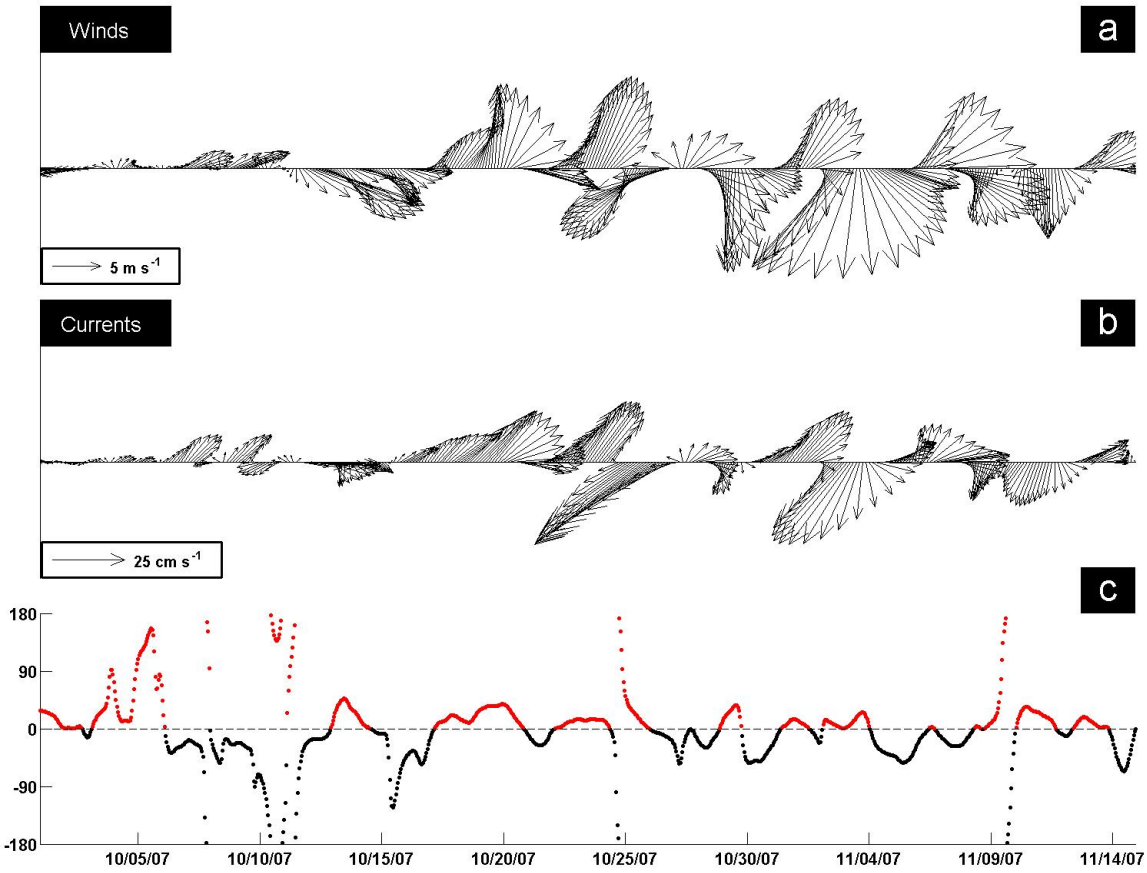

Figure 4.9: Wind and surface current time series at point 'A' in Figure 4.14 for the low outflow period: (a) 40–hour low–pass filtered WRF winds at 10 m; (b) 40–hour low–pass filtered surface currents from radar; (c) Direction difference in degrees (currents minus winds). Points shown in red are for times when the current was to the right of the wind.

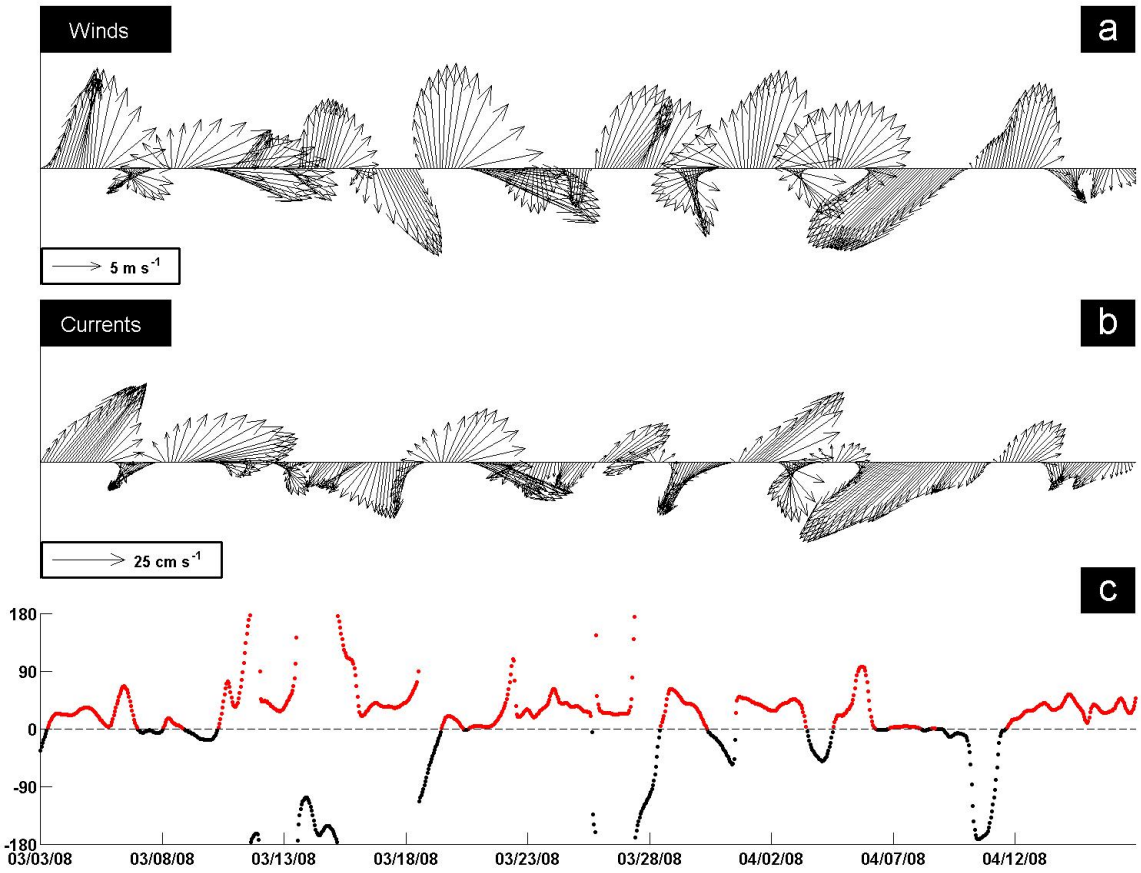

Figure 4.10: Wind and surface current time series at point 'A' in Figure 4.14 for the high outflow period: (a) 40–hour low–pass filtered WRF winds at 10 m; (b) 40–hour low–pass filtered surface currents from radar; (c) Direction difference in degrees (currents minus winds). Points shown in red are for times when the current was to the right of the wind.

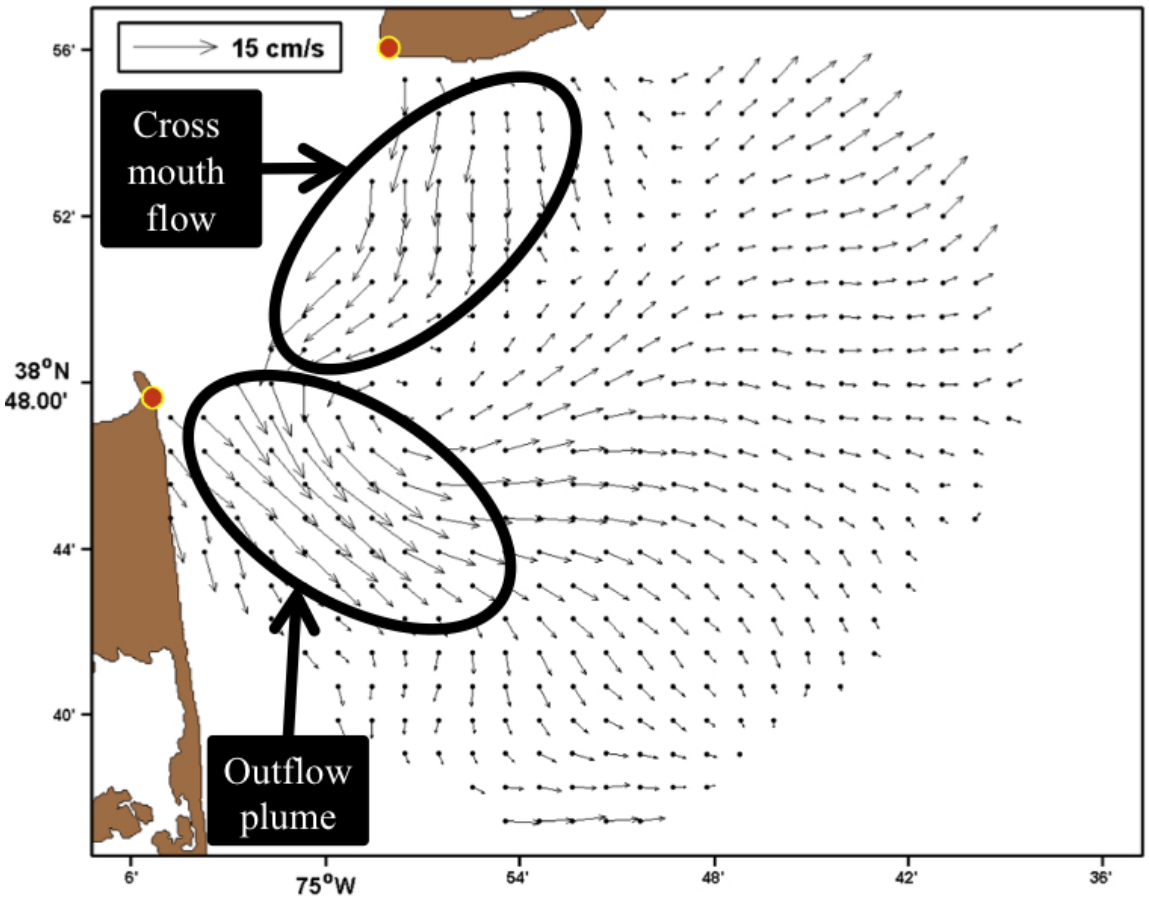

Figure 4.11: 45–day mean of HF radar surface currents during low outflow period with cross–mouth flow and outflow plume region.

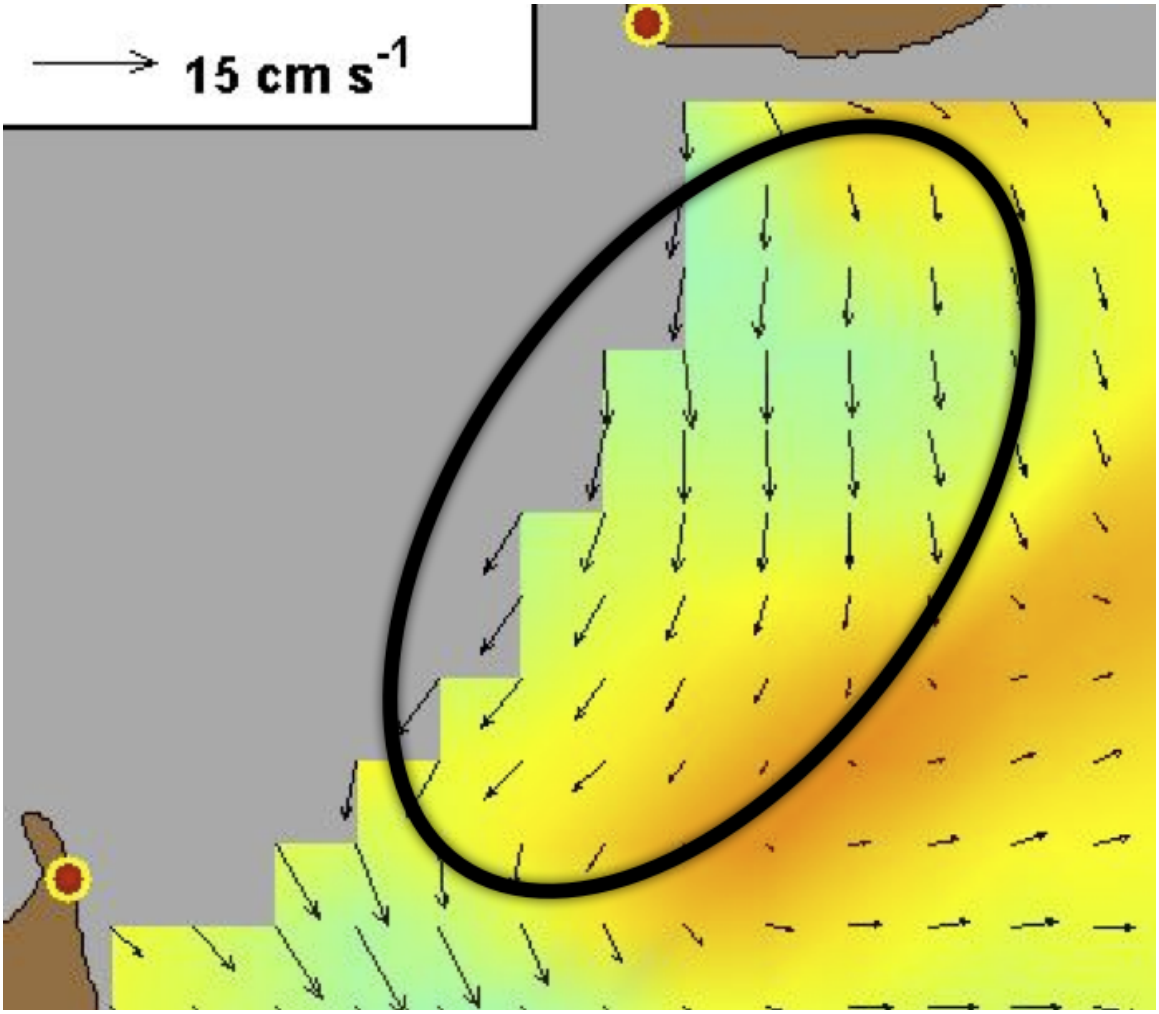

Figure 4.12: Zoomed cross–mouth flow region with low outflow period mean currents. The color contours are the magnitude of the mean divided by the standard deviation.

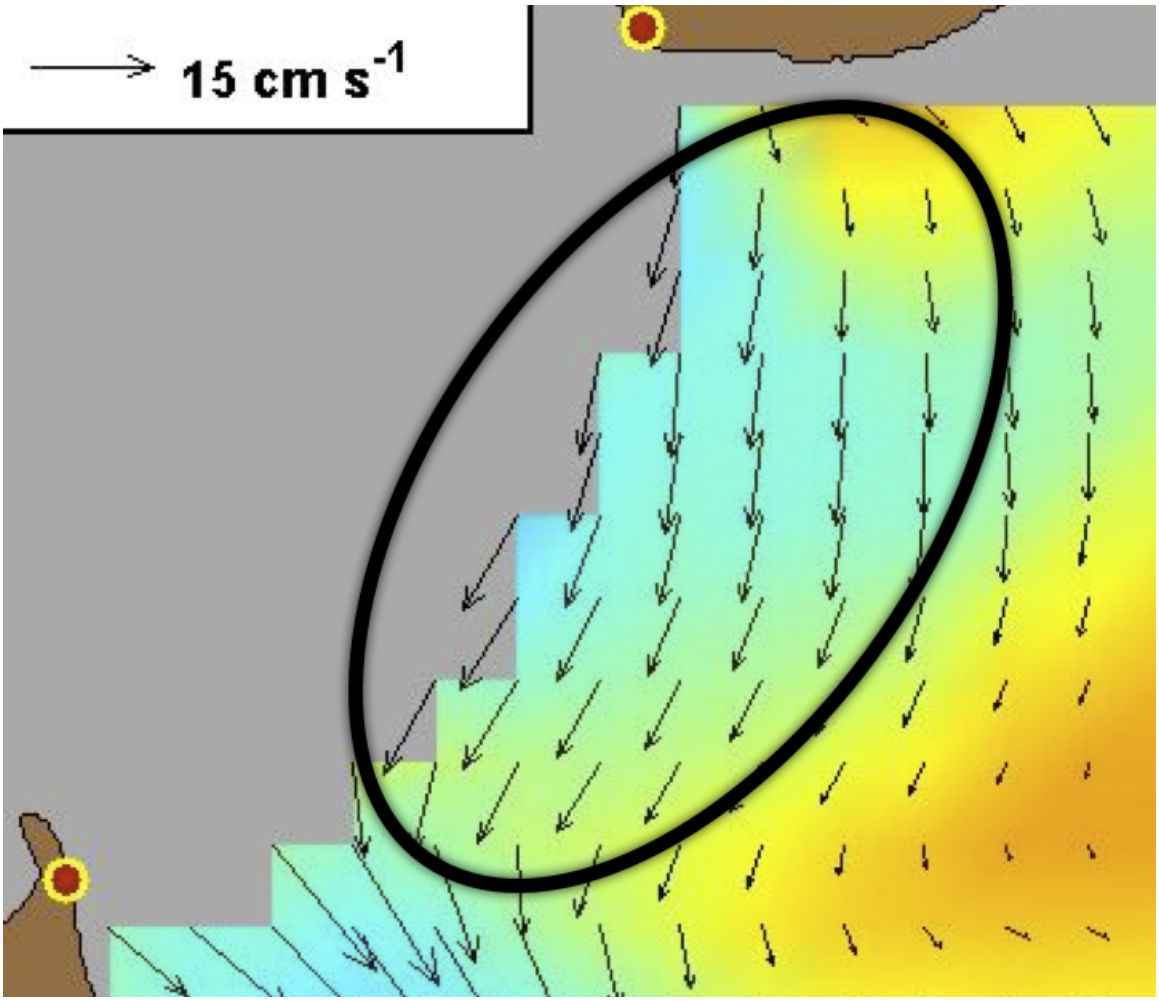

Figure 4.13: Zoomed cross–mouth flow region with high outflow period mean currents. The color contours are the magnitude of the mean divided by the standard deviation.

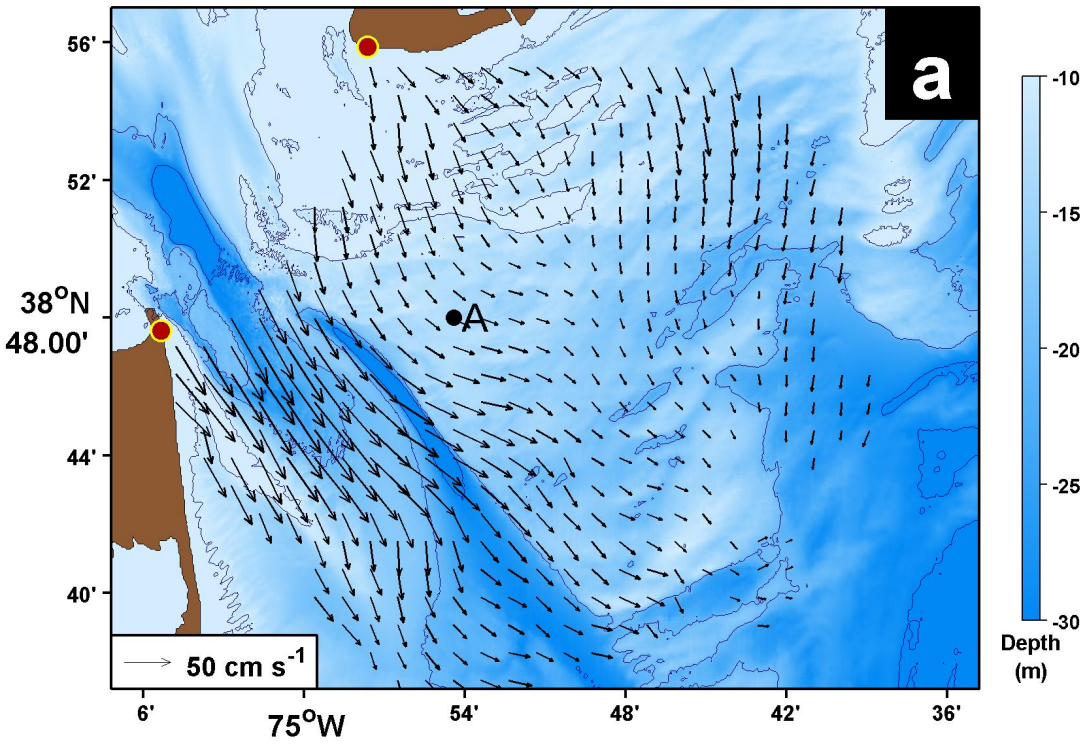

Figure 4.14: Example HF radar surface currents at the Delaware Bay mouth. Color contours show bottom topography (in m) and the two radar antenna locations are shown as red circles. The point labeled as 'A' near the center of the radar footprint shows the location where the wind–current comparisons shown in Figures 4.9 and 4.10 were made.

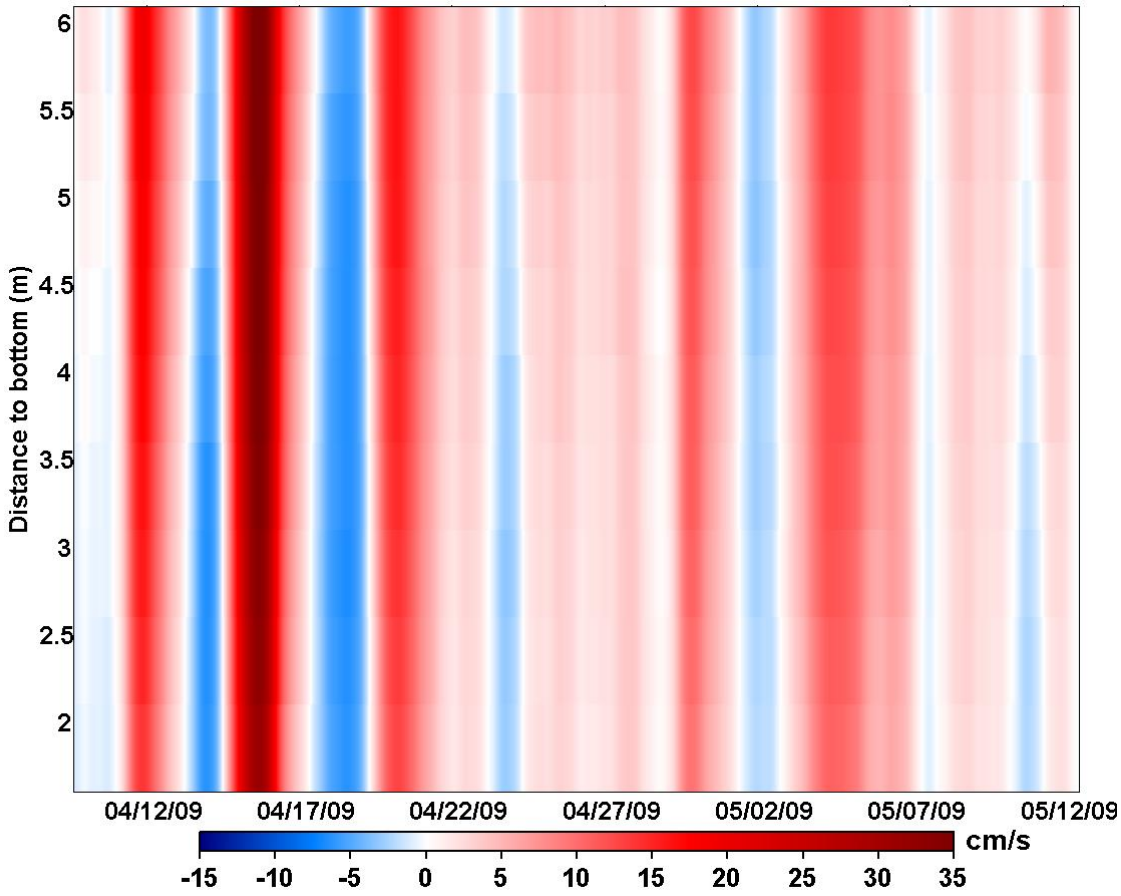

Figure 4.15: Time series of 40–hr LPF ADCP currents for the high outflow period at deployment 'C' (Figure 2.2). The magnitude of the current parallel to the line across the bay mouth is shown, with positive flow to the SW(red). Note how barotropic the flow is.

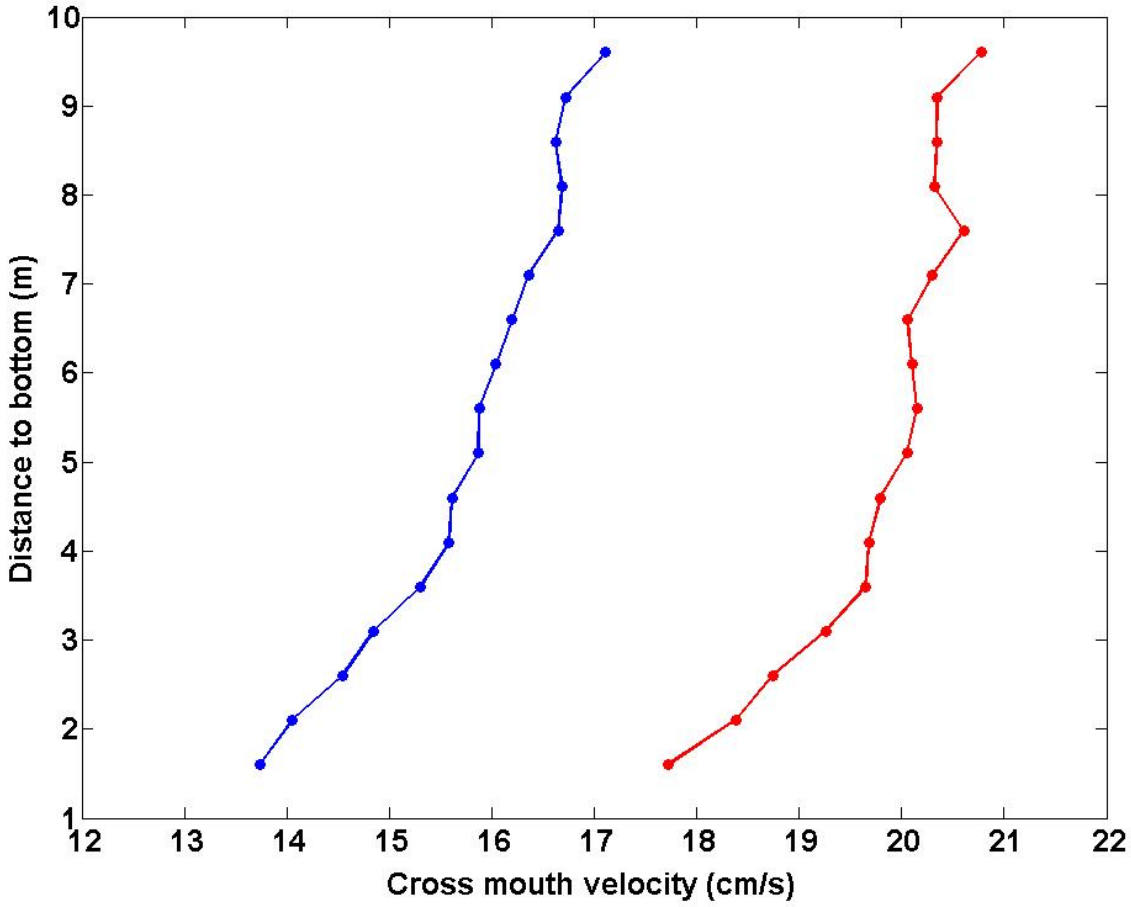

Figure 4.16: 40 hour low pass filtered ADCP currents rotated onto the cross–mouth line where southwest is positive. This ADCP location can be seen in figure 2.2 at deployment C. The velocity is constant throughout the water column. The blue plot is on April 15, 2009, 0400 GMT and the tide is flooding. The red plot is on April 15, 2009, 1000 GMT and the tide is ebbing.

Chapter 5

LAGRANGIAN PERSPECTIVE

This section examines advective transport at the Delaware Bay mouth. Lagrangian methods are the appropriate tool for this effort. The approach taken here requires the calculation of trajectories from an archive of gridded synoptic velocities from HF radar measurements. In a broad sense, the techniques used in this section include progressive vector diagrams (PVDs), residence time, escape fate, particle origin, and blobs. The results presented here provide a new look at the surface transport properties of the Delaware Bay Mouth. The transport in this region remains, for the most part, largely unknown. It was stated earlier that particle motions and their pathways are necessary for coastal ecologists, decision makers, military tacticians, and researchers.

5.1 Trajectory Calculations

The Delaware Bay high frequency radar network has measured hourly synoptic current maps since December 2006. These maps are inherently gappy in both space and time. To advect particles within the radar footprint, it is necessary to fill in these space and time gaps and create smooth two–dimensional current fields. One of the advantages of this approach is that it can be applied to any archive of Eulerian currents; for example a model output. This analysis is not limited by the two–dimensional radar data, in fact, the analysis is easily extended into the water column when three–dimensional data is available.

The method being used here is open–boundary modal analysis (OMA), which is discussed in detail by Lipphardt *et al.* (2000) and Lekien *et al.* (2004). Here, spatial gaps at each HF radar measurement time were filled using OMA. The OMA procedure objectively maps the HF radar measurements using three sets of basis functions that are truncated at a specified spatial resolution. Dirichlet modes (with zero horizontal divergence) represent the flows vorticity structure. Neumann modes (with zero relative vorticity) account for horizontal divergence, which is important in tidally dominated flows such as Delaware Bay. Boundary modes are used to represent the normal flow through the analysis domain open boundaries. Note that the Dirichlet and Neumann mode sets are orthogonal and complete. We are using the OpenMA Matlab toolbox to produce this finite set of modes, which are determined by the size and shape of the domain, and the smallest spatial scale. For our region of interest, the OMA modes has a smallest spatial scale of 5 km, which is roughly one–fourth the width of the bay mouth and qualitatively smaller then the majority of processes that occur in the area. With this minimum spatial scale of 5 km, there is a resulting set of 18 Dirichlet modes, 27 Neumann modes, and 21 boundary modes. The subsequent Lagrangian analyses span several time periods, where OMA velocities were calculated, but all utilize the same set of OMA modes. Figure 5.1 shows the lowest and highest order modes of all three mode types.

Unrealistic currents can occur in regions of irregular data density, such as near the antenna locations on the polar coordinate radial grid. It is unknown how this large amount of localized data can bias currents in this region. The (u,v) current velocity close to the radars can become overdetermined by this high data density. Thus, one should avoid small regions that are highly sampled by adjusting the weight factors to account for the contributions of each radial measurement to the fit (Kaplan *et al.* 2007).

Figures 5.2 and 5.3 show the OMA vectors (black) and the HF radar vectors

(red) at the same locations. There is an excellent agreement between the OMA and HF vectors. This is to be expected since the same radial data goes into both data products and qualitatively there is little difference between a OMA produced surface current map and a map produced with the CODAR software when there are few gaps in the data.

Our simulated trajectory analysis utilizes hourly archives of surface velocities from the OMA objective mapping. The discrete equations were integrated using an adaptive time-step Runge-Kutta scheme (Matlabs ode45 function). The coarsest time step was chosen to be the same as the HF radar archive time interval 1 h for the Delaware Bay mouth. Velocities were interpolated when necessary using a bilinear scheme in space and a linear time interpolation scheme (Matlab interpn function). Trajectory integrations required both space and time interpolation. Because only horizontal velocity measurements were available, all computed paths are near surface and two dimensional, and vertical particle motion was ignored. No attempt was made to account for diffusive processes or to parameterize subgrid scale effects.

5.2 How Accurate are these Trajectories

It is natural to question the appropriateness of this approach. As noted previously the comparisons between HF radar and ADCP velocities at the Delaware Bay were within reasonable limits for the RMS differences. This, unfortunately, does not mean that trajectories derived from the HF radar velocity archive compare equally favorably with drifter observations. For example, Huntley *et al.* (2010), compared trajectories from a high resolution data assimilating numerical model of the South China Sea with near surface drifter data. The Eulerian predictability horizon of the model was three days, but the Lagrangian predictability horizon was found to only be one day. HF radar comparisons with actual drifters in Santa Barbara Channel were performed by Ohlmann *et al.* (2007). That analysis was primarily focused on comparing HF velocities with those from near–surface drifters.

They found RMS differences of roughly 5 cm s^{-1} with occasional values as high as 20 cm s^{-1}. The question is: do these relatively small errors in the Eulerian velocities accumulate along the particle paths and produce large displacement errors given a sufficient amount of time?

It should be noted that the Huntley *et al.* (2010) study was carried out in deep water near the Kuroshio with modeled velocity data. In Ohlmann *et al.* (2007), the region of interest was Santa Barbara Channel which has energetic mesoscale circulation features. However, the temporal scales of the trajectories in the Ohlmann *et al.* paper are on the order of hours. In contrast, the study area in Delaware Bay is tidally driven with a research area smaller than the other study areas.

In any event, the HF radar archive is the only observed dataset available for Lagrangian analysis. Much of the subsequent analyses relies on large numbers of simulated trajectories. If the velocity errors in the observation have a strong random component, then the statistics of the simulated trajectories may be better than comparisons of individual trajectories.

5.3 How Useful are Progressive Vector Diagrams (PVDs) for Studying Coastal Ocean Transport?

Here I summarize results reported in Carlson *et al.* (2010).

Progressive vector diagrams (PVDs) have been used to estimate transport in the coastal ocean from point measurements of velocity time series, strictly they only approximate true particle trajectories in regions where the currents are spatially uniform. Currents in most coastal regions vary significantly in both space and time, making coastal transport estimates from PVDs questionable. We assess the time scales over which PVD paths computed from velocity time series at fixed points separate from particle trajectories computed from two–dimensional measured horizontal currents that vary in both space and time. PVDs and particle trajectories

separate by 1 km over a mean time period of 7–10 h with no significant month–to–month variation. The separation time statistics presented here should serve as a strong caution for investigators motivated to estimate transport using only point measurements. The fact that PVD's are so widely used by ecologists proves that there is a pressing need for Lagrangian data even so far as to accept PVD's as the Eulerian answer to the Lagrangian question.

5.3.1 PVDs in the Coastal Ocean

Ocean velocity time series typically consist of orthogonal velocity components (north/east or along/across shore) measured at a fixed location, often using a current meter or current profiler. Typically, current meters measure velocity at a fixed depth, and current profilers measure velocities throughout the water column at high temporal resolution, but over a single location. However, costs associated with maintenance and deployment limit the number of instruments available to only a few in a given domain. Therefore, the horizontal resolution of a dataset is usually very coarse. Whereas, velocity time series from several locations can provide important information about the time scales of the flow at a few locations, estimates of the transport of passive particles by the measured flow are often desired. To this end, the flow is taken to be spatially uniform with the observed temporal variability imposed over the entire spatial domain. Under this assumption, a pseudo particle path, termed a PVD, can be constructed by integrating the measured velocities over a specified time interval to obtain a position vector (see Emery and Thomson 2001, p. 165 and 186; Tomczak 2000).

However, uniform spatial currents rarely persist over broad ocean regions, particularly near the coast, so the main assumption on which the PVD analysis rests generally is invalid. Consequently, the usefulness of PVDs for studying coastal transport problems is problematic. Despite this obvious and well established limitation, PVDs are still used to examine a number of different coastal physical and

biological processes including larvae dispersal (Epifanio et al. 1989; Ben-Tzvi et al. 2007; Fiechter et al. 2008), sediment transport (Ogston et al. 2004), and current variability (Berman et al. 2000). Even in these applications, the limitations of PVDs often emerge. Epifanio *et al.* (1989), for example, noted that PVDs at the Delaware Bay mouth (where tidally dominated currents vary substantially in space) are not good surrogates for particle trajectories. Figures 2 and 3 in Epifanio *et al.* (1989), show two dramatic examples of PVD paths crossing onto land at the central New Jersey coast during one 46-day period in 1983.

If transport studies involving PVDs should be restricted only to regions of spatially uniform flow, why have they been used for coastal ocean studies, where the currents are known to vary spatially due to the combined effects of winds, tides, bottom topography, and coastline geometry? The answer is lack of synoptic current measurements. Most historical coastal circulation studies rely on point measurements of velocity time series from current meters or acoustic Doppler current profilers. Point measurements provide an incomplete picture of the spatially varying flow features inherent in coastal regions, making it natural to question their ability to describe transport in the vicinity of the sensors. Because little is typically known about the spatial scales of velocity variability in the neighborhood of in situ sensors, the time and space scales over which PVDs might provide useful transport estimates from sensor measurements could not be determined previously.

HF radar measurements offer an opportunity to independently assess the appropriate time and space scales over which PVDs might be applied in the coastal ocean. Obviously, if HF radar measurements are available, particle trajectories could be computed directly, and PVDs would not be required.

The purpose of a PVD assessment based on HF radar measurements is to gauge the uncertainties associated with their use in coastal areas, where HF radar measurements are not available and offer some guidance to investigators who may

want to use time series of velocities at a single point to estimate transport.

5.3.2 Computing PVDs and Statistics

For our analysis region, trajectories and PVDs were computed from objective mappings of HF radar velocity measurements. To compute PVDs, velocities over the entire integration time interval were chosen as the time–dependent velocities from the record at the PVD launch location. This is equivalent to assuming that the velocity field is spatially uniform, with time dependence specified by the velocity time series at the launch location. In addition, particle launch locations did not coincide with OMA grid points, hence PVD calculations required spatial interpolation, but always to the particle launch location in contrast to the simulated trajectory which uses the instantaneous location. Any trajectory/PVD pair was excluded from the analysis if the trajectory reached the domain boundary or the PVD crossed over to land before they separated by 1 km.

At the Delaware Bay mouth, the analysis domain boundaries were mostly open, so particles could escape. We used a grid of nine initial positions near the center of the analysis domain (see figure 5.4) to allow for longer particle residence times. Particles were launched hourly over a 72-h analysis period in each month and tracked for up to 48 h. A total of 648 particles were launched each month. A particle was considered to have escaped as soon as it entered any velocity grid cell that did not have valid velocities at all four cell corners. Temporal and spatial gaps in the radar coverage required careful choices for each monthly analysis interval. Because the radar coverage here had substantial spatial variability an additional criterion was used to ensure enough spatial coverage existed to constrain the OMA maps. For each hourly map in an analysis period, at least 65% of all mapping grid points were required to be no further than 5 km from a radial velocity measurement from each radar site. Most of the time, the spatial coverage was much better than this. Table 5.1 shows the time intervals (all times are GMT) for each month of the 10-month

analysis period (January 2008 through October 2008). For each monthly analysis period, Table 5.1 also shows the minimum value for the percentage of mapping grid points within 5 km of radial velocity measurements from each site (column labeled Minimum %).

	Start		End		
	Day	Hour	Day	Hour	Minimum %
January	11	0200	16	0200	84.0
February	23	2300	28	2300	84.8
March	26	2300	31	2300	93.7
April	11	0300	16	0300	93.3
May	17	1000	22	1000	91.6
June	18	2300	23	2300	81.1
July	18	1200	23	1200	77.1
August	8	0000	13	0000	68.6
September	10	0000	15	0000	66.5
October	16	1000	21	1000	77.3

Table 5.1: Time intervals for each month of the 10-month analysis period (January 2008 through October 2008). All times are GMT. The last column shows the minimum value for the percentage of mapping grid points within 5 km of radial velocity measurements from each site.

For all pairings of trajectories and PVDs, two simple statistics were computed: the time for the trajectory, and PVD paths to separate by 500 m and 1000 m. Monthly mean separation times are reported for both analysis regions. Because the distributions of separation times had long tails (see Fig. 5.5), the 95% confidence interval for the monthly mean separation times was estimated using the nonparametric bootstrap method (Efron and Tibshirani, 1986) with 1000 samples.

Table 5.2 shows monthly mean values of 500- and 1000-m separation times and 95% confidence interval limits for these mean values for the Delaware Bay mouth. The average 1000-m separation times ranges from 6.18 to 10.2 h and the

average 500-m separation times range from 4.09 to 6.9 h. During some months, a small number of particles escaped the domain before they separated from the PVD by the specified distance. Escaped particles are considered missing values, and the number of missing values is shown in Table 5.2. These should be compared with the total number of particle launches (648) in each month. Figure 5.5 shows histograms of the 500-m and 1000-m separation times for all particles launched in September 2008. These histograms show distributions with broad peaks and long tails, which were similar for all the months we studied. Again, the 95% confidence interval limits were estimated using the bootstrap technique.

	500 m				1000 m			
	Mean	95%	interval	Missing samples	Mean	95%	interval	Missing samples
January	4.93	4.75	5.11	0	7.81	7.51	8.11	0
February	4.64	4.47	4.83	0	6.94	6.69	7.22	3
March	5.19	5.04	5.34	0	7.45	7.22	7.68	0
April	4.78	4.62	4.94	0	7.52	7.24	7.83	1
May	4.79	4.63	4.96	0	7.59	7.31	7.88	2
June	4.52	4.34	4.71	0	6.56	6.30	6.85	2
July	4.09	3.97	4.21	0	6.18	5.97	6.40	4
August	5.61	5.41	5.81	3	8.65	8.31	9.02	14
September	6.90	6.66	7.14	0	10.20	9.88	10.54	2
October	4.85	4.70	5.01	0	7.76	7.45	8.05	3

Table 5.2: Delaware Bay monthly mean separation times (in hours) for 2008. Particles that escaped the domain before 500 m and 1000 m separation could occur were treaded as missing samples.

5.3.3 Results

We assessed the accuracy of surface transport estimates based on PVDs using synoptic surface currents measured by HF radar in two coastal regions with distinctly

different flow regimes over time intervals spanning several months. The errors that result from assuming that PVDs represent true particle trajectories were assessed by computing the times for PVDs and trajectories to separate by 500 and 1000 m. PVDs deviate from HF radar trajectories by 1000 m over time periods of less than 12 h (monthly mean values of 6–10.2 h for the Delaware Bay mouth). These monthly mean separation times do not vary significantly from month to month, suggesting that seasonal influences are minimal.

Carlson *et al.* (2010) showed that these separation time statistics are similar for two coastal regions with marked differences in surface circulation characteristics. They reported a similar analysis for the northern terminus of the Gulf of Eilat, which is a nearly rectangular, deep, semi–enclosed basin in the northeast region of the Red Sea. Circulation in that gulf is driven by tides, winds, and thermohaline forcing. The average time required for the PVDs and trajectories to separate by 1000 m ranges from 6.13 to 7.94 h. The 500 m separation time ranges from 4.45 to 6.28 h.

We assessed the accuracy of surface transport estimates based on PVDs using synoptic surface currents measured by HF radar in two coastal regions with distinctly different flow regimes over time intervals spanning several months. The errors that result from assuming that PVDs represent true particle trajectories (an assumption that is only strictly accurate when the currents are spatially uniform) were assessed by computing the times for PVDs and trajectories to separate by 500 m and 1000 m. For both regions studied, PVDs deviate from true trajectories by 1000 m over time periods of less than 12 h (monthly mean values of 6–7.5 h for the Gulf of Eilat and 6–10.2 h for the Delaware Bay mouth). These monthly mean separation times do not vary significantly from month to month, suggesting that seasonal influences are minimal. It is noteworthy that these separation time statistics are so similar for two coastal regions with marked differences in surface circulation characteristics.

Because both trajectories and PVDs were computed using the same velocity archives and the same numerical algorithms, details about how they were computed cannot explain the separation of their paths. This separation is due solely to the spatial variability of the surface currents and the accumulating effect of this spatial variability as particles move over time.

Studies that involve surface transport in the coastal ocean focus on events spanning days to weeks. These are time periods where significant net transport can occur. Because these results demonstrate that PVDs accumulate errors of 1 km or more during the first 12 h, they clearly cannot provide useful surface transport estimates over time periods longer than this. These results demonstrate that, although spatial variations in coastal surface currents may not readily indicate their effect on particle transport, their effect on trajectories is significant and develops rapidly over several hours. No simple remedy exists to salvage the PVD for applications involving coastal transport; where surface currents vary spatially, this variability must be measured or modeled, and its influence on particle paths must be explicitly accounted for when trajectories are computed.

5.4 Residence Time

This section describes an effort to examine the movement of water particles at the Mouth of the Delaware Bay. The basic goal is to find where particles come from and where they go in the analysis domain for specified time periods. The huge amount of data produced will be examined with the use of synoptic Lagrangian maps. This method was used to examine surface transport in Monterey Bay by Lipphardt *et al.* (2006). These maps will be used to represent the Lagrangian trajectory information in the forms of residence time and escape fate plots.

5.4.1 What do Residence Times Tell us About the Coastal Ocean?

The interpretation of current variability in the coastal ocean has broad applicability to both practical problems and fundamental scientific questions. The practical issues that can be addressed include oil spill risk assessment, harmful algal bloom studies, and search and rescue operations. These efforts are mainly concerned with the tracking of surface particles near a coastal area. Users require answers to three questions about a particle: 1) Where does it go?, 2) Where did it come from?, and 3) How long does it take to transit its path? We attempt to answer these questions.

5.4.2 Computing Residence Time and Escape Fate

Particles are initialized on a one–half km interval grid over the bay mouth's surface, as shown in figure 5.6. The particles are tracked from their initial locations (the black dots) to the boundary locations (the red dots). We see from this figure that our domain is composed of entirely open boundaries. A particle is considered at the boundary once it reaches a grid point that does not have other grid points on all sides (the red dots). Once a particle leaves our domain, it dies and can not return. We use this rule since we do not have the capability to track particles outside the domain.

Here we analyze 91 days of OMA current maps for three months in 2008: March, April, and September. 2,904 particles are initialized every hour for 2,184 hours resulting in 6,342,336 Lagrangian trajectories. Due to the overwhelming amount of information, it is necessary to use a unique data representation method that compresses the vast amount of data into an easily understandable format. The amount of Lagrangian data available to use far exceeded even the most well funded observational drifter studies. The high spatial resolution of the radar measurements produced a large amount of simulated Lagrangian measurements. In turn, this revealed considerable structure in the residence time maps. However, the volume of

data also makes interpreting the results difficult.

The five types of synoptic Lagrangian maps computed here are: 1) residence time, which simply calculates the time it takes for a particle to reach a boundary, 2)backward residence time, shows the time a particle takes to get from a boundary to a point, 3) total residence time, is the total time a particle remains in the domain, i.e. the sum of the forward and backward residence times, 4) escape fate, which shows the location an initialized particle leaves the domain and, 5) particle origin, is the location a particle enters our domain. The escape fate and particle origin figures are produced by apportioning the boundary into 10 km segments and recording the initial locations of the particles to pass through each segment.

5.4.3 Typical Residence Times

Figure 5.7 shows an example of a typical forward, backward and total residence time synoptic Lagrangian maps for the mouth of the Delaware. For this example, there is a patch of high (greater than 100 hrs) residence time values in the southern portion of the domain. There is also a boundary of lower residence time values that surround the high values. These lower values are due to the tidal currents pushing particles closer to the boundary and out of the domain relatively quickly. The phase of the tide plays a critical role in determining the structure of these particle residence features. This figure is an example of when the tidal currents are at a maximum and switching from ebb to flood. Animations of this figure show the high residence patch moving with the phasing of the tides. For a flood tide we would see the higher particle residence near the ocean boundary and lower values on the bay side. The reverse is true for an ebb tide; lower residence times occur along the ocean boundary and higher residence times along the bay side (see Figure 5.8).

Figures 5.7, 5.8, and 5.9 also show particle escape fate and origin plots. These figures depict the respective exit and entrance locations for the forward and backward residence time calculations. These plots requires some explanation. The

boundary is divided into equal arbitrary boundary segments. For this example, the segments are ten km in length. The colored pixels within the domain imply a particle from that location will enter or leave the footprint through the boundary segment of the same color. This is an extremely powerful descriptive tool especially when used in conjunction with the residence time plot. The escape fate plot in figure 5.7 shows a large area where the particles will leave the domain through the blue and purple colored boundary segment. Additionally, we see in the particle origin plot a large section of the domain colored dark red, meaning particle from this area entered the domain through the southern portion of the across the mouth section.

The influence of the tides causes a large number of particles to leave the domain relatively quickly, while at the same time causing a smaller amount of particles to become 'trapped' by the canceling action of the ebb and flood tidal currents. This result is shown by figure 5.10. The plot strongly suggests an exponential relationship between the population of particles that exit and their residence time. The result that the probability of a particle to remain in the domain decays exponentially with time has not been noted before. Mathematically this is expressed as:

$$\frac{\mathrm{dn}}{\mathrm{dt}} = -\lambda \mathrm{n}. \tag{5.1}$$

Here, n is the amount of particles in the bay, t is time, and λ is the time decay constant. Integrating equation 5.1 yields

$$\frac{n(t)}{n_0} = e^{-\lambda \mathrm{t}}. \tag{5.2}$$

Figure 5.10 shows the left side of equation 5.2 for October 2007. Table 5.3 has results from five additional months. The results for additional months of residence time show differences in the λ^{-1} value. These differences may be due to seasonal differences in outflow which may decrease a particle's residence time. We see the

probability that any particle remains in the domain beyond a certain time interval, then, decays exponentially as the time interval increases.

	λ^{-1}	R^2
October 2007	27.28	0.999
January 2008	22.58	0.999
March 2008	23.87	0.998
April 2008	29.13	0.998
May 2008	22.22	0.999
September 2008	36.26	0.996

Table 5.3: Exponential fit statistics for six months of residence times. The λ^{-1} is the time decay constant for the exponential decay in hours and R^2 is a "goodness of fit" criterion, with a values of 1 indicating a perfect fit.

Do particles with long residence times follow preferred pathways? Figure 5.11 shows trajectories of particles launched hourly at a single location for seven days. The particle launch location was chosen in a region of high residence times. Particles released from this location most often exit the domain in three distinct locations: 1)through the western boundary into the Delaware Bay, 2) through the northern boundary, and 3)through the southern boundary. Generally the particles that exit into the bay do so relatively quickly while the particles which leave through the northern and southern boundaries, tend to take longer. The semi–diurnal tidal phase at launch is an important factor influencing these pathways. This is easily seen with the particles which leave the domain to the west. Thus, their exit location is determined by the phase of the tide at the time of the particle's launch. This suggests that even though they enter the bay, they will eventually exit the domain through the southern boundary in due time.

5.4.4 Seasonal Influence

The Delaware Bay experiences seasonal variability, including effects of increased freshwater inflow; in the early spring, stratification during the summer, and energetic storm events in the fall and winter (nor'easters). How does this annual variability impact particle residence times?

The tides certainly influence hourly residence time maps. Temporal averages of hourly residence time maps help reveal the effects of lower–frequency forcing. Figures 5.12, 5.13, 5.14 show monthly mean residence maps, for March 2008, April 2008, and September 2008. Note the differences in typical mean residence times between the months. Maximum mean residence for March 2008 (Figure 5.12) is around 40 hours compared to September 2008 (Figure 5.14), which shows max residence time of 60 hours. These residence time distribution differences are likely driven by changes in low–frequency forcing. Winds during both periods were variable and typically less than 5 m s^{-1}. This suggests that the higher volume of fresh water outflow in the spring (March 2008 and April 2008) drives increased surface transport reducing residence times.

The seasonal influence is more difficult to assess when examining spatial mean residence time. Figure 5.15 shows time series of spatial mean residence time for all particles in the domain (in red) with grey areas representing the one sided standard deviations from the mean. One sided standard deviations are appropriate because residence time is a positive definite quantity. The influence of changing freshwater inflow is less apparent in figure 5.15 while temporal variability over 3–10 day time periods could represent passing weather systems.

5.5 Estimating Surface Flow Deformation from Finite Area Blobs

What can simulations of blobs tell us about flow in Delaware Bay? A blob is a finite area, dynamically linked collection of trajectories that can be used to estimate kinematic quantities (using methods in appendix A). Blob simulations provide

information about the spatial variability of the flow in the immediate vicinity of a particle as it marches along it's trajectory. This may not be valuable for a single particle, but when part of an oil spill, harmful algal bloom, or finite biological population, shape changes become important.

For present purposes, the blobs are collections of particles initialized in a circle and connected by line segments. Simulated particle trajectories from archives of synoptic high frequency radar velocities are used to study time-dependent kinematic parameters for surface currents. For a specific time period, a circular blob is initialized with the HF radar surface current velocity field. OMA currents are then used to advect this blob through the domain.

5.5.1 Basic Kinematic Quantities

Velocity gradients are used to compute these kinematic quantities:

$$\begin{aligned} D &= \frac{\partial u}{\partial x} + \frac{\partial v}{\partial y}, \\ 2N &= \frac{\partial u}{\partial x} - \frac{\partial v}{\partial y}, \\ 2S &= \frac{\partial v}{\partial x} + \frac{\partial u}{\partial y}, \\ \xi &= \frac{\partial v}{\partial x} - \frac{\partial v}{\partial y}, \end{aligned} \tag{5.3}$$

where D is horizontal divergence, N is normal deformation, S is shear deformation, and ξ is vorticity. In a coastal environment we expect the D to be somewhat small, while N plus S processes conspire to produce elongated filamented structures like those seen in satellite images of sea surface temperature (SST) or color. Lastly, ξ processes are most often associated with eddies, curving fronts or jets.

It is important to note the physics involved with the velocity gradients. The components of the gradients reflect changes in the volume, area, and orientation of a blob. It is instructive to illustrate the effect that these differential kinematic

parameters have on example blobs' area and perimeter. The following examples are taken from unpublished notes by Kirwan (2011).

First consider a square blob in a purely divergent flow (S=N=ξ=0). The area of the blob increases exponentially with time, and the perimeter increases exponentially, but at half the rate of the area. The evolution of the blob in this example does not cause a shape change.

Next, consider how an initially square blob evolves in a flow with only N (D=S=ξ=0). The blob becomes an elongated rectangle; i.e. a shape change. The area remains the same, but the perimeter ultimately increases exponentially. However, this perimeter change is not necessarily monotonic. It may be noteworthy that N+S deformation processes which increase perimeter, also increase contact area between an oil spill or harmful algal bloom with the surrounding fluid, making exchange more likely.

There is a tenuous relationship between the D and N+S and their impact on perimeter changes. In converging flows with deformation, the area will obviously decrease exponentially, but the perimeter could increase exponentially if the deformation is stronger than the convergence.

Lastly, consider the effect vorticity has on a square blob. This is merely a rotation of the blob, which has no effect on the area or perimeter.

The Okubo–Weiss (OW) parameter is used often to characterize a flow field. This criterion is defined as,

$$\mathrm{OW} = S^2 + N^2 - \xi^2, \geq 0, \leq 0. \tag{5.4}$$

If OW is negative, the flow dominated by vorticity. This is often referred to as elliptical flow. If positive deformation dominates, the flow is termed hyperbolic. When OW is equal to zero, the flow it is parabolic. The results show the flow field at the Delaware Bay mouth tends to be elliptic with occasional episodes of

hyperbolic flow.

Before continuing into the results section let us list the different effects of the velocity gradient:

1) The divergence only affects the area of the blob with no impact on the shape or orientation.

2) The deformation changes the blob shape, but does not change the orientation or area.

3) The perimeter is only affected by the divergence and the deformation.

4) The final result of deformation is to make the blob 'stringy,' but there can also be a transient effect that will depend on the initial blob shape and position, which may cause the perimeter to decrease temporarily.

5.5.2 Computing Kinematic Quantities from Evolving Fluid Patches

Blobs are initialized as finite numbers of points around a circle connected by line segments. The kinematic quantities are computed using contour integrals along the line segments (see appendix A). Two long lived example blobs will be examined, now known as example 1 and example 2. The selection of the blobs from examples 1 and 2 were made simpler with the use of residence time maps. Figures 5.16 and 5.17 show the starting location of the blobs from examples 1 and 2 (black circles), and the residence time in the background. Residence time is discussed in section 5.4. In order to select some long–lived blobs, it was trivial to place the blob in the region of the domain with the highest values of residence.

5.5.3 Results for Evolving Blobs at the Delaware Bay Mouth

The first example is a blob that is advected through the velocity field for 150 hours or 6.25 days. The blob has a radius 1.5 km and was initialized on 1 Oct.

2007, 0200 GMT. Figure 5.18 shows the time series plot of perimeter and area of the blob, with the y-axis normalized by the initial perimeter and area. The perimeter initially decreases then increases while the area increases then decreases over the time period that the blob is within the radar footprint. It is important to note that this decrease in area can decrease the perimeter. The increase in perimeter only occurs area the initial rapid decrease in area. The size and shape of the blob for some selected times can be seen in figure 5.19. Here, we can see how the blob becomes elongated due to the deformation. After an examination of a toy model, there seems to be an interplay between the initial conditions and the deformation field which governs the behavior of the perimeter.

Figure 5.20 shows time series plots of both methods for D, ξ, N, and S for example 1. It is important to note that the dy and dx distances are the same as the initial radius of the blob. Note that the all values has been normalized by Coriolis. We see that both methods agree extremely well for divergence, vorticity, and deformation. The finite difference method seems to be a bit noisier than the blob method. This is to be expected since only four discrete points calculate the velocity gradients, whereas the blob method is using 500 points. Near the end of the time series, the two methods begin to diverge. This likely is due to the fact the evolved perimeter is sampling a larger spatial footprint, so spatial variability produces changes in the area average estimates from the loop method.

We examine another example of blob initialized at a different location and at a different time. The second example was initialized on 1 Sept. 2008, 0000 GMT, which remained in the domain for 127 hours or 5.29 days. Figure 5.21 shows various times of the blob advecting through the domain. As before we see the blob transitioning into a long thin filament after several days. Figure 5.22 shows the time series plots of the perimeter and area. The perimeter is less smooth than in example 1, but the general structure is the same since the curve decreases then increases.

Excluding the initial increase in area, the curves in example 1 and 2 are very similar.

What is the reason for the increase in the perimeter with a simultaneous decrease of area? This is a direct result of the importance of deformation on the blob shape. The blob decreases in area rapidly corresponding to a smaller perimeter; then the area tends to remain relatively constant, while the perimeter increases quickly. This is when the blob evolves into a long thin filament with an increasing perimeter. For the time periods examined here, deformation processes occur very often and tend to dominate. Elongation is commonly observed in drifter clusters or dye patches. The decrease in area for the two example blobs is associated with the movement of the blobs into regions of convergence from which they never recovery their initial areas.

That the time series plots of D, ξ,N, and S are in figure 5.23, for example 2. Again the loop method and the finite difference method are in good agreement. There is also a much larger amount of variance in the divergence and vorticity curves than in the previous example. The deformation plots seem to be relatively the same. Time series of OW (equation 5.4) do not provide much insight into the dominant kinematics beyond the values already discussed.

Figures 5.24 and 5.25 are the power spectra of the time series of divergence, vorticity, and deformation using the loop integral method for the blob from examples 1 and 2, respectively. The deformation curves for both examples have strong peaks at the semi–diurnal tidal frequencies. The vorticity plot has a strong semi–diurnal peak in example 2 and a weaker peak, which is shifted slightly in example 1. The vorticity curve in example 1 also appears to be noisy relative to the other component of the velocity gradient. The divergence plots for examples 1 and 2 are not similar except for a higher frequency peak that is present in both examples. The divergence seems to be influenced by a higher frequency forcing at approximately twice the semi–diurnal frequencies.

To test this method's ability to capture the frequency of these kinematic features, a test blob was advected with an M2 tidal field. Figure 5.26 shows that this single frequency in the velocity record will appear as a strong peak at the M2 frequency in the power spectra of the kinematic parameters. This test case also produced a weaker peak at twice the semi–diurnal frequencies. This higher frequency peak could be the max flood and ebb tides acting on the blob twice for every tidal period.

The agreement between the two methods is very good for the time periods examined here. The finite difference method is strictly a point estimate at a center of mass, while the loop method is strictly an area average. Since these two methods are very similar, the flow lacks spatial variability of the kinematic parameters.

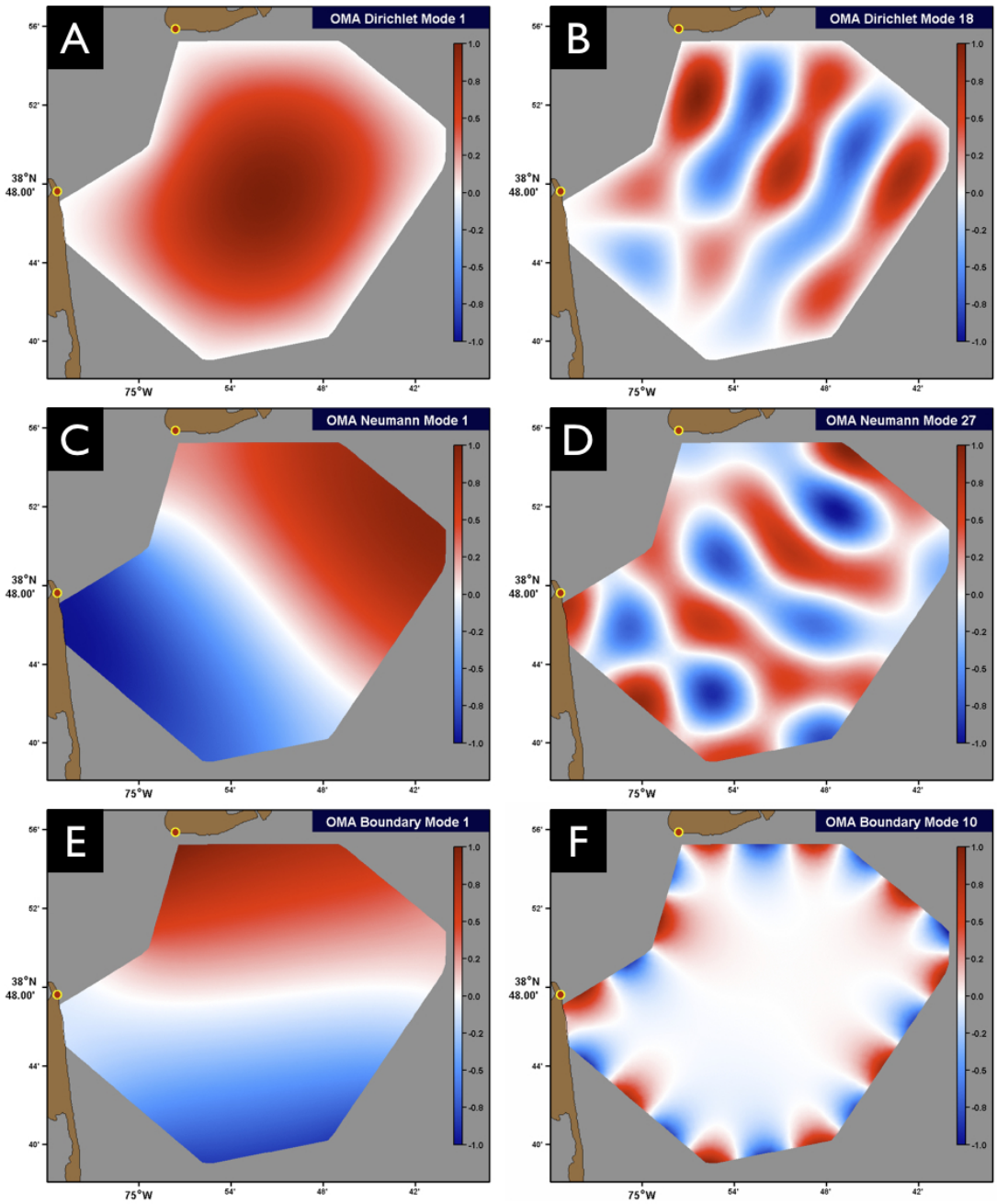

Figure 5.1: Delaware Bay OMA mode representations: (A) Dirichlet mode 1, (B) Dirichlet mode 18, (C) Neumann mode 1, (D) Neumann mode 27, (E) Boundary mode 1, and (F) Boundary mode 10.

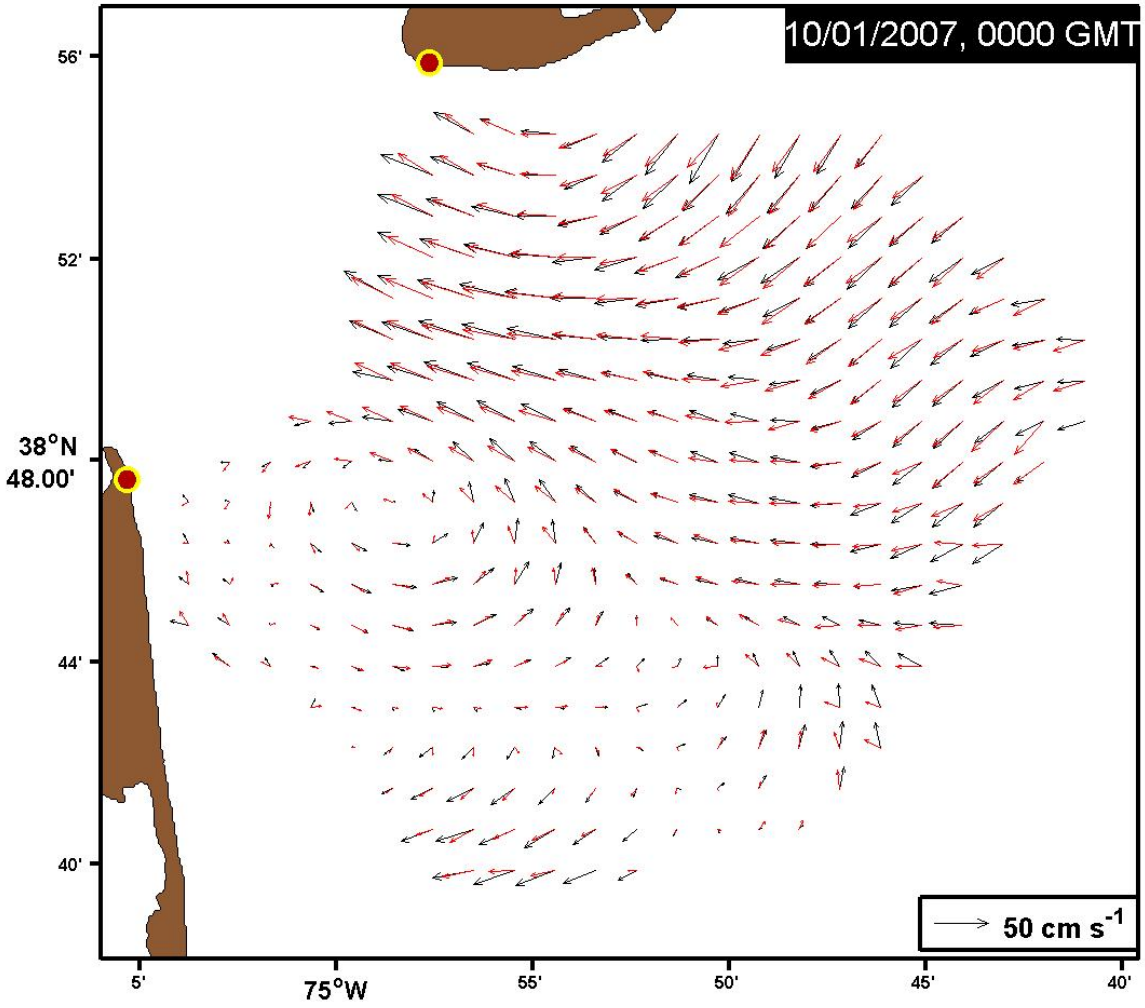

Figure 5.2: Delaware Bay OMA (black vectors) vs. HF radar (red vectors) comparison for Oct. 1, 2007, 0000 GMT.

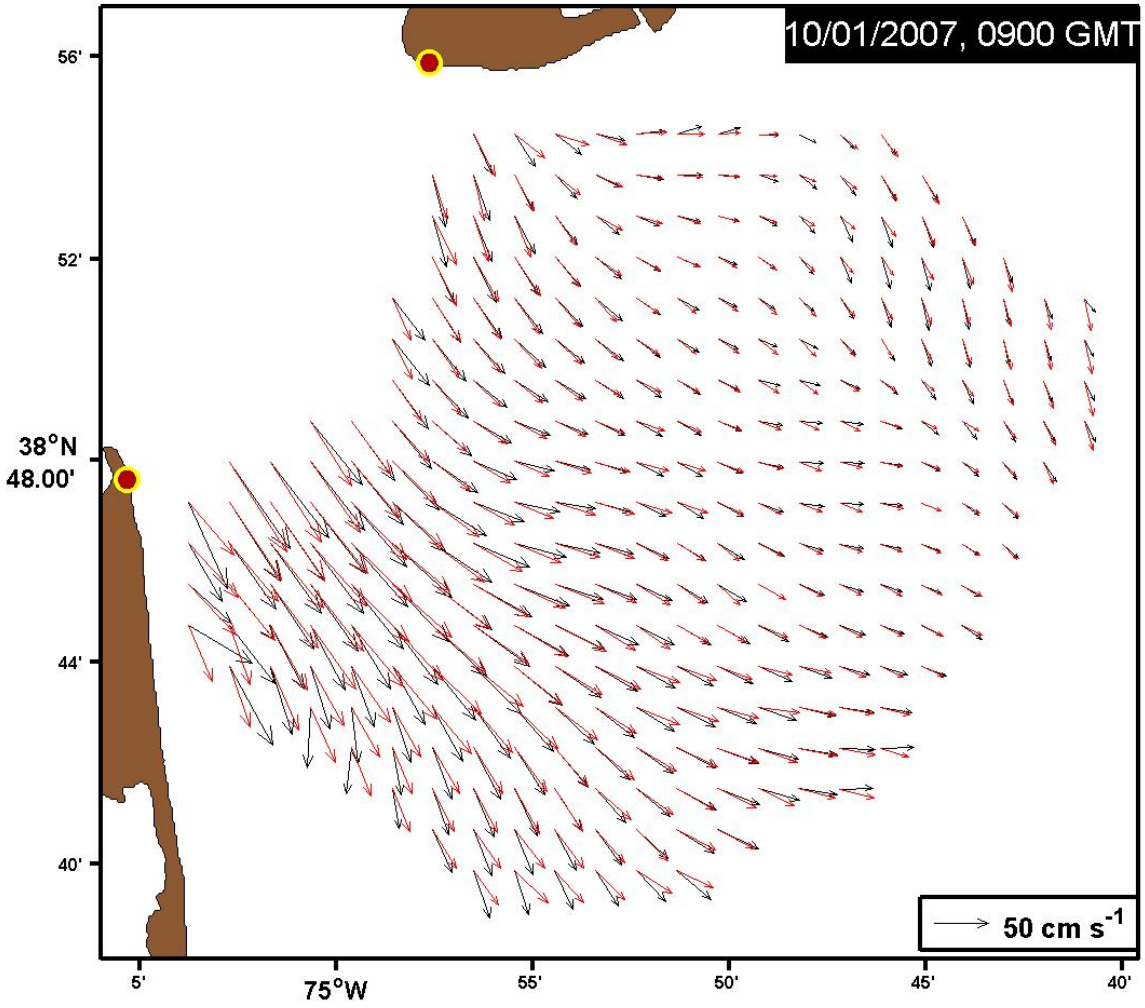

Figure 5.3: Delaware Bay OMA (black vectors) vs. HF radar (red vectors) comparison for Oct. 1, 2007, 0900 GMT.

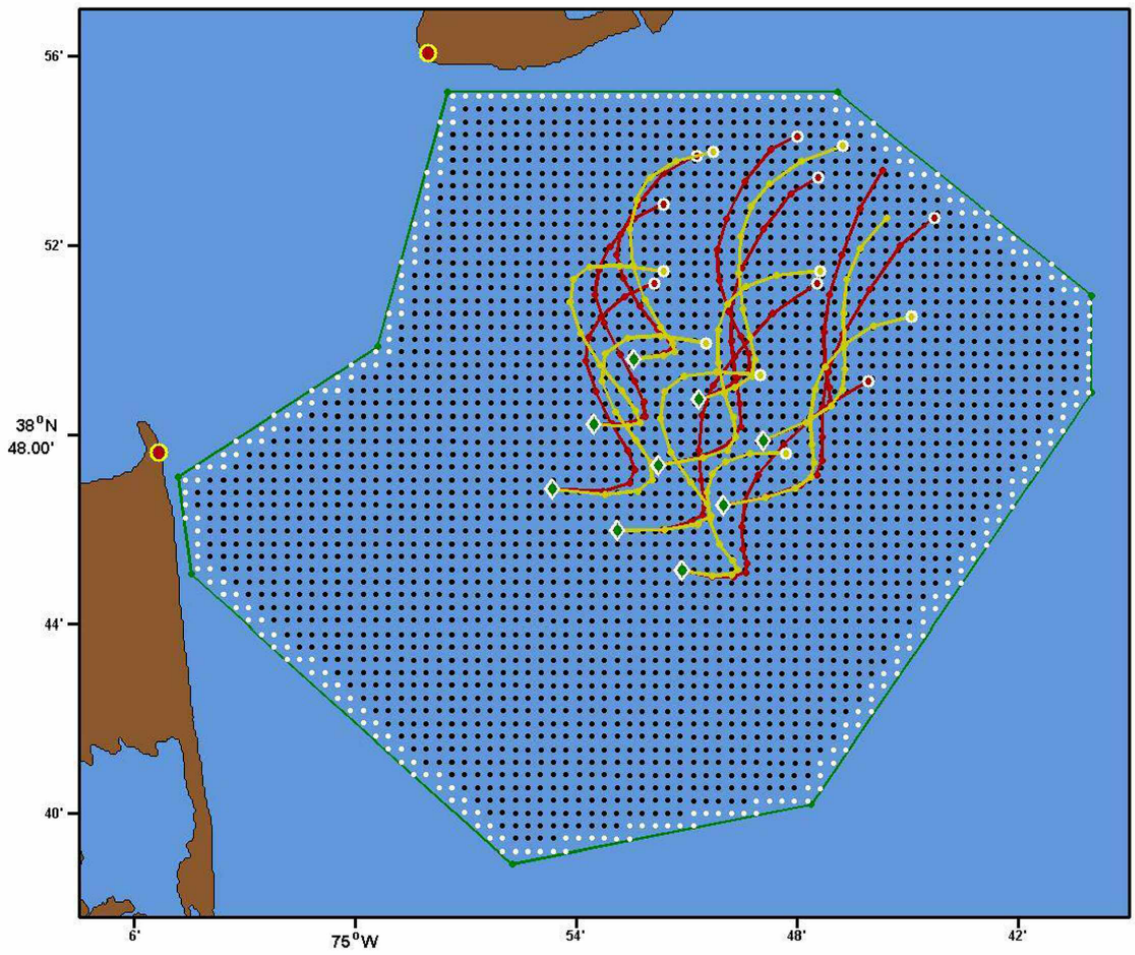

Figure 5.4: Map of the Delaware Bay mouth showing the objective mapping domain (green), mapping grid points (black and white circles), and locations of the two radar sites (red circles with yellow outlines). The nine particle launch positions for this study are shown as green diamonds with white outline. Example 12-hour trajectories (red) and PVD trajectories (yellow) for particles launched at 12 April 2008, 1200 GMT are also shown. (Copyright (2011) by the American Society of Limnology and Oceanography, Inc.)

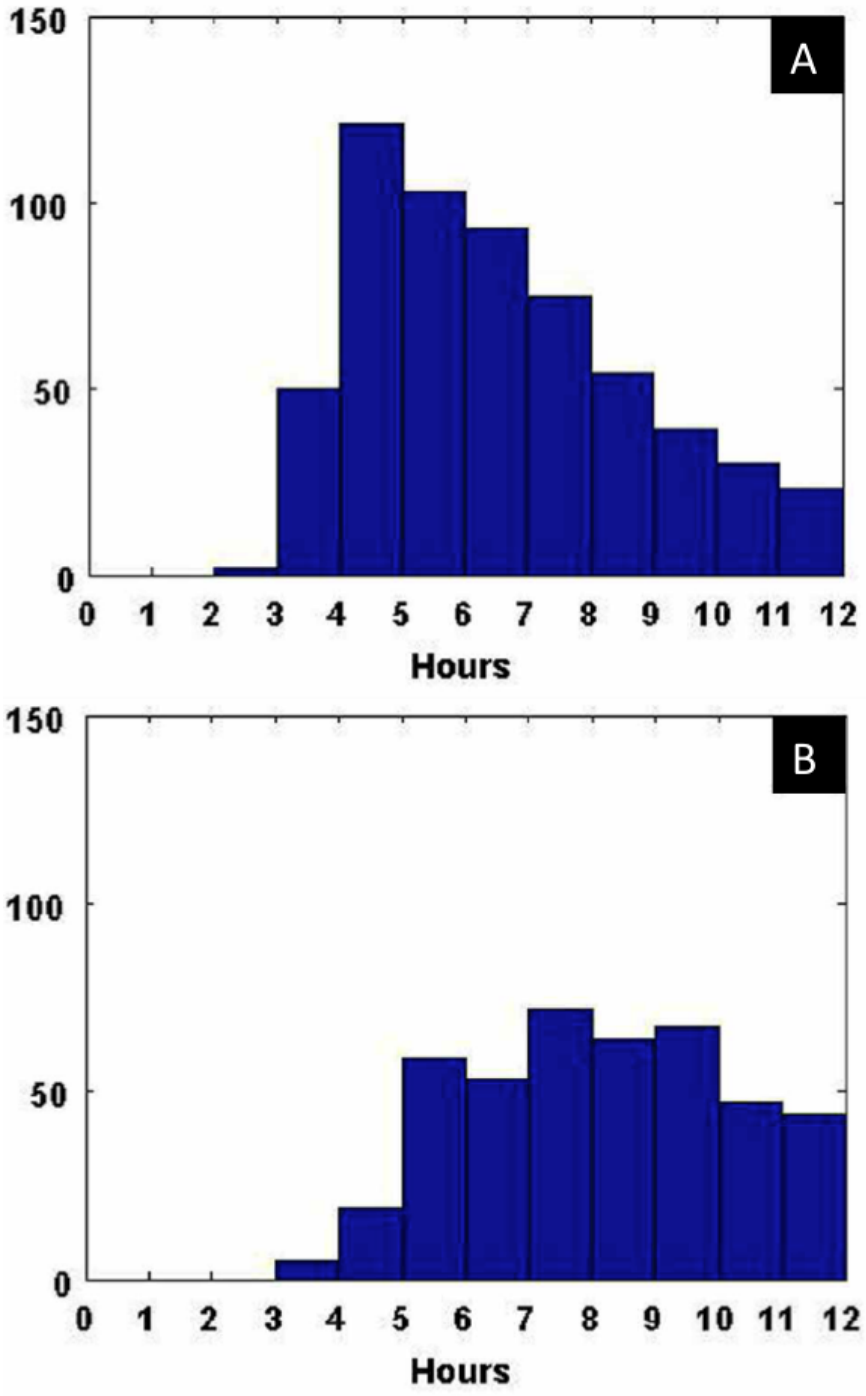

Figure 5.5: Histograms of 500-m and 1000-m separation times (hours) for September 2008 at the Delaware Bay mouth (A and B).

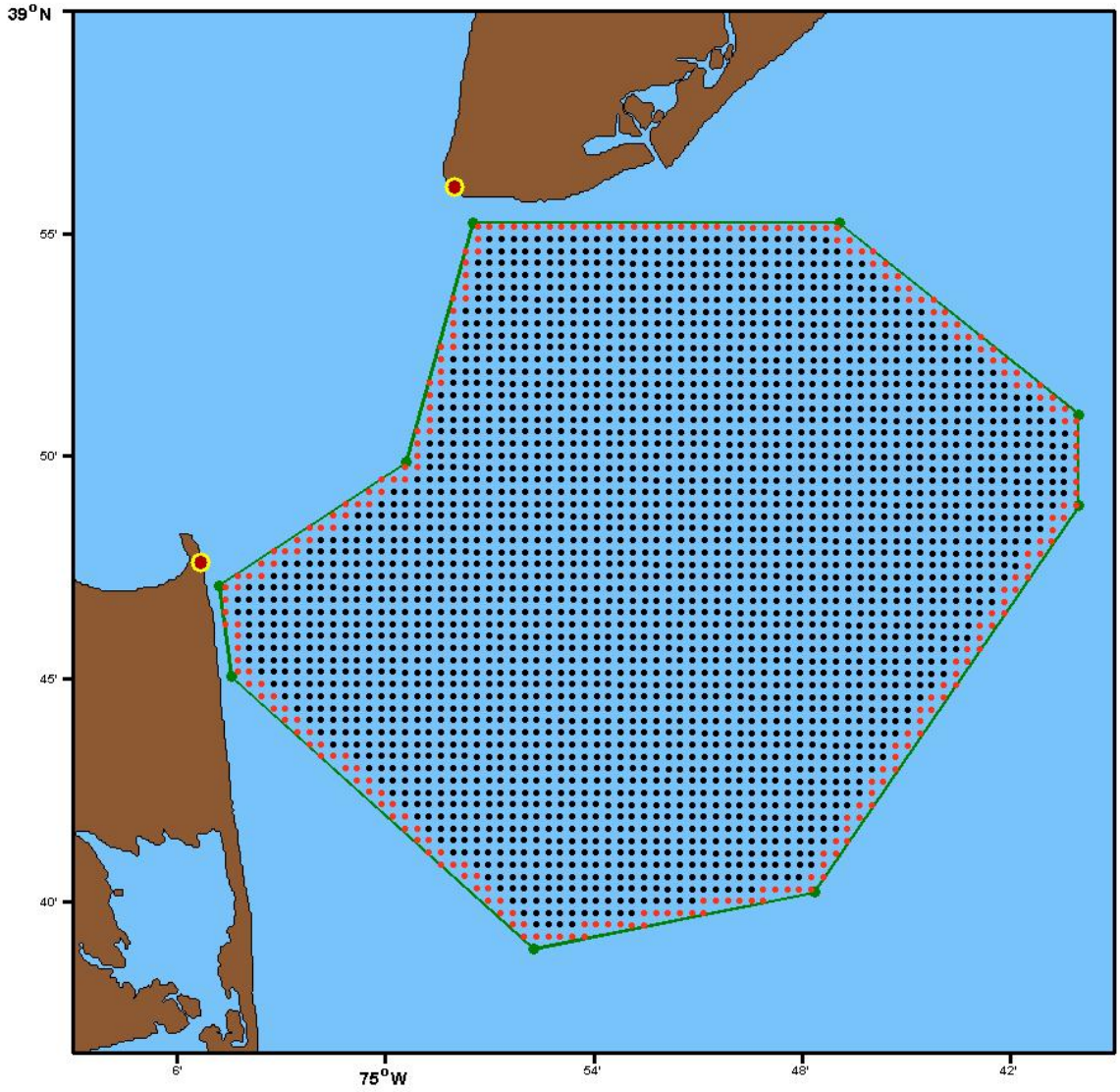

Figure 5.6: Grid showing initial particle positions (in black) for residence time and particle origin/fate calculations. Grid points in red show locations, where particles are considered to exit the domain.

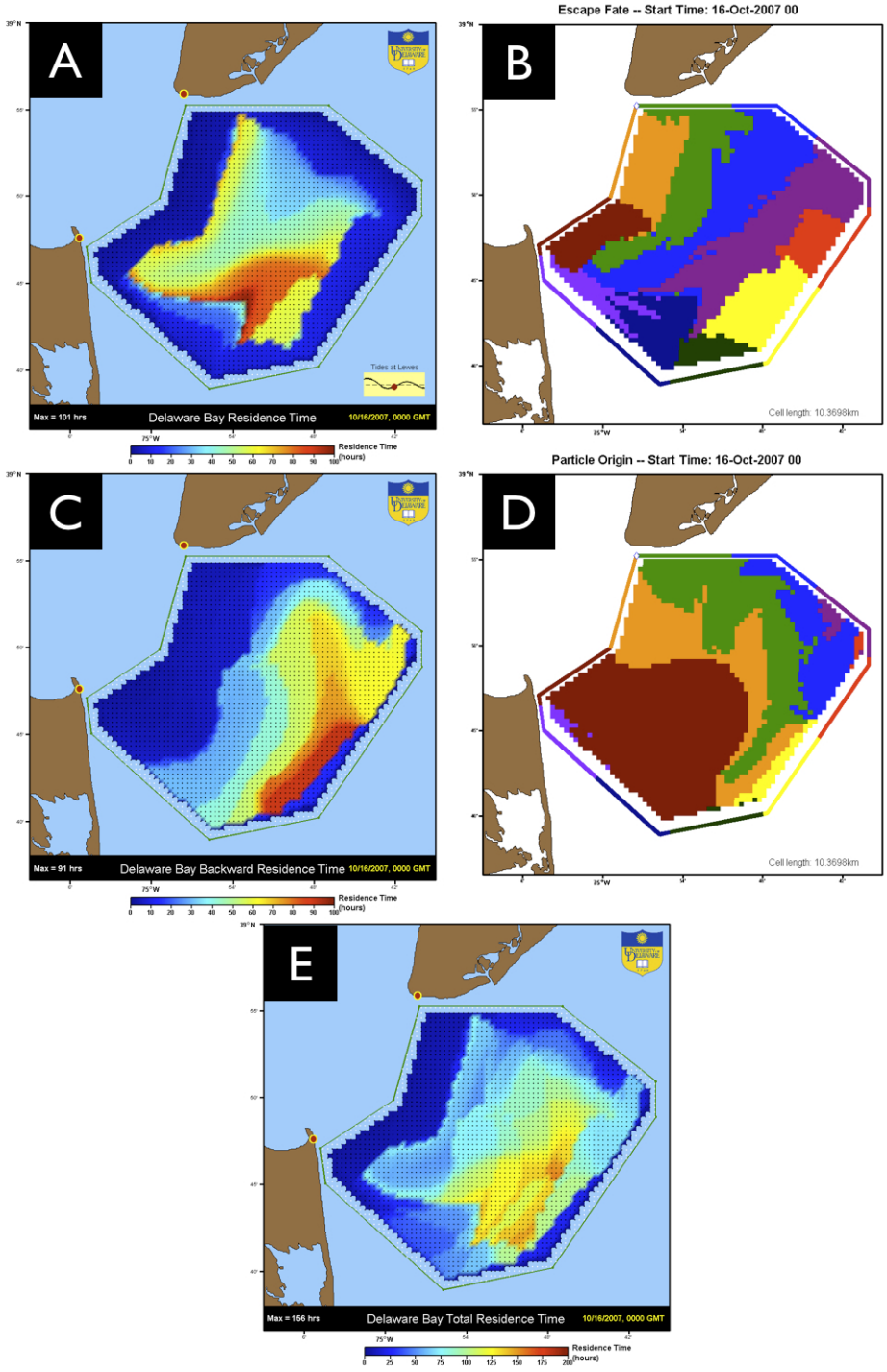

Figure 5.7: (A) Forward residence time with inset plot of tidal height at Lewes, DE; (B) Escape fate; (C) backward residence time; (D) particle origin; and (E) total residence time (i.e. the sum of the forward and backward residence) for particles released on Oct. 16, 2007, 0000 GMT. This example is at a time when tidal currents are at a maximum.

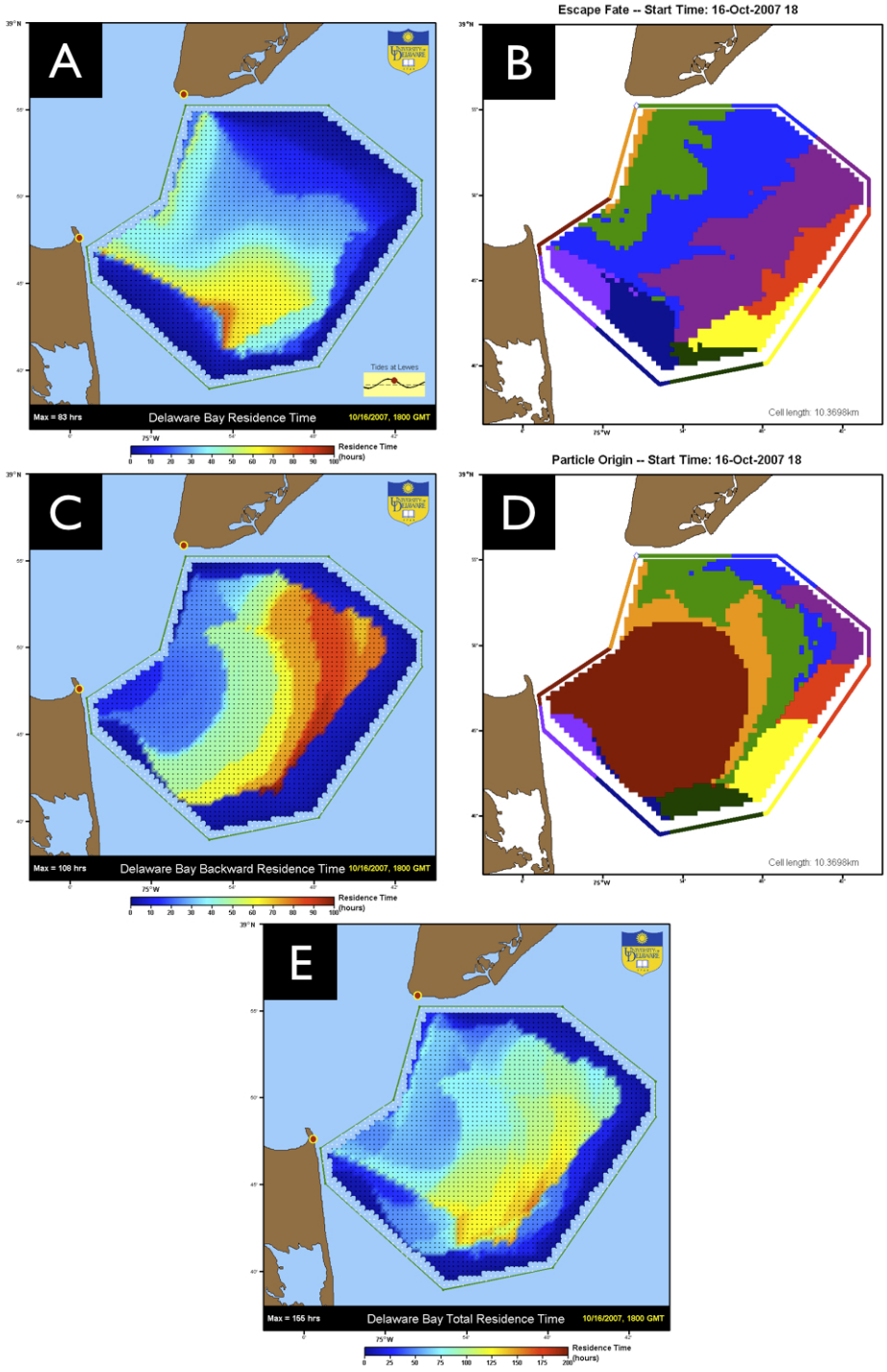

Figure 5.8: (A) Forward residence time with inset plot of tidal height at Lewes, DE; (B) Escape fate; (C) backward residence time; (D) particle origin; and (E) total residence time (i.e. the sum of the forward and backward residence) for particles released on Oct. 16, 2007, 1800 GMT. This example is at a time when tidal currents ebbing.

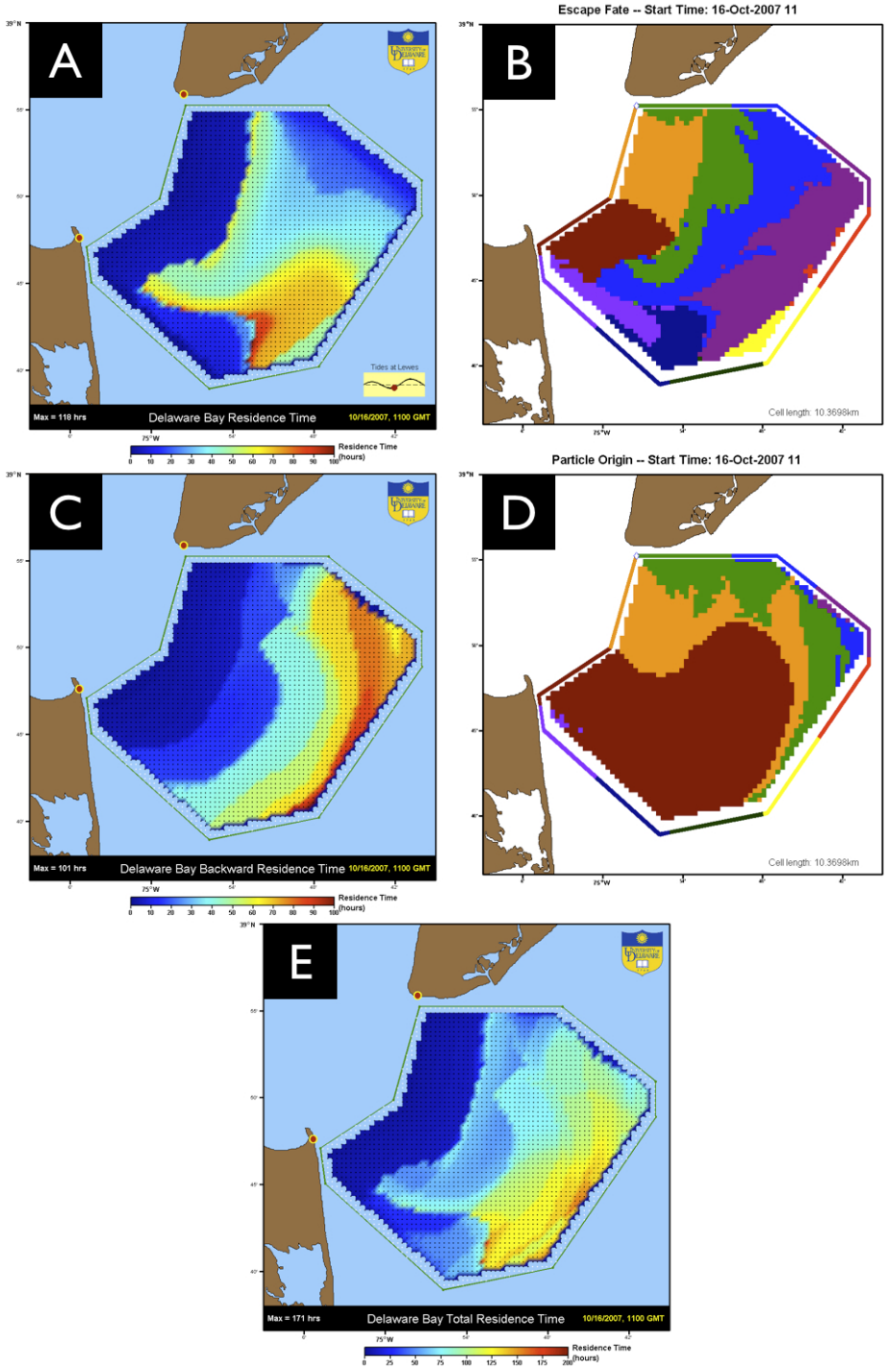

Figure 5.9: (A) Forward residence time with inset plot of tidal height at Lewes, DE; (B) Escape fate; (C) backward residence time; (D) particle origin; and (E) total residence time (i.e. the sum of the forward and backward residence) for particles released on Oct. 16, 2007, 1100 GMT. This example is at a time when tidal currents flooding.

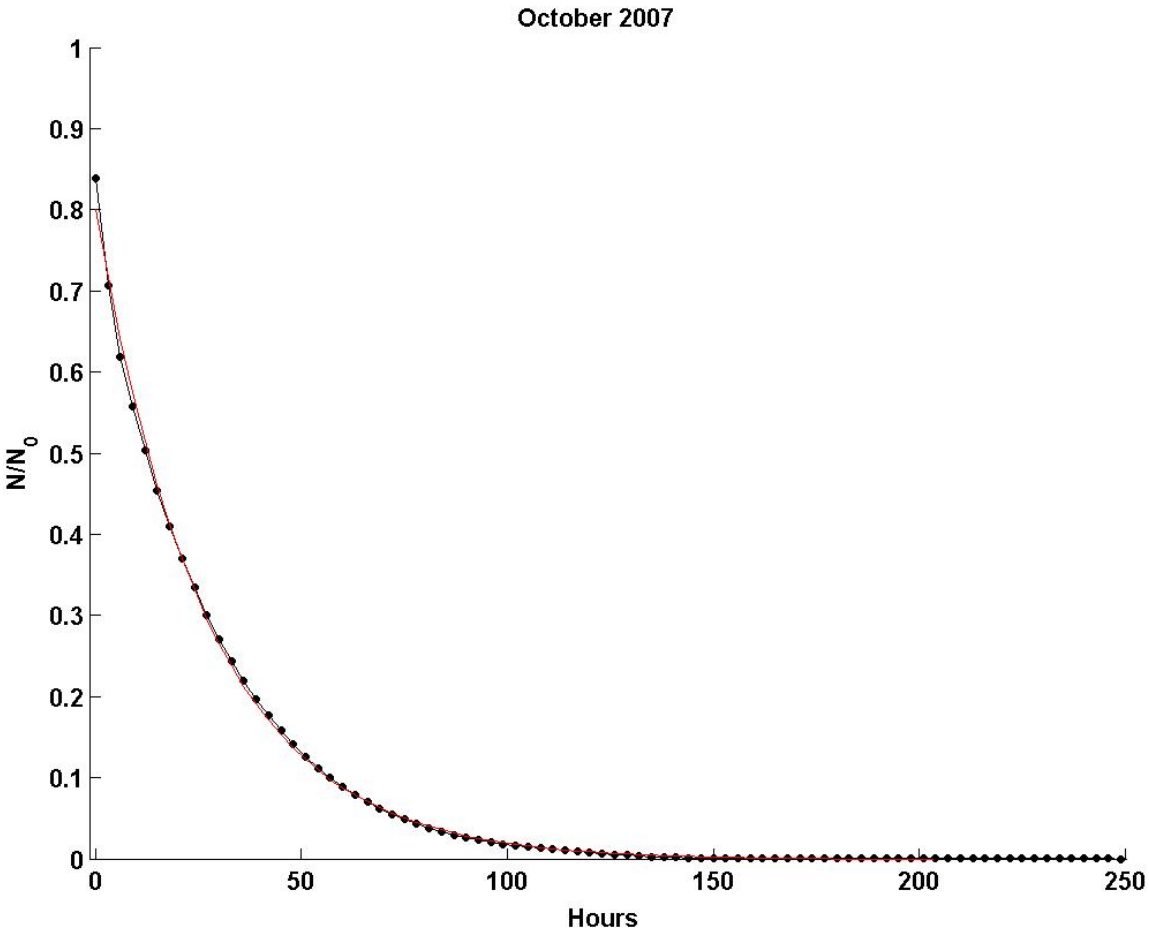

Figure 5.10: Population size of particles that remain in the domain normalized my the initial number of particles. Black curve is the data in three hour bins while the red curve is the exponential fit to the data.

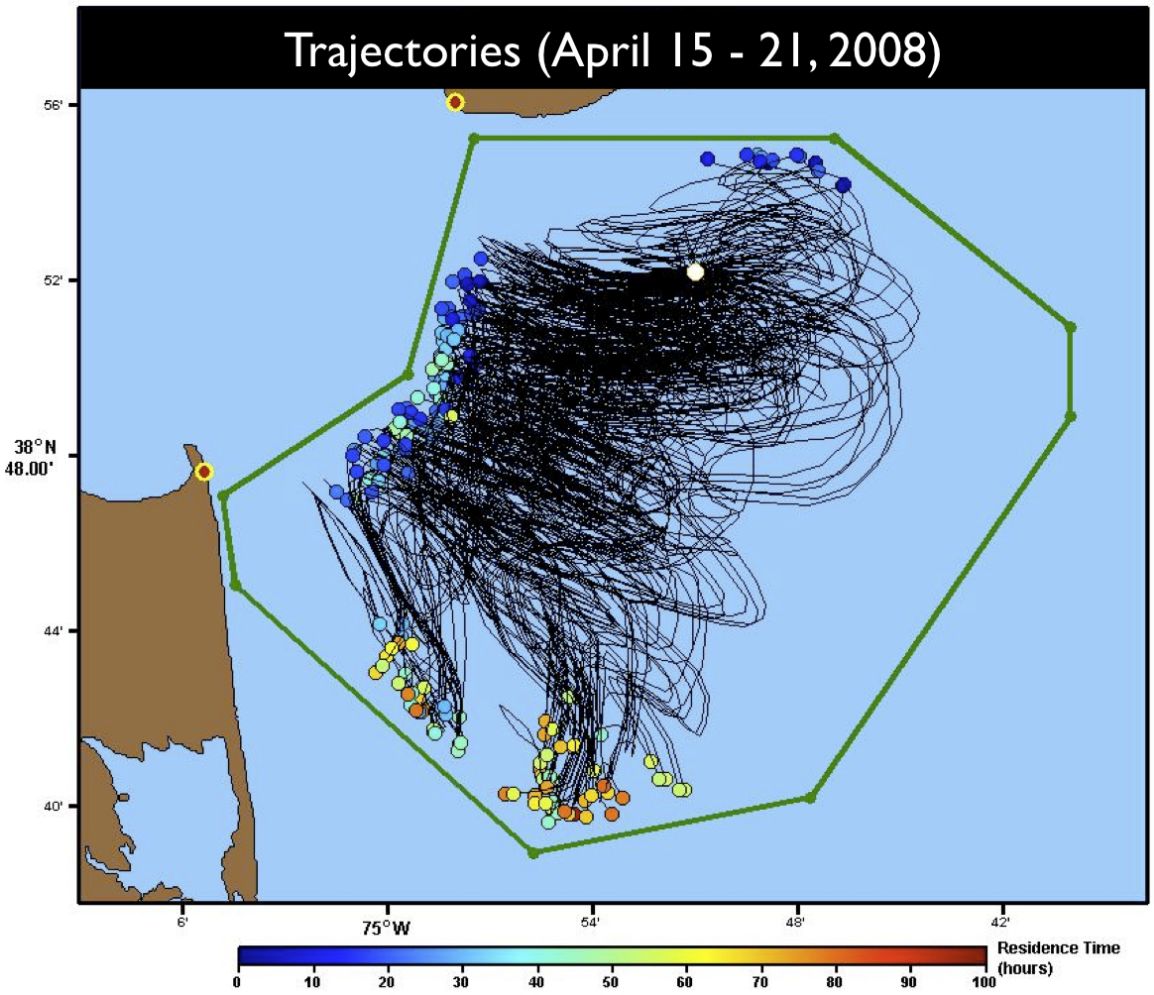

Figure 5.11: Residence time trajectories (in black) from a single location (white dot) with the residence time (color coded dots at end of trajectory) and escape locations for April 15 through April 22, 2008.

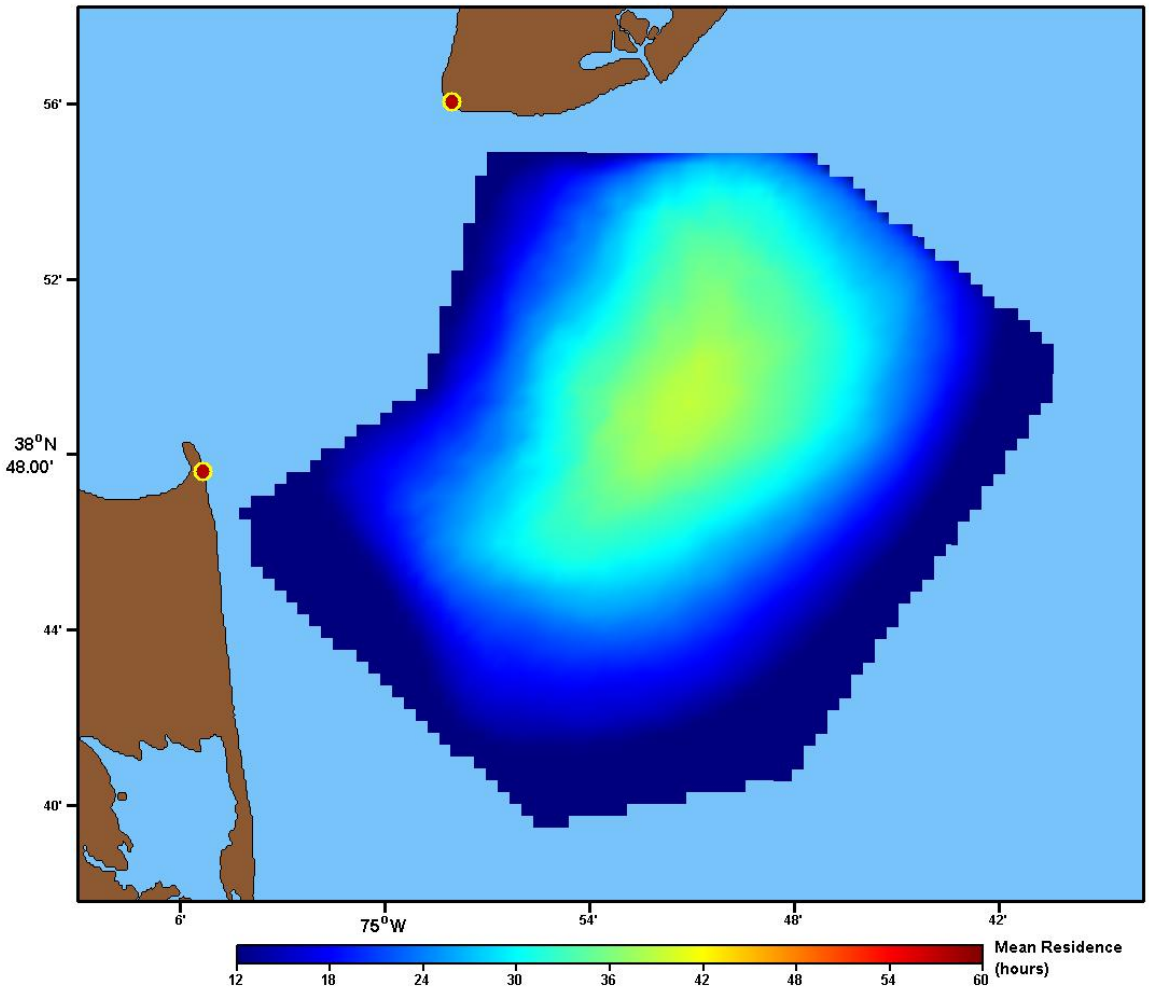

Figure 5.12: Mean residence time for March 2008 computed from hourly residence time maps.

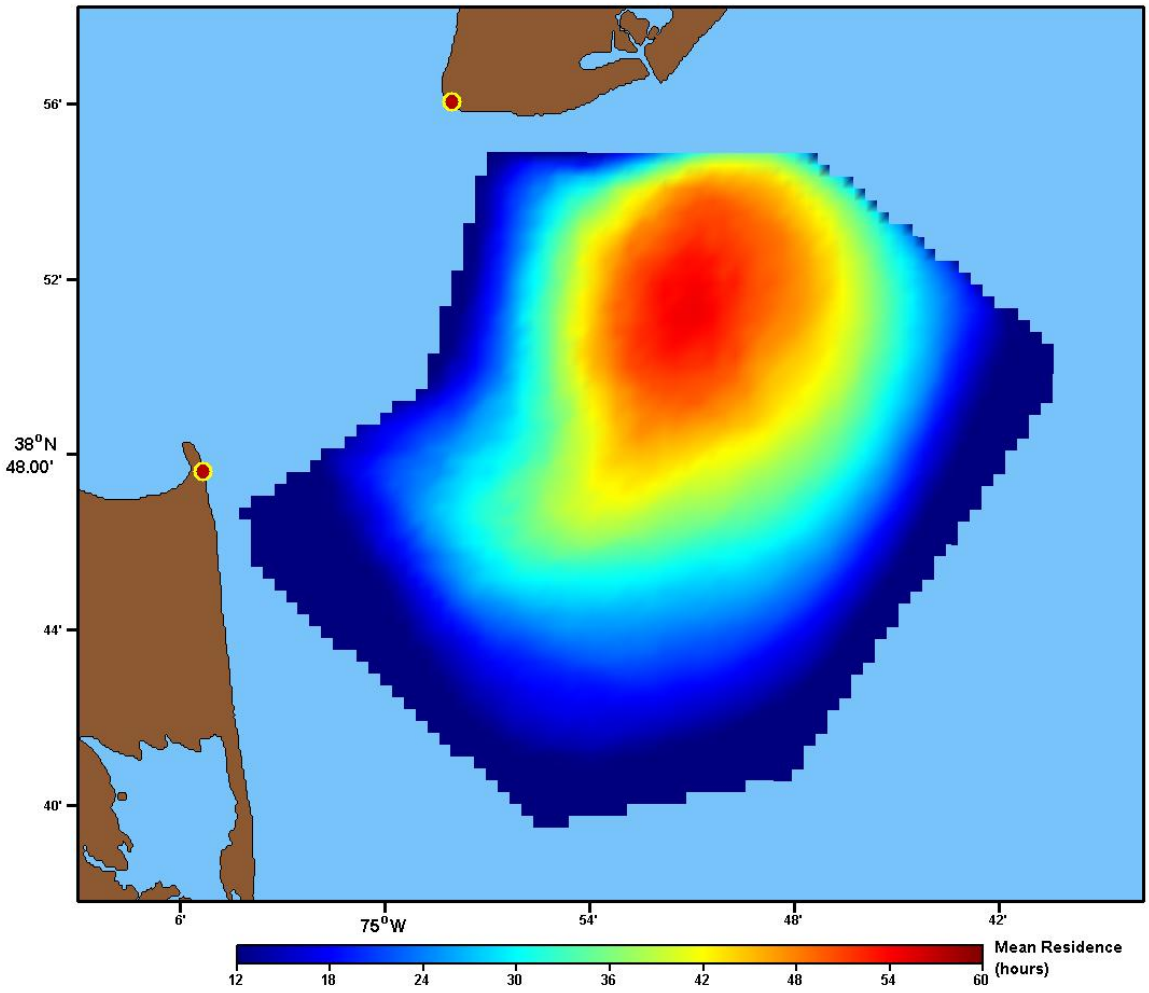

Figure 5.13: Mean residence time for April 2008 computed from hourly residence time maps.

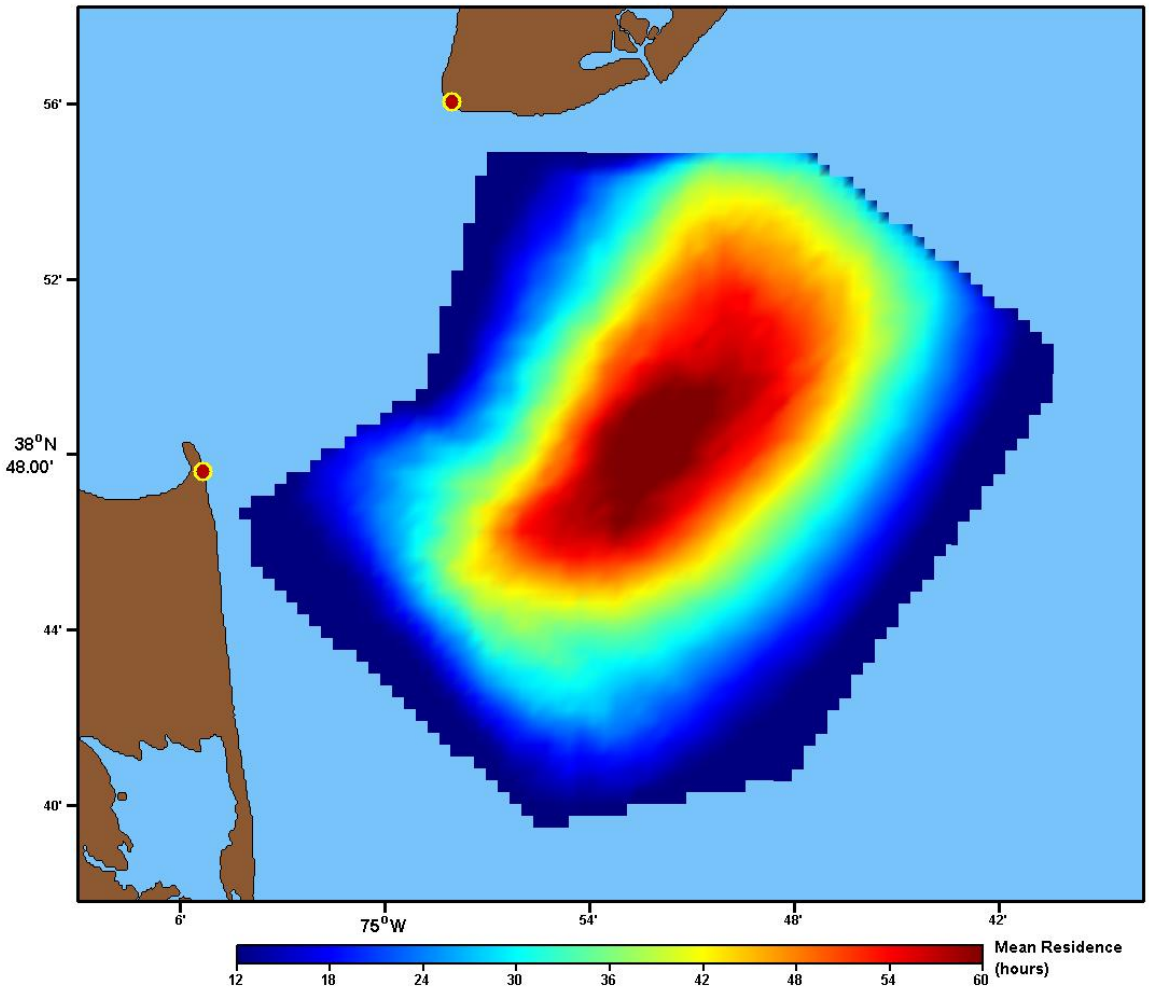

Figure 5.14: Mean residence time for September 2008 computed from hourly residence time maps.

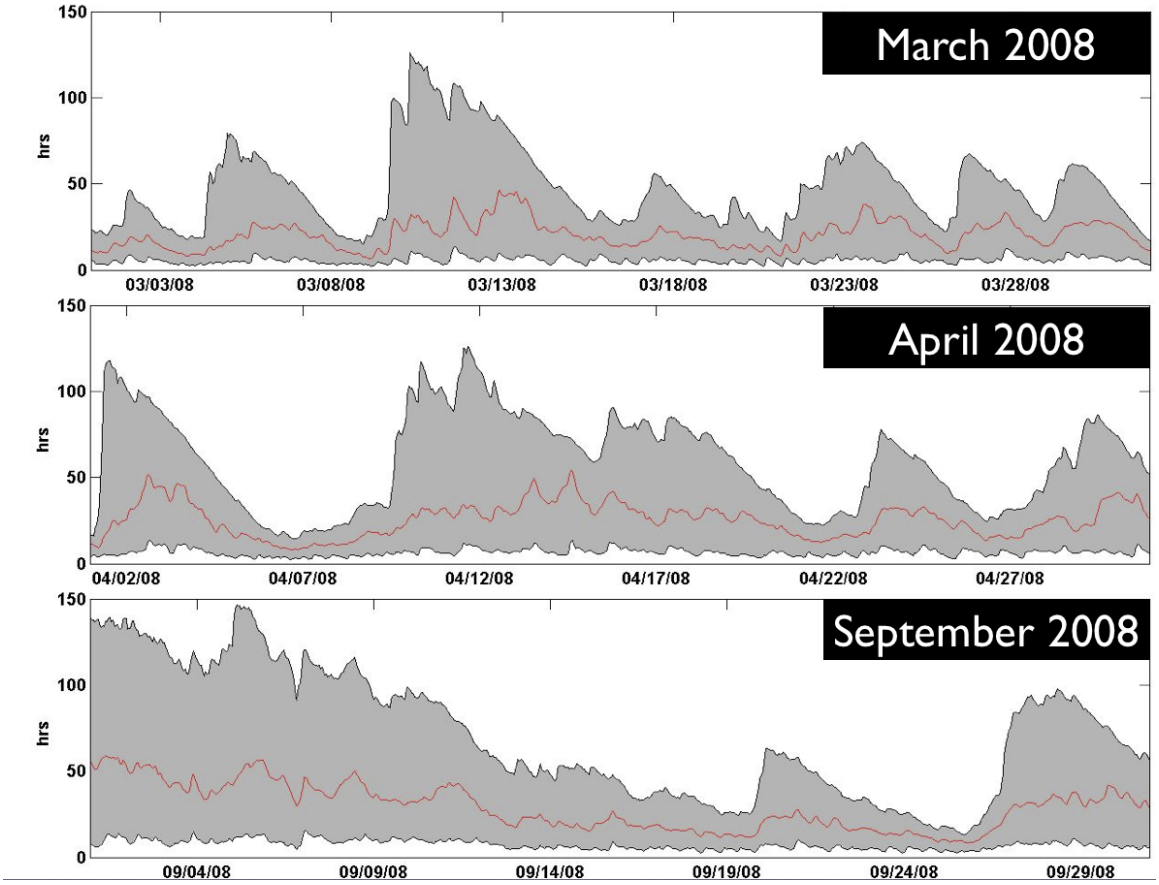

Figure 5.15: Spatial mean residence time March 2008, April 2008 and September 2008.

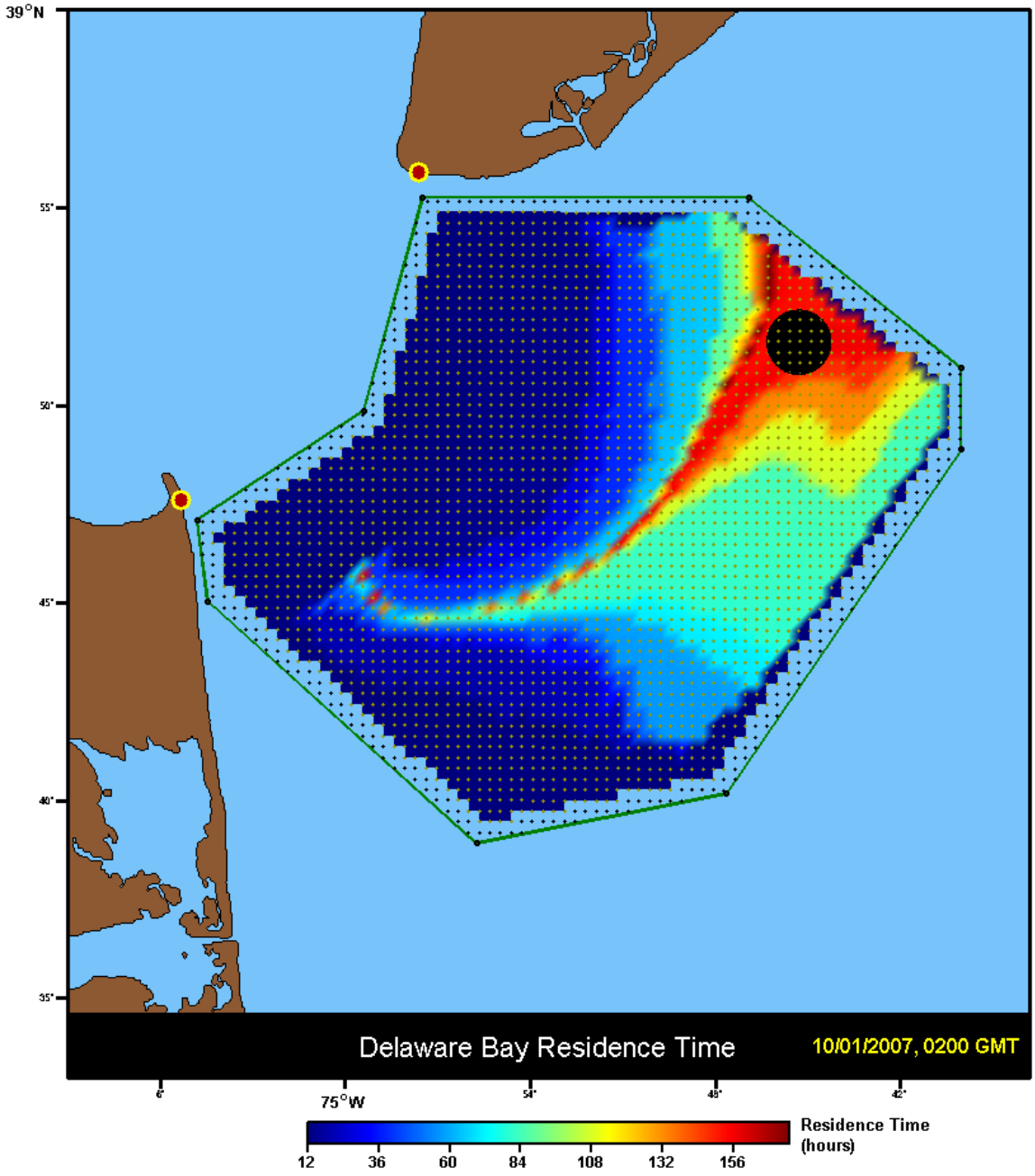

Figure 5.16: Black circle is a blob of radius 1.5 km that is initialized on 1 Oct. 2007, 0200 GMT which remained in the domain for 150 hours. The center of the blob is located at longitude -74.753 degrees and latitude 38.862 degrees. The color contour plot is the residence time.

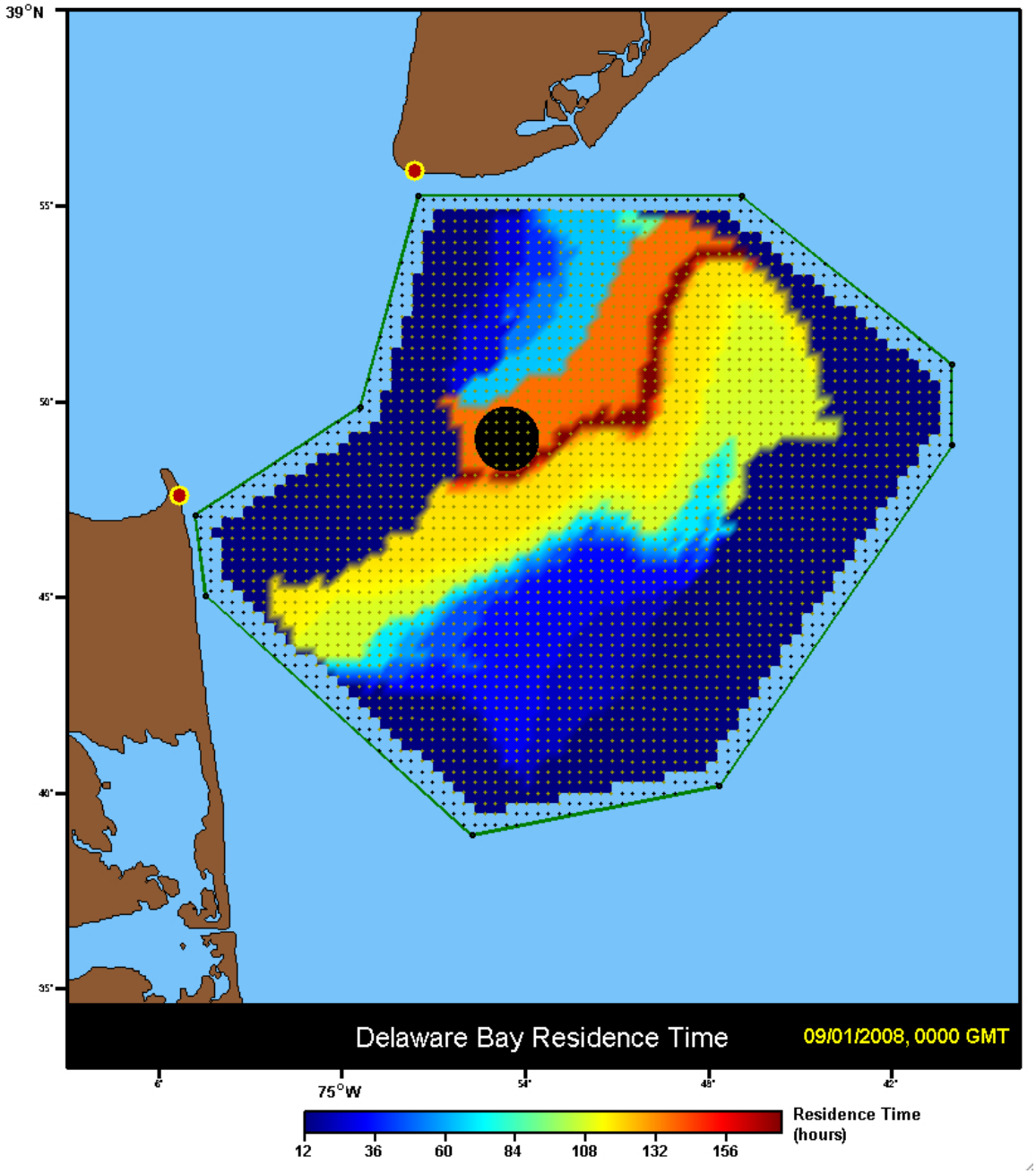

Figure 5.17: Black circle is a blob of radius 1.5 km that is initialized on 1 Sept. 2008, 0000 GMT which remained in the domain for 127 hours. The center of the blob is located at longitude -74.91 degrees and latitude 38.8175 degrees. The color contour plot is the residence time.

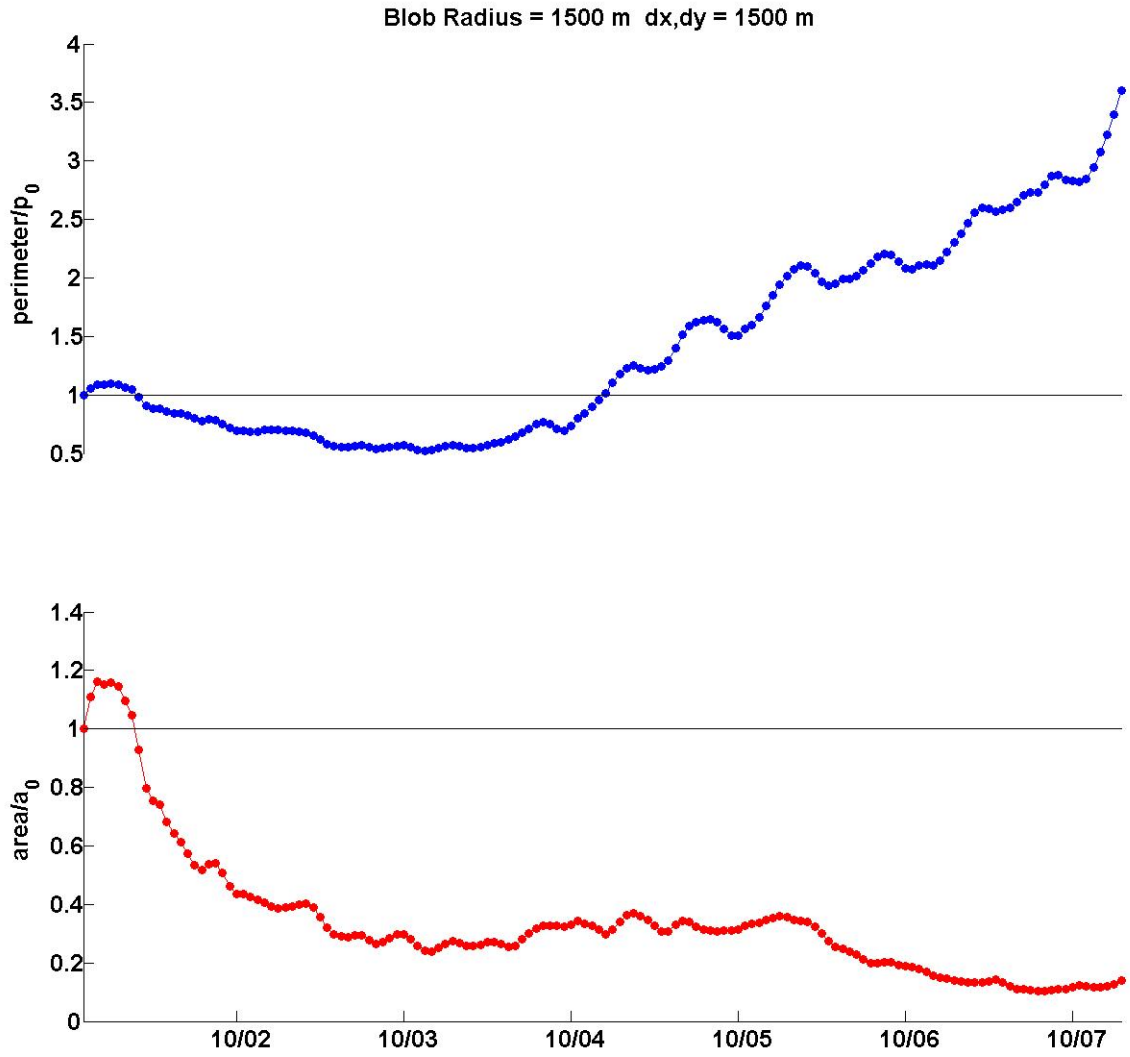

Figure 5.18: Time Series plots of perimeter and area for a blob initialized on 1 Oct. 2007, 0200 GMT which remained in the domain for 150 hours.

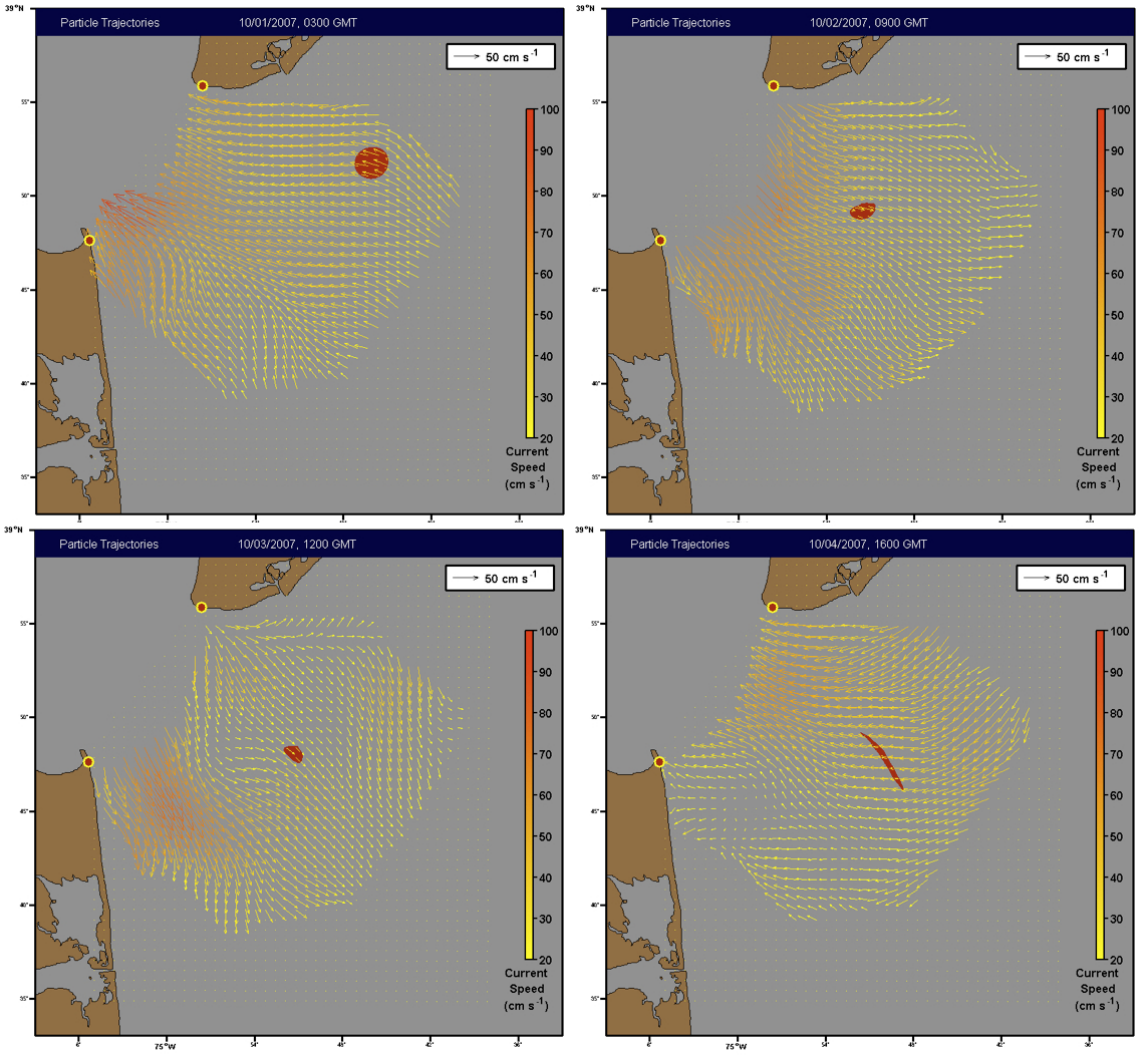

Figure 5.19: Frames of an animation where a blob is initialized on 1 Oct. 2007, 0200 GMT which remained in the domain for 150 hours.

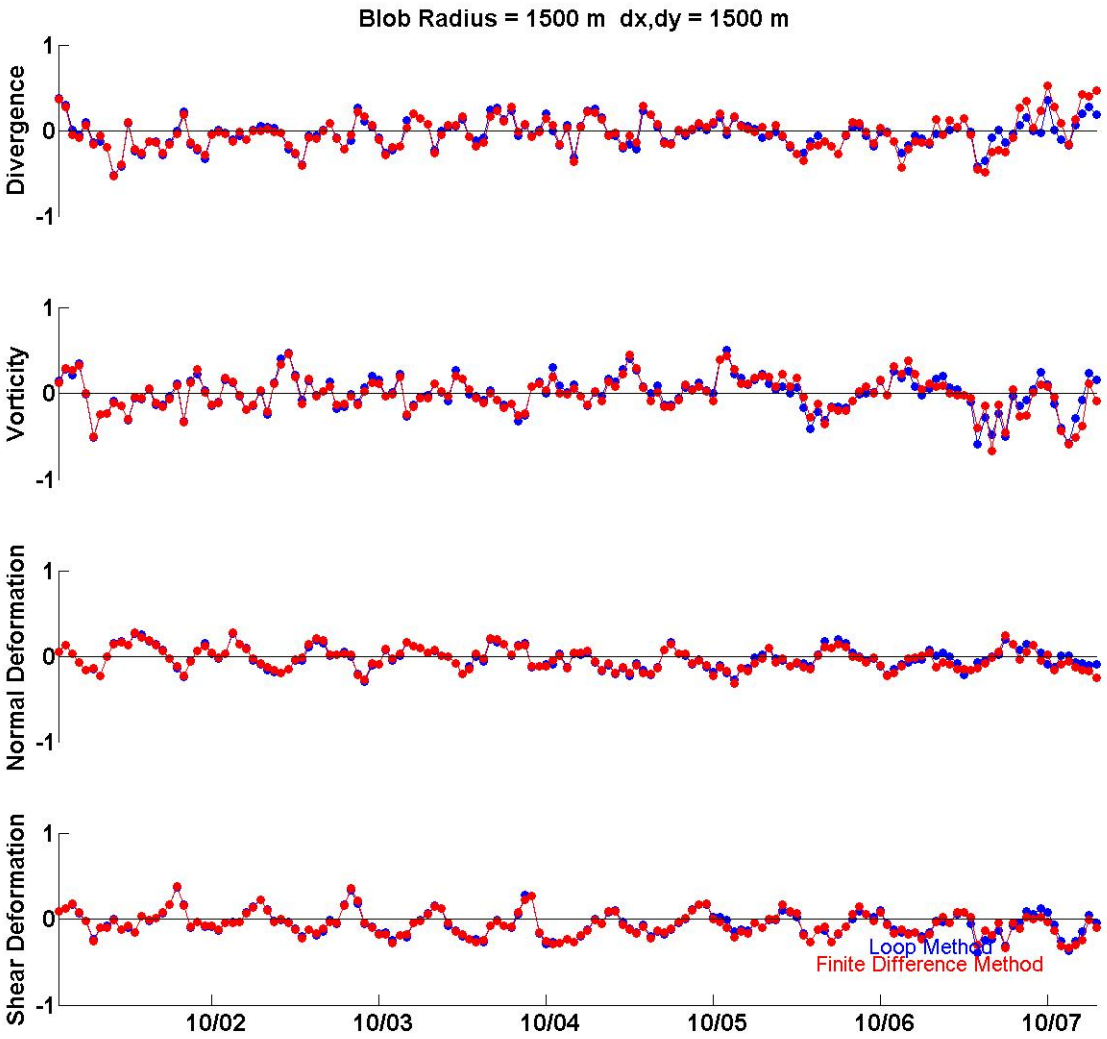

Figure 5.20: Time series of D, ξ,N, and S for a blob initialized on 1 Oct. 2007, 0200 GMT, which remained in the domain for 150 hours. The blue curves use the loop method and the red curves use the finite difference method. All values have been normalized by the local Coriolis.

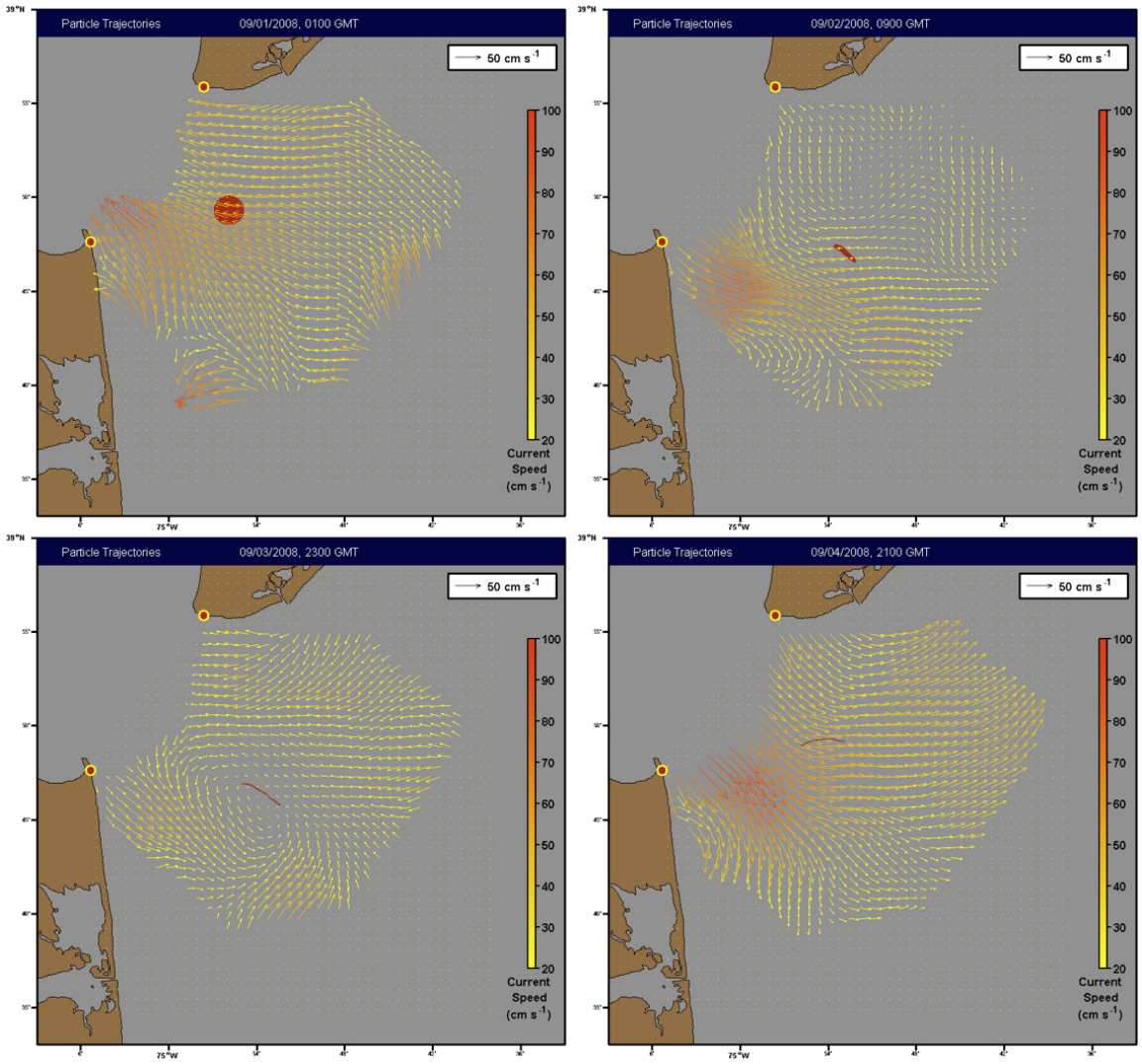

Figure 5.21: Evolution of a blob launched on 1 Sept. 2008, 0000 GMT. This blob remained in the domain for 127 hours.

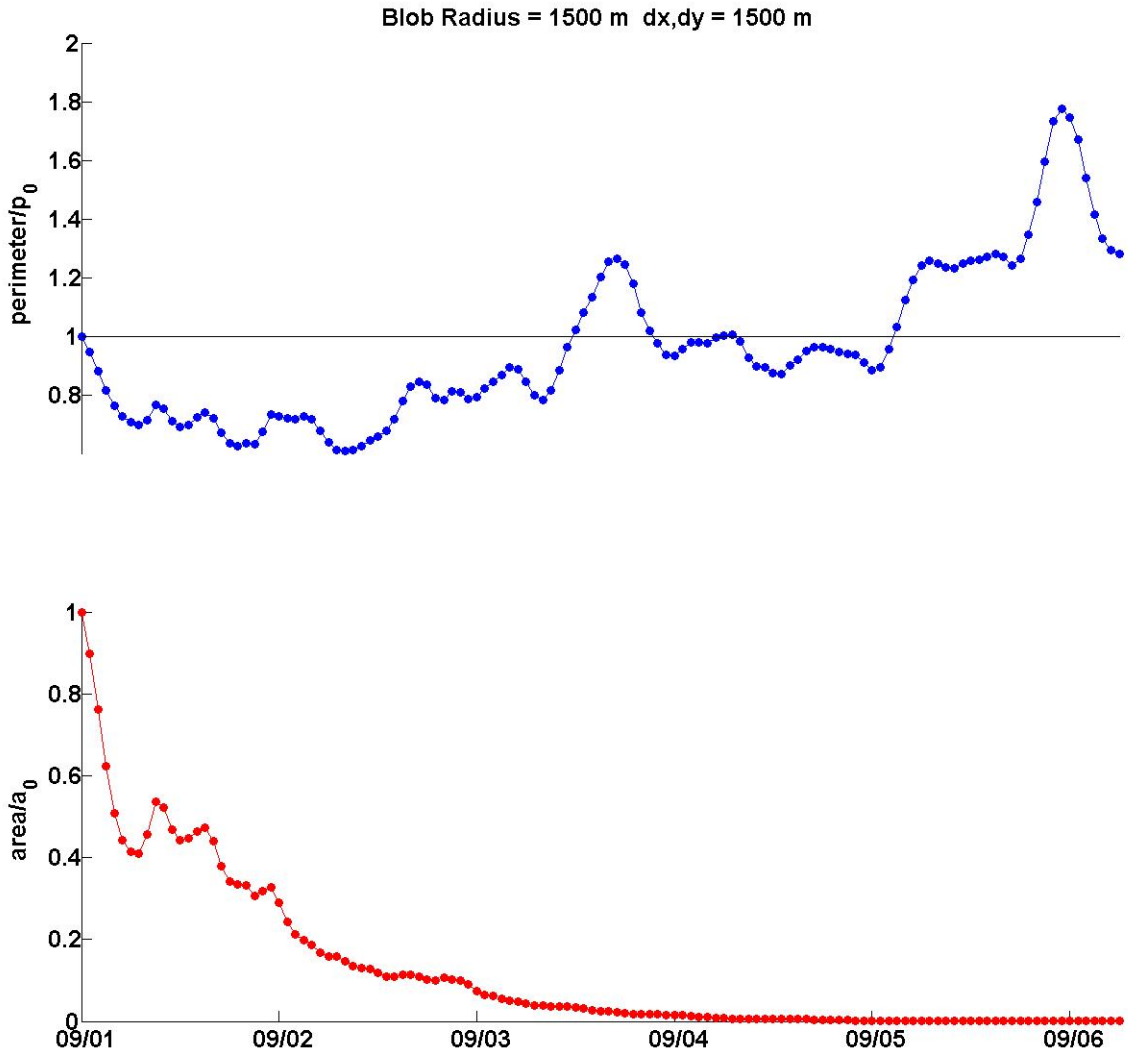

Figure 5.22: Time Series plots of perimeter and area for a blob initialized on 1 Sept. 2008, 0000 GMT, which remained in the domain for 127 hours.

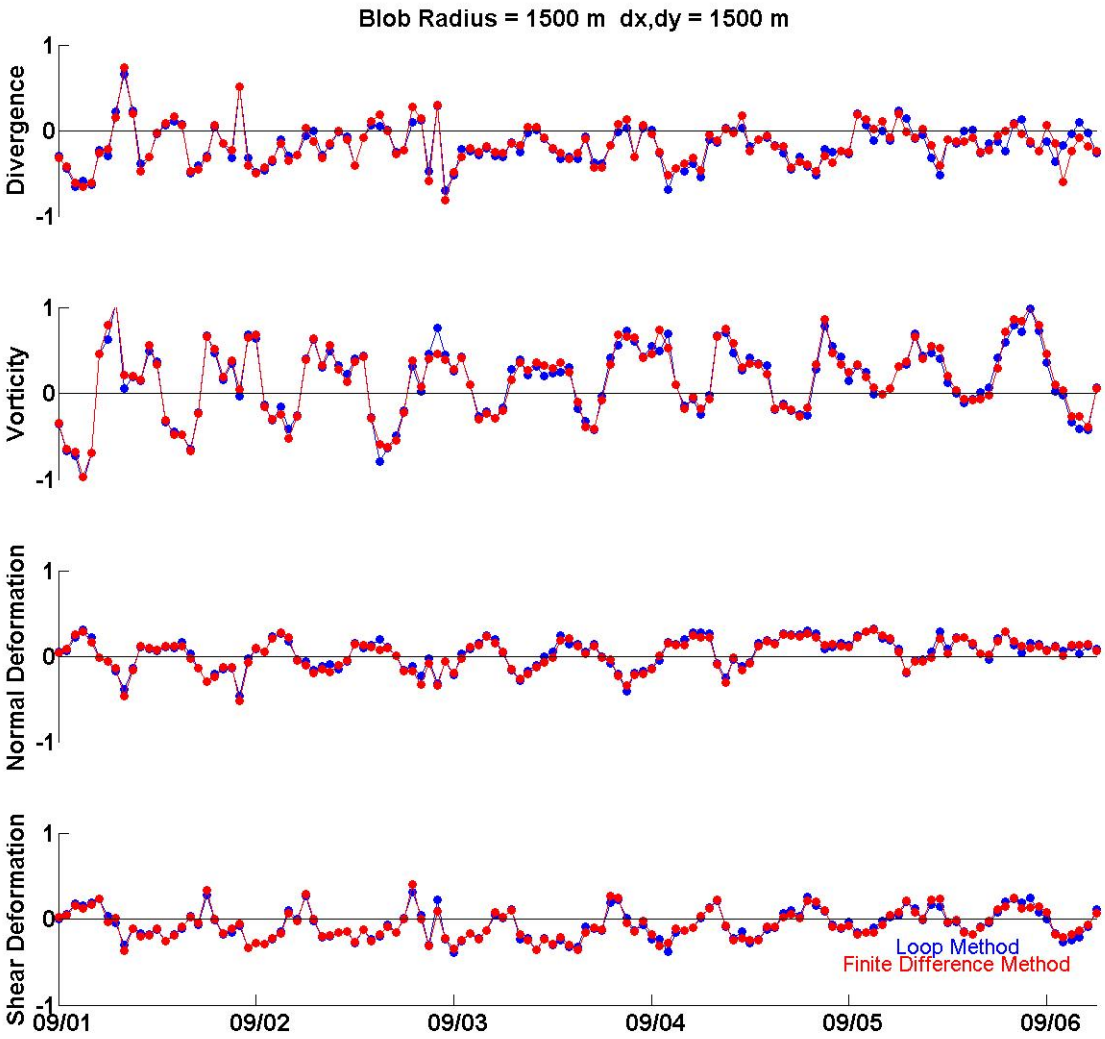

Figure 5.23: Time series of D, ξ,N, and S for a blob initialized on 1 Sept. 2008, 0000 GMT, which remained in the domain for 127 hours. The blue curves use the loop method and the red curves use the finite difference method. All values has been normalized by the local Coriolis.

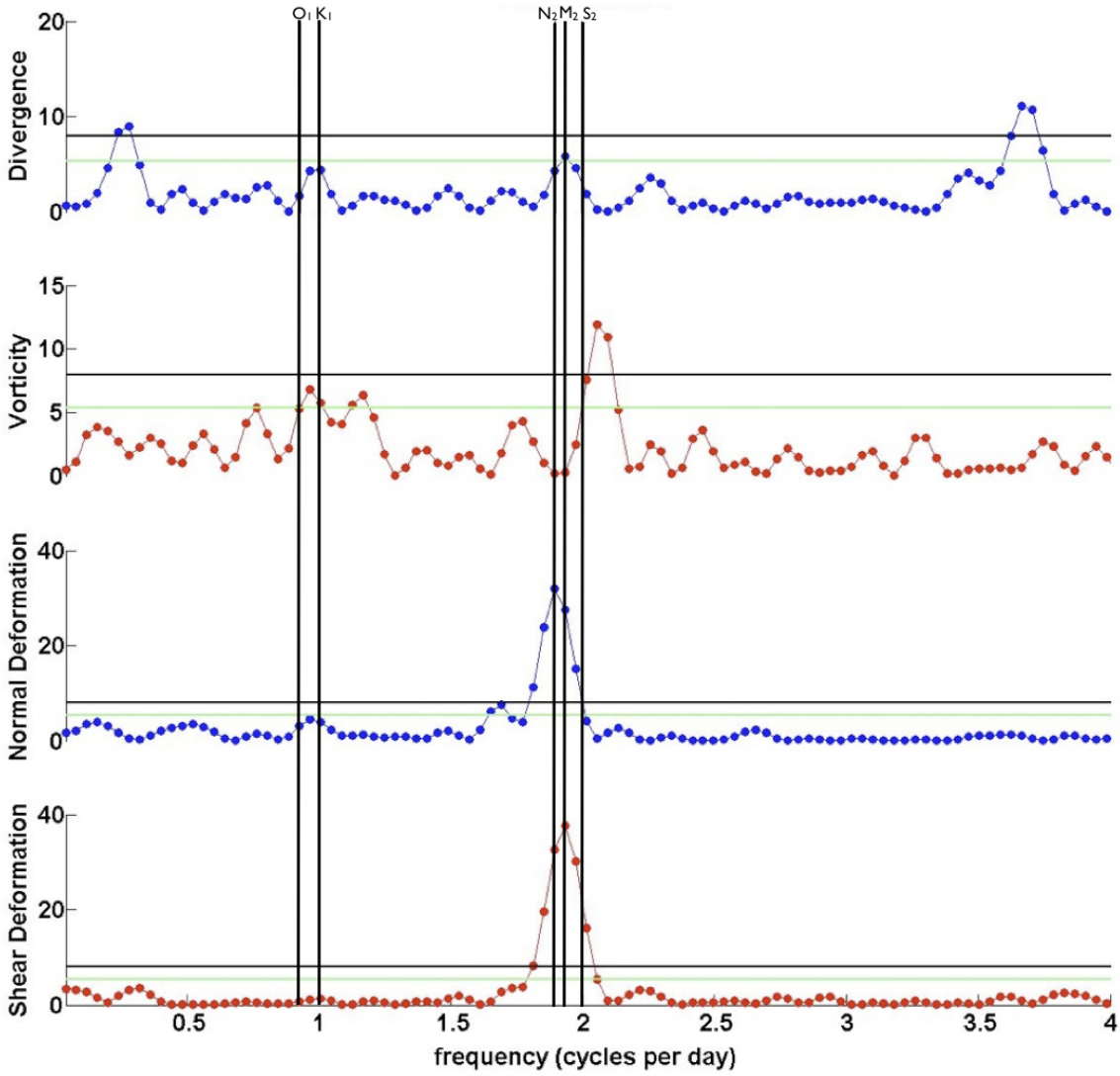

Figure 5.24: Power spectra plots of divergence, vorticity, normal deformation, and shear deformation for a blob initialized on 1 Oct. 2007, 0200 GMT, which remained in the domain for 150 hours. The black and green horizontal lines are the 95% and 50% confidence respectively. The black vertical lines are placed at the frequencies of the dominant tidal constituents.

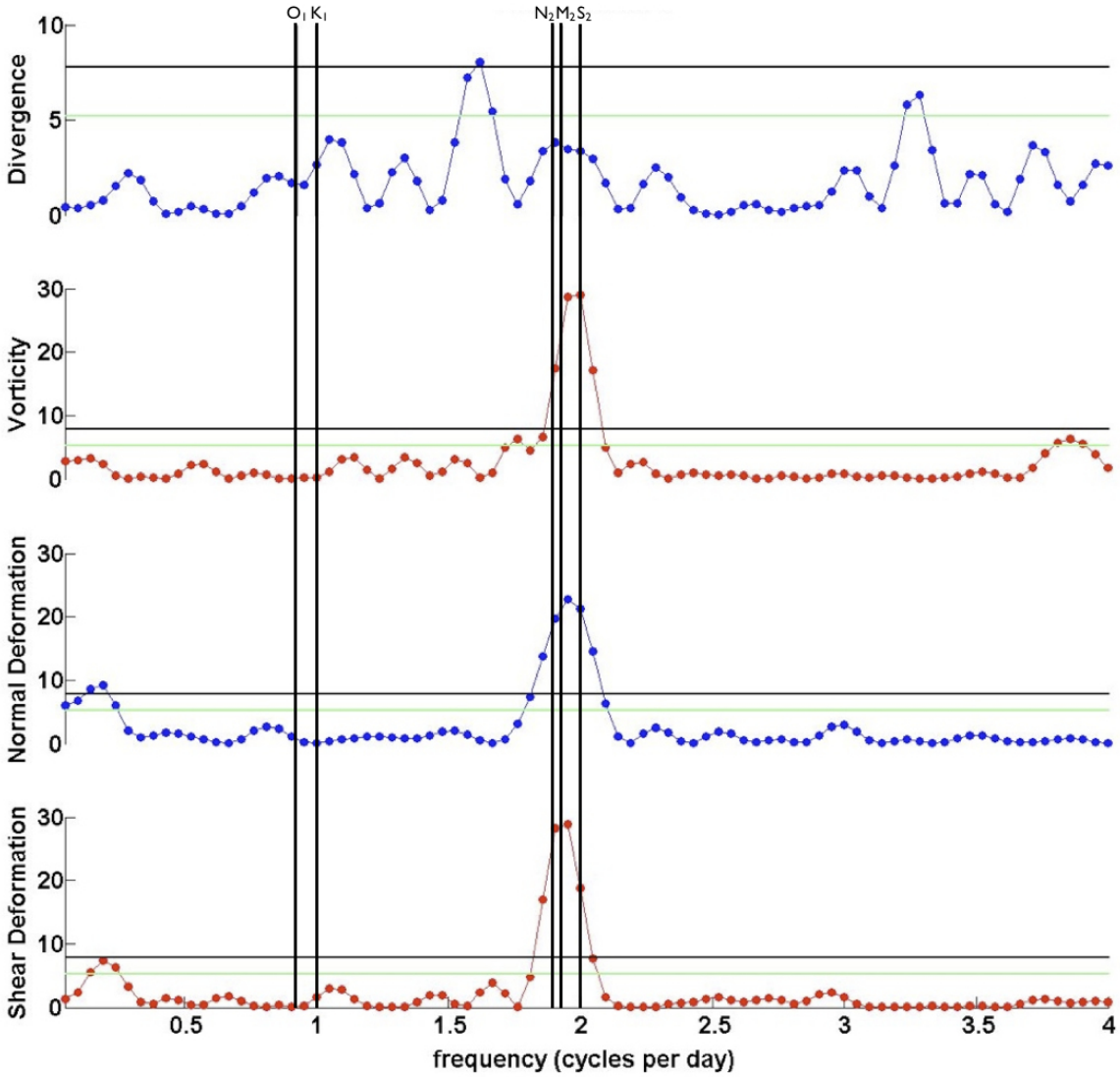

Figure 5.25: Power spectra plots of divergence, vorticity, normal deformation, and shear deformation for a blob initialized on 1 Sept. 2008, 0000 GMT, which remained in the domain for 127 hours. The black and green horizontal lines are the 95% and 50% confidence respectively. The black vertical lines are placed at the frequencies of the dominant tidal constituents.

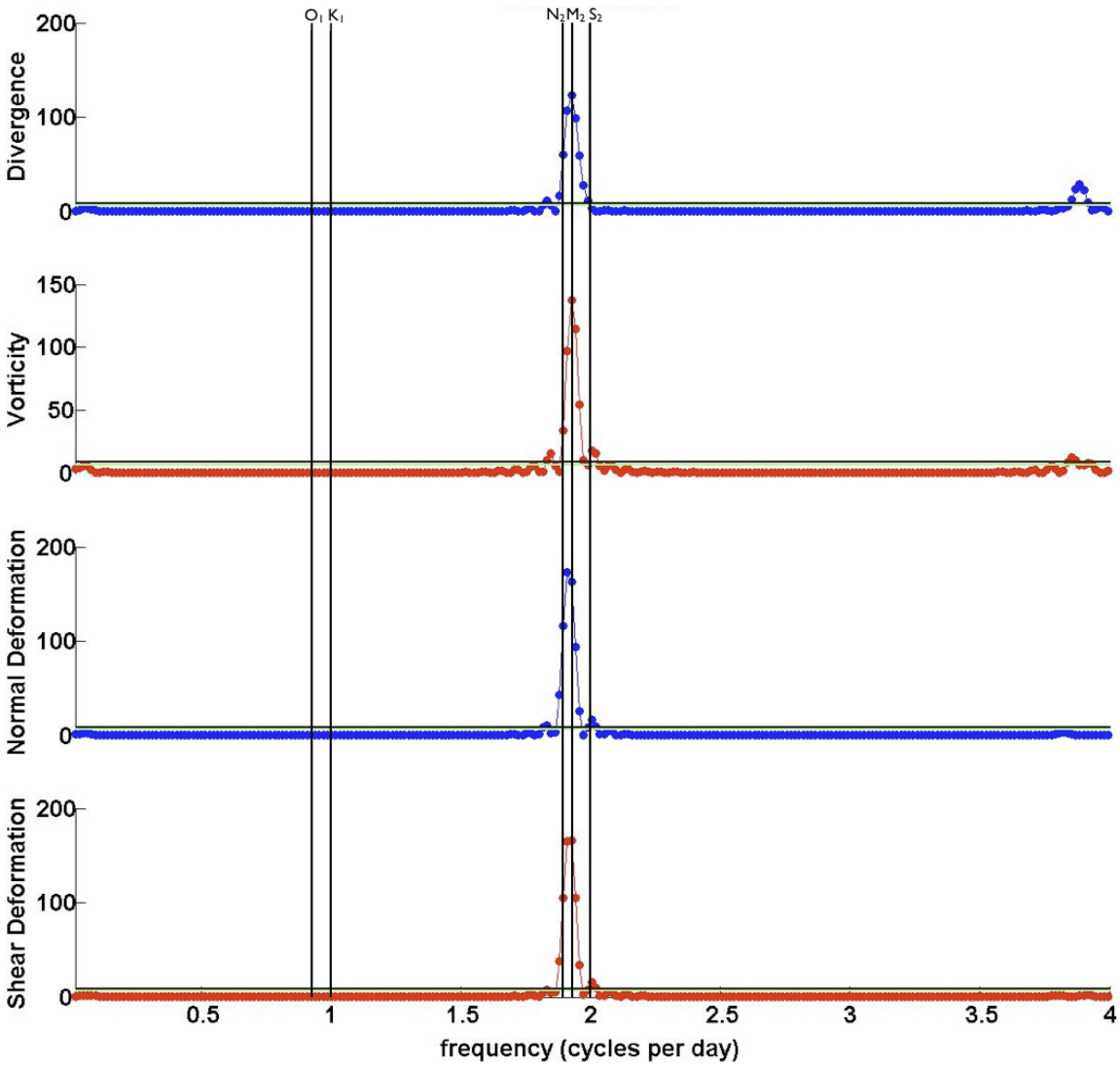

Figure 5.26: Power spectra plots of divergence, vorticity, normal deformation, and shear deformation for a blob within a M2 tidal field. The black and green horizontal lines are the 95% and 50% confidence respectively. The black vertical lines are placed at the frequencies of the dominant tidal constituents.

Chapter 6

DISCUSSION

6.1 Summary and Conclusions

Previous studies of the Delaware Bay circulation suffered from a lack of synoptic observations. They were most often based on relatively short time series measurements from sparse arrays at fixed locations, or from hydrographic cruises of limited duration. The influence of near–surface winds on the circulation had to be inferred either from wind measurements on land or from meteorological buoys well removed from the bay mouth. Even with limited observations, existing studies have established the broad characteristics of the bay's surface circulation: an energetic M2 tide, a buoyant outflow plume seasonally modulated by freshwater inflow to the bay, and a detectable response to remote wind forcing. What is missing from this picture is a sense of the spatial variability at smaller scales (1-10 km) and a sense of the episodic nature of the flow, which responds to both wind events (typical periods of 3-10 days), changes in freshwater inflow (strong seasonal variability), and changing circulation on the adjacent shelf, which is poorly understood. Since historical descriptions of surface transport have been based largely on PVDs computed from velocities at a single mooring, the role of spatial varying currents on transport also has yet to be assessed. Here, synoptic surface current measurements and synoptic winds from a high resolution model are used to explore the spatial variability of the surface circulation over an eight–month period and to assess the role of this spatial variability in driving surface transport.

Synoptic hourly HF radar surface currents, available nearly continuously over the eight–month period, allowed us to map the spatial variability of the dominant M2 tides and the percent of the total surface velocity variance explained by tidal fits using the five most energetic constituents. Near the bay mouth, M2 tidal ellipses from the radar measurements were highly elliptical and oriented perpendicular to the bay mouth (see Figure 4.1). Moving offshore, the ellipses became smaller and more circular. These results agree very well both with analysis of historical point measurements (Münchow *et al.*, 1992) and with one numerical model study (Whitney and Garvine, 2008).

The synoptic study of the M2 tide fills in "gaps" in the M2 tide picture (based solely on historical point measurements) and validates one numerical model study with highly resolved synoptic velocities. The continuous eight–month record also allowed us to examine potential influences of stratification on the M2 tidal ellipses by comparing tidal fits from low and high outflow periods. Since the differences were negligible, we conclude that stratification effects on the circulation are minimal throughout most of the year.

Continuous synoptic velocities were also used to assess how much of the total velocity variance is explained by the tides. Figure 4.6 shows that, near the bay mouth, tidal fits using the five most energetic constituents explain 80-90% of the velocity variance. Moving offshore, this fraction drops to 50-60%. This analysis of velocity variance, however, ignores any spatial structure in the mean flow.

As noted above, there are no published direct comparisons of surface wind observations with surface currents in Delaware Bay. In prior studies, winds from land stations or a meteorological buoy located well outside the study area were used to establish a remote connection of winds on the surface circulation. Thus, very little is known about the spatial and temporal variability of surface winds and their relation to the circulation. We took a first step toward addressing this by correlating

model winds with radar surface currents to assess the low frequency response. As the WRF model is data assimilating, we view these winds as dynamic interpolations of observations.

Seasonally persistent winds were reported by Garvine (1985). However, during the transitional periods we analyzed; no persistent wind direction was found. While winds certainly influence surface circulation, all of the wind records we examined were dominated by frequent wind events lasting 3-5 days with no persistent wind direction (see Figures 4.9 and 4.10for examples). These highly variable wind conditions prohibit a simplified surface Ekman analysis that depends on steady winds. Consequently, we focused on one question. Is a low–frequency surface current response to changing winds detectable in synoptic records?

In conjunction with the surface current record, a high–resolution, nested wind model was used to explore the surface current response due to low–frequency winds. Maps of complex correlation between surface currents and model wind stress at 10 m (Figure 4.8) clearly show high correlation magnitudes (0.8 or higher) over most of the analysis region. Maps of mean veering angle (Figure 4.8) are less clear, with surface currents to the right of the winds only at the center of the analysis region. While these low–frequency correlation results indicate some relationship between wind stress and surface currents, they are not rigorous evidence for wind–driven flow. A complicating factor in this assessment is the presence of the outflow plume. As shown in figure 4.8 the complex correlation between the surface currents and the wind stress in the localized region of the outflow plume decreases from approximately 0.8 during the low outflow period to about 0.6 during the high outflow period. We conclude that wind events are not energetic or persistent enough to set up a detectable Ekman response.

Over the eight month tidal fit 90% of the the total velocity variance is due to the tides (see section 4.1.2). The remaining 10% of the velocity variance includes

contributions from wind driven and buoyancy flows. Since we expect these currents to be weak, when compared to maximum tidal velocities, it is perhaps not surprising that a consistent Ekman response was difficult to detect.

We computed mean surface velocities over two 45–day periods that contrast low and high freshwater outflow conditions. During both low and high outflows, two persistent low–frequency flow structures are apparent: the bay's energetic outflow plume at the southern bay mouth, and persistent, energetic cross–mouth flow toward the southwest. To our knowledge this is the first tangible documentation of this cross–mouth flow. Similar cross–mouth flows have not been widely reported before. Our results (Figure 4.7, 4.12, 4.13) clearly show that this is a persistent low–frequency flow feature, and it's structure is modulated to some extent by changing outflow conditions. Thus it is important to identify the responsible dynamics. To this end, it is obviously important to extend the radar coverage, both into the bay and along the shelf, to understand the spatial extent of this flow, and its connection with other nearshore currents.

The role of spatial variability on surface transport was assessed by comparing PVDs with trajectories. PVDs were found to be useful only over limited time scales (one day or less). The rapid separation of trajectories and PVDs indicate that spatial variability is critical when examining surface transport at the bay mouth. Those who are interested in transport related to ecological problems should be cautious. PVDs are of limited value in this region.

The results from section 5.4 show that even a small tidally driven domain such as Delaware Bay, can have residence times of three days or more. Average residence times during the month of September 2008 are 60 hours in certain areas of the domain. The analysis also shows that tides clearly influence the residence times, as well as escape fate and particle origin, which is expected since tides are the dominant forcing mechanism at the Bay mouth. The roles of winds and freshwater

outflow, and their influence on residence time, have yet to be determined. The phase of the tide as well as the particle's initialization location play the biggest role in determining a particle's residence, fate, and origin.

One limitation of the residence time results is that particles cannot reenter the domain. This is a general limitation of any analysis on a finite area domain. Here the M2 tides likely cause many particles to oscillate back and forth across the domain boundaries. Since we have no velocity information outside the domain we cannot track particles once they cross the domain boundary. The residence time results should therefore be treated as a lower bound. Of course, the residence time analysis shown here depend on the size and shape of the domain as well as the phase of the tide at the location of the particle's initialization.

Section 5.4 defines a time scale (λ^{-1}) for residence time in Delaware Bay that varies between 22 to 36 hrs from month to month. The fraction of particles remaining in the domain decreases exponentially with time. The rate of this decay is somewhat variable throughout the year. Similar laws govern a wide spectrum of physical processes, such as the decay of radioactive material and the transmittance of light as it travels through seawater.

The main advantage of blobs is that they help visualize the impact of deformation processes on a finite area of ocean. Single trajectories cannot depict the influence of deformation, whereas a blob can. Blobs also represent an acceptable surrogate for a dye patch, an oil spill, a harmful algal bloom, or a small group of larvae. At the Delaware Bay mouth, strong deformation processes were observed. This blob identification of deformation processes could have only been completed with the use of a synoptic current maps.

6.2 Future Questions

Finally, a new set of questions raised by our analysis:

1) *What is the origin of the cross–mouth flow?* The forcing mechanism responsible for the cross–mouth current will require further study, but it may be a part of the coastal current that travels southward along the New Jersey coast. This buoyancy driven current is represented by the large arrows near the coast in figure 6.1, taken from Epifanio and Garvine (2001). This low–frequency current may originate as part of a larger–scale feature on the New Jersey shelf, or it may be generated by tidal rectification at the bay mouth resulting from non–linear interactions with a complex coastline and bottom topography. A larger coverage area for HF radar could help answer this question.

2) *What causes observed differences between ADCP and radar currents?* In section 2, the spatial averaging areas for both the HF radar and an ADCP were addressed as the source of differences between the two instruments. This result explains 10–20% of the total RMS difference. There could be a bias in one or both of the instruments. Additional ADCP deployments, as well as drifter studies, can be used to examine this further.

3) *How do transport processes change with depth?* Carefully planned subsurface velocity measurements will be important to assess three–dimensional transport. Numerical models driven by realistic winds will also be helpful. Deeper understanding of the complex surface circulation at the Delaware Bay mouth, as well as many other coastal areas, requires analyses of long time series of synoptic surface winds and currents using tools like those employed here.

4) *How do winds and river outflow influence a particle's residence time?*

Section 5.4 showed how the particle residence time results can be influenced by the strong tidal forces at the bay mouth. It would be interesting to examine specific periods of high and low outflow, and winds, to determine their impact on residence time. Additionally, Lagrangian observations (drifter and dye experiments) at the bay mouth would be useful for validation of our simulated trajectories.

5) *How important are deformation processes on the evolving surface flow?* A number of interesting deformation processes were detected by the blob simulations presented here (Figures 5.19 and 5.21). These deformation processes will influence evolving harmful algal blooms or oil spills, as well as larval populations. Further studies using blobs for different time periods will help to gauge the robustness of this result.

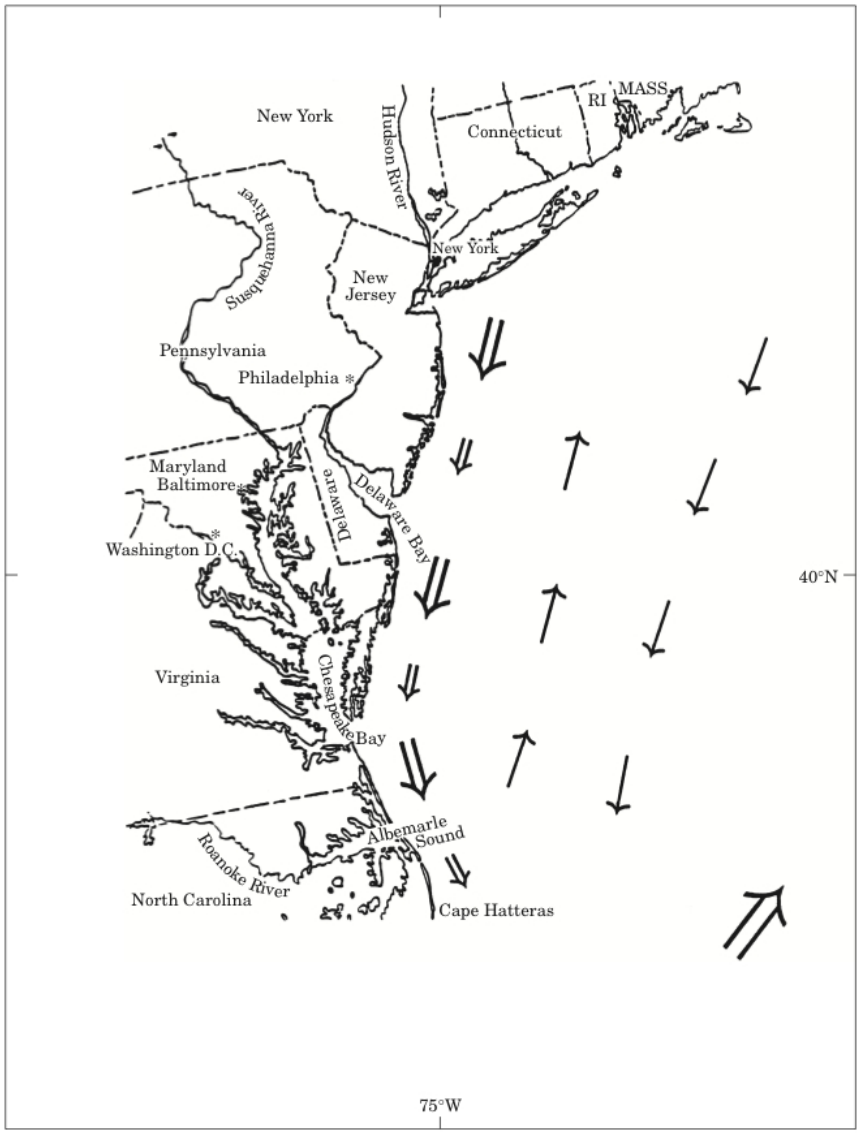

Figure 6.1: Map of the southern Middle Atlantic Bight showing mean surface flow field during late spring and summer. Southward arrows along the coast represent buoyancy–driven flow originating in Hudson, Delaware, and Chesapeake systems. Northward arrows on mid–shelf represent wind–driven flow associated with upwelling circulation. Southward arrows on outer shelf represent buoyancy–driven flow originating in Arctic regions well north of the Middle Atlantic Bight. North–eastward arrow off Cape Hatteras represents western boundary current, i.e., Gulf Stream. (Reprinted from Estuarine, Coastal and Shelf Science, 52, C. E. Epifanio, R. W. Garvine,Larval Transport on the Atlantic Continental Shelf of North America: a Review, 51-77, Copyright (2001), with permission from Elsevier)

BIBLIOGRAPHY

[1] R. Ahmadov, C. Gerbig, R. Kretschmer, S. Koerner, B. Neininger, A.J. Dolman, and C. Sarrat. Mesoscale covariance of transport and CO_2 fluxes: Evidence from observations and simulations using the WRF-VPRM coupled atmosphere–biosphere model. *J. Geophys. Res.*, 112:D22107, 2007.

[2] G. Avicola and P. Huq. Scaling analysis for the interaction between a buoyant coastal current and the continental shelf: Experiments and observations. *J. Phys. Oceanogr.*, 32(11):3233–3248, 2002.

[3] D. Barrick. *Geometrical Dilution of Statistical Accuracy (GDOSA) in Multi–Static HF Radar Networks*. CODAR Ocean Sensors, May 2002.

[4] E. Beckenbach and L. Washburn. Low-frequency waves in the Santa Barbara Channel observed by high-frequency radar. *J. Geophys. Res.*, 109:18, 2004.

[5] O. Ben-Tzvi, M. Kiflawi, H. Gildor, and A. Abelson. Possible effects of downwelling on the recruitment of coral reef fishes to the eilat (red sea) coral reefs. *Limnol. Oceanogr.*, 52:2618–2628, 2007.

[6] T. Berman, N. Paldor, and S. Brenner. Simulation of wind-driven circulation in the gulf of elat (aqaba). *J. Mar. Sys.*, 26:349–365, 2000.

[7] D. F. Carlson, P. A. Muscarella, H. Gildor, B. L. Lipphardt Jr., and E. Fredj. How useful are progressive vector diagrams for studying coastal ocean transport? *Limnol. Oceanogr.: Methods*, 8:98–106, 2010.

[8] R. D. Chapman and H. C. Graber. Validation of hf radar measurements. *Oceanography*, 10(2), 1997.

[9] R. D. Chapman, L. K. Shay, H. C. Graber, J. B. Edson, A. Karachintsev, C. L. Trump, and D. B. Ross. On the accuracy of HF radar surface current measurements: Intercomparisons with ship–based sensors. *J. Geophys. Res.*, 102:18737–18748, 1997.

[10] F. Chen and J. Dudhia. Coupling an advanced land surface-hydrology model with the Penn State-NCAR MM5 modeling system. Part I: Model implementation and sensitivity. *Mon. Weath. Rev.*, 129(4):569–585, 2001.

[11] C. Coulliette, F. Lekien, J. D. Paduan, G. Haller, and J. E. Marsden. Optimal pollution mitigation in Monterey Bay based on coastal radar data and nonlinear dynamics. *Environ. Sci. Technol.*, 41:6562–6572, 2007.

[12] L.S. Darby, S.A. Mckeen, C.J. Senff, A.B. White, R.M. Banta, M.J. Post, W.A. Brewer, R. Marchbanks, R.J. Alvarez, S.E. Peckham, H. Mao, and R. Talbot. Ozone differences between near-coastal and offshore sites in New England: Role of meteorology. *J. Geophys. Res.*, 112:D16S91, 2007.

[13] J. Dudhia. Numerical study of convection observed during the winter monsoon experiment using a mesoscale two–dimensional model. *J. Atmos. Sci.*, 46(20):3077–3107, 1989.

[14] J. A. Dutton. *The Ceaseless Wind*. McGraw-Hill, Inc., 1976.

[15] B. Efron and R. Tibshirani. Bootstrap methods for standard error, confidence intervals, and other measures of statistical accuracy. *Stat. Sci.*, 1:54–77, 1986.

[16] M.B. Ek, K.E. Mitchell, Y. Lin, E. Rogers, P. Grunmann, V. Koren, G. Gayno, and J.D. Tarpley. Implementation of Noah land–surface model advances in the National Centers for Environmental Prediction operational mesoscale Eta model. *J. Geophys. Res.*, 108:8851, 2003.

[17] W.J. Emery and R.E. Thomson. *Data analysis methods in physical oceanography*. Elsevier, 2nd edition, 2001.

[18] C. E. Epifanio and R. W. Garvine. Larval transport on the Atlantic continental shelf of North America: a review. *Estuarine, Coastal and Shelf Science*, 52:51–77, 2001.

[19] C. E. Epifanio, A. K. Masse, and R. W. Garvine. Transport of blue crab larvae by surface currents off Delaware Bay, USA. *Mar. Ecol. Prog. Ser.*, 54:35–41, 1989.

[20] J. Fiechter, B. K. Haus, N. Melo, and C. N. K. Mooers. Physical processes impacting passive particle dispersal in the Upper Florida Keys. *Cont. Shelf Res.*, 28:1261–1272, 2008.

[21] R. W. Garvine. A simple model of estuarine subtidal fluctuations forced by local and remote wind stress. *J. Geophys. Res.*, 90:1945–1948, 1985.

[22] R. W. Garvine. Subtidal frequency estuary-shelf interaction: Observations near Delaware Bay. *J. Geophys. Res.*, 96:7049–7064, 1991.

[23] H. Graber, D. R. Thompson, and R. E. Carande. Ocean surface features and currents measured with synthetic aperture radar interferometry and hf radar. *J. Geophys. Res.*, 101(C11), 1996.

[24] T.R. Holt, D. Niyogi, F. Chen, K. Manning, M.A. Lemone, and A. Qureshi. Effect of land–atmosphere interactions on the IHOP 24–25 may 2002 convection case. *Mon. Weath. Rev.*, 134(1):113–133, 2006.

[25] S. Y. Hong, Y. Noh, and J. Dudhia. A new vertical diffusion package with an explicit treatment of entrainment processes. *Mon. Weath. Rev.*, 134(9):2318 – 2341, 2006.

[26] C. P. Hughes and D. Veron. Impact of coastal development on the Delaware Bay sea breeze. In *Coastal Atmospheric/Ocean Processes and Urban Effects*, 2010.

[27] H. S. Huntley, B.L. Lipphardt Jr., and A.D. Kirwan Jr. Lagrangian predictability assessed in the East China Sea. *Ocean Modelling*, 2010.

[28] Teledyne RD Instruments. *Acoustic Doppler Current Profiler Principles of Operation: A Practical Primer*, p/n 951-6069-00 edition, 2006.

[29] Z. Janjic. The step-mountain eta coordinate model: Further developments of the convection, viscous sublayer, and turbulence closure schemes. *Mon. Weath. Rev.*, 1994.

[30] C. D. Janzen. *Wind forced dynamics of an estuary–shelf regime: Delaware Bay and the adjacent inner shelf.* Ph.D. dissertation, University of Delaware, 2000.

[31] P. Kabat, M. Claussen, P. A. Dirmeyer, J. H. C. Gash, L. Bravo de Guenni, M. Meybeck, R. A. Pielke Sr., C. J. Vorosmarty, R. W. A. Hutjes, and S. Lutkemeier, editors. *Vegetation, Water, Humans and the Climate*, pages 375–413. Springer, 2004.

[32] D. M. Kaplan and F. Lekien. Spatial interpolation and filtering of surface current data based on open–boundary modal analysis. *J. Geophys. Res.*, 112(C12007), 2007.

[33] A.D. Kirwan Jr. Velocity gradients. Kinematic parameters and blob evolution.

[34] N. P. Klingaman, J. Butke, D. J. Leathers, K. R. Brinson, and E. Nickl. Mesoscale simulations of the land surface effects of historical logging in a moist continental climate regime. *J. Applied Met. and Clim.*, 47(8):2166–2182, Aug 2008.

[35] J. T. Kohut, H. J. Roarty, and S. M. Glenn. Characterizing observed environmental variability with HF doppler radar surface current mappers and acoustic doppler current profilers: environmental variability in the coastal ocean. *Oceanic Engineering*, 31(4), 2006.

[36] P. K. Kundu. Ekman veering observed near the ocean bottom. *J. Phys. Oceanogr.*, 6:238–242, 1976.

[37] J. H. Kwun and S. H. You. Numerical study of sea winds simulated by the high-resolution Weather Research and Forecasting (WRF) model. *Asia-Pacific Journal of Atmospheric Sciences*, 45(4):523 – 554, 2009.

[38] F. Lekien, C. Coulliette, R. Bank, and J. Marsden. Open–boundary modal analysis: Interpolation, extrapolation, and filtering. *J. Geophys. Res.*, 109(C1), 2004.

[39] B.L. Lipphardt Jr., A.D. Kirwan Jr., and C.E. Grosch. Blending HF radar and model veocities in Monterey Bay. *J. Geophys. Res.*, 2000.

[40] B.L. Lipphardt Jr., D. Small, A.D. Kirwan Jr., S. Wiggins, K. Ide, C. E. Grosch, and J. D. Paduan. Synoptic Lagrangian maps: Application to surface transport in Monterey Bay. *J. Mar. Res.*, 64:221–247, 2006.

[41] R. D. McPherson. A numerical study of the effect of a coastal irregularity on the sea breeze. *Jour. Appl. Met.*, 9(5):767—777, 1970.

[42] E.J. Mlawer, S.J. Taubman, P.D. Brown, M.J. Iacono, and S.A. Clough. Radiative transfer for inhomogeneous atmospheres: RRTM, a validated correlated–k model for the longwave. *J. Geophys. Res. - Atmos.*, 102:16663–16682, 1997.

[43] A. Münchow. *The formation of a buoyancy driven coastal current.* Ph.D. dissertation, University of Delaware, 1992.

[44] A. Münchow and R. W. Garvine. Buoyancy and wind forcing of a coastal current. *J. Mar. Res.*, 51(2):293–322, 1993.

[45] A. Münchow, A. K. Masse, and R. W. Garvine. Astronomical and nonlinear tidal currents in a coupled estuary shelf system. *Cont. Shelf Res.*, 12:471–498, 1992.

[46] P. A. Muscarella, N. P. Barton, B. L. Lipphardt Jr., D. E. Veron, K.-C. Wong, and A. D. Kirwan Jr. Surface currents and winds at the Delaware Bay mouth. *Accepted for Cont. Shelf Res.*, 2011.

[47] G. Neumann. *Ocean Currents*, volume 4 of *Oceanography*. Elsevier Publishing Company, 335 Jan Van Galenstraat, P.O. box 211, Amsterdam, 1968.

[48] D.S. Nolan, C. Zhang, and S.H. Chen. Dynamics of the shallow meridional circulation around intertropical convergence zones. *J. Atmos. Sci.*, 64(7):2262–2285, 2007.

[49] A. S. Ogston, C. D. Storlazzi, M. E. Field, and M. K. Presto. Sediment resuspension and transport pattern on a fringing reef flat, molokai, hawaii. *Coral Reefs*, 23:559–569, 2004.

[50] Y. Ohashi and H. Kida. Local circulations developed in the vicinity of both coastal and inland urban areas: A numerical study with a mesoscale atmospheric model. *J. Applied Met.*, 41(1):30–45, 2002.

[51] C. Ohlmann, P. White, L. Washburn, E. Terrill, B. Emery, and M. Otero. Interpretation of coastal HF radar–derived surface currents with high–resolution drifter data. *Jour. Atmos. Ocean Tech.*, 24:666–680, 2007.

[52] J.D. Paduan and H. Graber. Introduction to high–frequency radar: Reality and myth. *Oceanography*, 10:36–39, 1997.

[53] J.D. Paduan, K.C. Kim, M.S. Cook, and F.P. Chavez. Calibration and validation of direction finding high frequency radar ocean surface current observations. *IEEE J. Oceanic Eng.*, 31(4), 2006.

[54] J.D. Paduan and L.K. Rosenfeld. Remotely sensed surface currents in Monterey Bay from shore–based HF radar (Coastal Ocean Dynamics Application Radar). *J. Geophys. Res.*, 101:20669–20686, 1996.

[55] H. L. Pan and L. Mahrt. Interaction between soil hydrology and boundary–layer development. *Bound. Layer Met.*, 38(1-2):185–202, 1987.

[56] E. H. Pape and R. W. Garvine. The subtidal circulation in Delaware Bay and adjacent shelf waters. *J. Geophys. Res.*, 87:7955–7970, 1982.

[57] R. Pawlowicz, B. Beardsley, and S. Lentz. Classical tidal harmonic analysis including error estimates in MATLAB using T_TIDE. *Computers and Geosci.*, 28:929–937, 2002.

[58] R.A. Pielke. Influence of the spatial distribution of vegetation and soils on the prediction of cumulus convective rainfall. *Rev. of Geophys.*, 39(2):151–177, 2001.

[59] T.M. Sanders and R.W. Garvine. Fresh water delivery to the continental shelf and subsequent mixing: An observational study. *J. Geophys. Res.*, 106(C11):27087–27101, 2001.

[60] L.K. Shay, T.M. Cook, Z.R. Hallock, B.K. Haus, H. Graber, and J. Martinez. The strength of the M_2 tide at the Chesapeake Bay mouth. *J. Phys. Oceanogr.*, 31:427–449, 2001.

[61] W. C. Skamarock, J. B. Klemp, J. Dudhai, D. O. Gill, D. M. Barker, W. Wang, and J. G. Powers. A description of the Advanced Research WRF Version 2. $http://www.mmm.ucar.edu/wrf/users/docs/arw_v2.pdf$, 2007.

[62] A. Skarke, B. L. Lipphardt Jr., P. Muscarella, K.-C. Wong, A. Trembanis, and M. Badiey. Comparison of HF radar and ADCP surface currents at the Delaware Bay mouth. In *Proceedings of the IEEE/OES/CMTC Ninth Working Conference on Current Measurement Technology*, 2008.

[63] W. T. Thompson, T. Holt, and J. Pullen. Investigation of a sea breeze front in an urban environments. *Quart. Jour. of the Royal Met. Soc.*, 133(624):579–594, 2007.

[64] M. Tomczak. Advanced exercises in physical oceanography.

[65] C. Truesdell. *The Kinematics of Vorticity.* Science Series No. 19. Indiana University Press, 1954.

[66] W Wang, D. Barker, J. Bray, C. Bruyere, M. Duda, J. Dudhia, Gill D., and Michalakes J. User's guide for Advanced Research WRF (ARW) modeling system version 2.2, 2007.

[67] M. M. Whitney. *Simulating the Delaware Coastal Current.* Ph.D. dissertation, University of Delaware, 2003.

[68] M. M. Whitney and R. W. Garvine. Simulating the Delaware Bay buoyant outflow: Comparison with observations. *J. Phys. Oceanogr.*, 36(1):3–21, 2006.

[69] M. M. Whitney and R. W. Garvine. Estimating tidal current amplitudes outside estuaries and characterizing the zone of estuarine tidal influence. *Cont. Shelf Res.*, 28(3):380–390, 2008.

[70] K.-C. Wong. The wind driven currents on the Middle Atlantic Bight inner shelf. *Cont. Shelf Res.*, 19(6):757–773, 1999.

[71] K.-C. Wong and J. E. Moses-Hall. The tidal and subtidal variations in the transverse salinity and current distributions across a coastal plain estuary. *J. Mar. Res.*, 56:489–517, 1998.

[72] K.-C. Wong and A. Münchow. Buoyancy forced interaction between estuary and inner shelf: observation. *Cont. Shelf Res.*, 15:59–88, 1995.

Appendix A

CALCULATING KINEMATIC QUANTITIES FOR EVOLVING BLOBS

A.1 Finite Difference Method

Finite differences are widely used to numerically approximate derivatives on a discrete grid. This method (figure A.1) uses the center of mass of the evolving blob as the center point for a plus sign finite difference stencil. Four surrounding points that are a distance of dy or dx away from the center of mass are used to compute the velocity gradients as finite differences:

$$\begin{aligned} \frac{\partial u}{\partial x} &= \frac{u_{i+1,j} - u_{i-1,j}}{2\Delta x}, \\ \frac{\partial u}{\partial y} &= \frac{u_{i,j+1} - u_{i,j-1}}{2\Delta y}, \\ \frac{\partial v}{\partial x} &= \frac{v_{i+1,j} - v_{i-1,j}}{2\Delta x}, \\ \frac{\partial v}{\partial y} &= \frac{v_{i,j+1} - v_{i,j-1}}{2\Delta y}. \end{aligned} \tag{A.1}$$

A.2 Loop Integral Method

An alternative method for computing mean velocity gradients over finite area polygons relies on numerical line integrals around the polygon perimeter. Perimeter and area are calculated as:

$$\text{Perimeter} = \oint \text{ds} \tag{A.2}$$

and

$$\text{Area} = \frac{1}{2}\oint(x\text{dy} - y\text{dx}). \tag{A.3}$$

Mean velocity gradients within the polygon are computed using contour integrals based on Greens theorem:

$$\begin{aligned}
\overline{\frac{\partial u}{\partial x}} &= \frac{\oint u\text{dy}}{\text{Area}}, \\
\overline{\frac{\partial u}{\partial y}} &= \frac{-\oint u\text{dx}}{\text{Area}}, \\
\overline{\frac{\partial v}{\partial x}} &= \frac{\oint v\text{dy}}{\text{Area}}, \\
\overline{\frac{\partial v}{\partial y}} &= \frac{-\oint u\text{dx}}{\text{Area}}.
\end{aligned} \tag{A.4}$$

It may be important to note that the finite difference method has truncation errors on the order of Δx^2, while the loop method uses a numerical integration also with errors of the same order. This implies that there should be no real difference in the accuracy between the two methods. Also, the finite difference method is essentially a special case of the loop method with the blob defined by four points at (i-1,j),(i+1,j),(i,j-1), and (i,j+1).

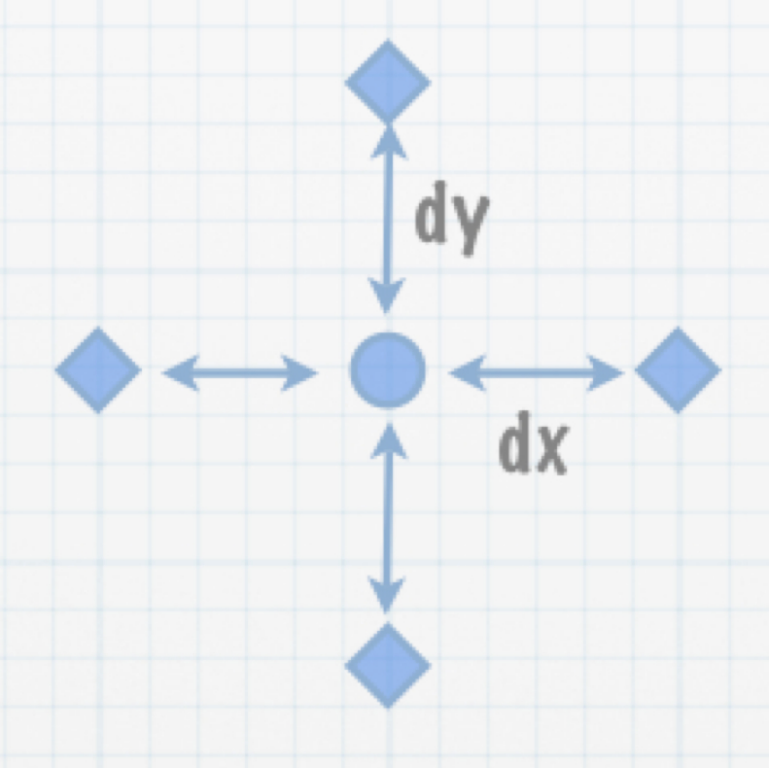

Figure A.1: Plus sign stencil

Appendix B

EXPLORING UNCERTAINNESS IN HF RADAR MEASUREMENTS USING SIMULATIONS WITH KNOWN FLOWS

There are number of known sources of uncertainty in HF radar measurements, as discussed in section 2.5.1. GDOP (section 2.5.1.1) is a natural consequence of the geometry associated with measuring surface currents using multiple radars. GDOP only degrades current measurements that include a source of error or uncertainty. All radial velocities measured by HF radars have inherent measurement uncertainties associated with them. In addition, spatial variability of ocean currents over the footprint of the averaging circles used for the radials to totals mapping (circles with 3 km radius for Delaware Bay) contributes an additional uncertainty source that is amplified by GDOP effects. This occurs because the least–squares mapping within each totals averaging circle assumes that the true current is constant over the entire circle and can be represented by a single vector at the circle's center.

The comparisons of HF radar with ADCPs at the Delaware Bay mouth (section 3.2) showed (u,v) RMS differences of 6–23 cm s^{-1} (see table 3.1). Two ADCPs were deployed at the same time, and separated by roughly 3.8 km. For these two ADCPs, RMS differences with HF radar were 6–14 cm s^{-1} (see table 3.1). When ADCPs B and C were compared with each other, RMS differences of 12.6 cm s^{-1} (u) and 23 cm s^{-1} (v) were found (see table). Since the ADCP vs. ADCP RMS statistics are similar to those for HF radar vs. ADCP, spatial variability of the

currents at scales of 3 km or smaller likely contribute to HF radar measurement uncertainties. We want to quantify the impact of this small scale spatial variability on HF radar measurements. We construct a simulator in Matlab to explore this, using known flows.

The simulator can be configured for any geographic region, using any number of radar sites. It can include Gaussian random noise added to the simulated measured radial velocities. It can also include random spatial gaps within each radar footprint. We will refer to this simulator as the "R2T Simulator".

Here, we configure the R2T Simulator for the geographic region at the Delaware Bay mouth using two radars located at the positions of the actual radars, as shown in Figure 2.2. The simulated radial measurement grids use an azimuthal spacing of five degrees and a range spacing of 1.5 km. These are the same grids used by the Cape May and Cape Henlopen radars. Figure B.1 shows the totals grid used for the simulations, with each grid point colored by the number of radial velocity measurements available within an averaging circle (3 km radius) centered at the grid point. The number of available radials are shown separately for each of the two radar sites.

Three known flows are examined (see figure B.2):

1) Steady, constant uniform flow - the simplest case of a constant known flow with no time dependence.

2) Steady, eddy flow - a simple, circular eddy centered outside the bay mouth with no time dependence.

3) M2 tidal flow - time dependent M2 tides computed from tide fits of actual HF radar measurements over an eight month period.

Note that the role of spatial variability (and its amplification through GDOP effects) can be assessed by comparing cases 2) vs. 1) and 3) vs. 1).

A conservative estimate of the lower bound on aggregated uncertainties for Delaware Bay measurements is made by considering the most energetic part of the flow (the M2 tide, case 3) including both random noise (added to the radial measurements) and spatial gaps (randomly inserted in the radial measurements for each radar at each hour).

B.1 The R2T Simulator

Figure B.3 shows the processing steps within the R2T Simulator. The R2T Simulator requires one input: a velocity field that can be accurately evaluated separately on an arbitrary number of polar coordinate grids that represent radial velocity measurement grids centered at the locations of each antenna. The known input velocity field can be specified analytically (as done in cases 1 and 2) or as a prescribed field on some input grid. If the input velocity is prescribed on a grid, it is linearly interpolated to the radial velocity measurement grid points for each antenna's grid.

The first step in the simulation is creating simulated measured radial velocities by evaluating or linearly interpolating the input known flow at each radial grid measurement point for each radar site, then projecting the velocities onto the radial look direction for each site respectively. Next, two options are available: one random noise can be added to each simulated radial velocity, and two spatial gaps can be inserted in the measured radials at each site by randomly deleting radials on each grid. For this study, the noise is specified as white ranging from -5 to 5 cm s^{-1}. Finally, simulated total velocities are computed on a total velocity grid using circles centered at each total velocity grid point. The radius of these circles is adjustable within the simulator, and is chosen to be 3 km for the simulations used here. This is the same circle radius used to process the Delaware Bay HF radar measurements described in section 2.5. All radials from all radar sites within the averaging circle are combined using unweighted least–squares to produce a single measurement of u and v velocity at the grid point (the circle's center). The R2T Simulator uses the

same least–squares mapping algorithm that is used to process the actual Delaware Bay HF radar measurements (using the CODAR software).

B.2 Results

The simplest example we examine is the uniform velocity field, which has no spatial variability and shows no difference between the known and simulated totals, which is expected. The main purpose for case one with no noise or gaps was to test the R2T Simulator. Figure B.4 shows the differences in magnitude and angle between the analytic and simulated totals. This example has the -5 to 5 cm s^{-}1 randomly varying white noise term included, which causes the GDOP errors to appear. The differences in the total vectors is more pronounced farther away from the radar sites.

Figure B.5 is the comparison with the known and simulated eddy velocity field. This, case two example, has no noise and no spatial gaps, but here we notice the introduction of the eddy's spatial variability has produced a max RMS error of 23 cm s^{-1} (see table B.1). This demonstrates how small variations in currents in space can be amplified by GDOP. Notice the largest differences occur in the regions of the domain with high GDOP. If the noise term and the spatial gaps were introduced into this example, the differences would increase in magnitude.

Figure B.6 shows the comparison for single time period for an M2 tidal current field. This example has the no noise term added and has no spatial gaps. The largest differences in this case are seen in the northern area of the domain (south of Cape May). This region is is known for rough topography and spatial current variability. Again, spatial variability is amplified by GDOP. Adding the noise term and the spatial gaps to this case will produce larger difference magnitudes.

Another important aspect of the M2 tidal flow is its time varying nature. Figure B.7 is the difference between the M2 fit totals and our simulated ones at

ADCP B deployment (see Figure 2.2). The bi–linear interpolation has been performed in space and time to put the M2 tidal data onto a radial grid at 10 minute time intervals. This example showing the time varying difference does not include noise or spatial gaps. Therefore, the difference in magnitude in figure B.7 is due solely to spatial variability. As the magnitude of the tidal currents increases, u difference values increase from 0.4 cm s^{-1} at slack tide and 2.1 cm s^{-1} at max flood and max ebb, and v difference values of cm s^{-1} at slack tide and 2.1 cm s^{-1} at max flood and max ebb. That is why we observe two complete cycles over this value over a 12 hour time period.

Due to the large amount of tunable parameters within the simulator it is practical to examine some of these statistics in a tabular format (Table B.1). The no noise uniform case produces no difference between the simulated and analytic vectors, which was stated earlier. The inclusion of a noise term in all of the cases will increase the observed differences in magnitude and angle. It is important to note that there are cases where the maximum difference in magnitude and angle can be quite large, yet the mean value is relatively low.

		Uniform		Eddy		M_2	
% missing		No noise	Noise	No noise	Noise	No noise	Noise
0%	$\|\vec{v}\|$	[0,0]	[2,14.2]	[5.2,23]	[5.6,26.7]	[1.1,12.1]	[2.1,12.0]
	Angle	[0,0]	[1.1,8]	[1.9,5.9]	[2.2,6.4]	[2,17.4]	[4.3,31.1]
20%	$\|\vec{v}\|$	[0,0]	[2.4,14.1]	[5.6,25.6]	[6,26.9]	[1.3,15.7]	[2.3,18.1]
	Angle	[0,0]	[1.4,10.1]	[2.9,15.3]	[5.7,17.4]	[2.4,22.7]	[4.7,30]

Table B.1: Table of HF radar simulator statistics. Values in the square brackets represent the [mean,max] (in cm s^{-1} for $|\vec{v}|$ and degrees for angle) over the entire grid. The tunable parameters are percent of data missing, flow type, and the optional inclusion of a noise term.

In conclusion, the R2T Simulations for the M2 tide can only account for approximately 2 cm $s^{-}1$ differences in (u,v) at the ADCP location. The remaining differences must come from spatial variability of the residual currents (remainder after the M2 tide is removed), or smaller scale variability not captured by the radial measurement grids, which have a range spacing of 1.5 km. Note that frame B vs. frame C comparisons in figure 3.7 indicate a large amount of spatial variability over 3.8 km that could explain the HF radar vs. ADCP difference we report here.

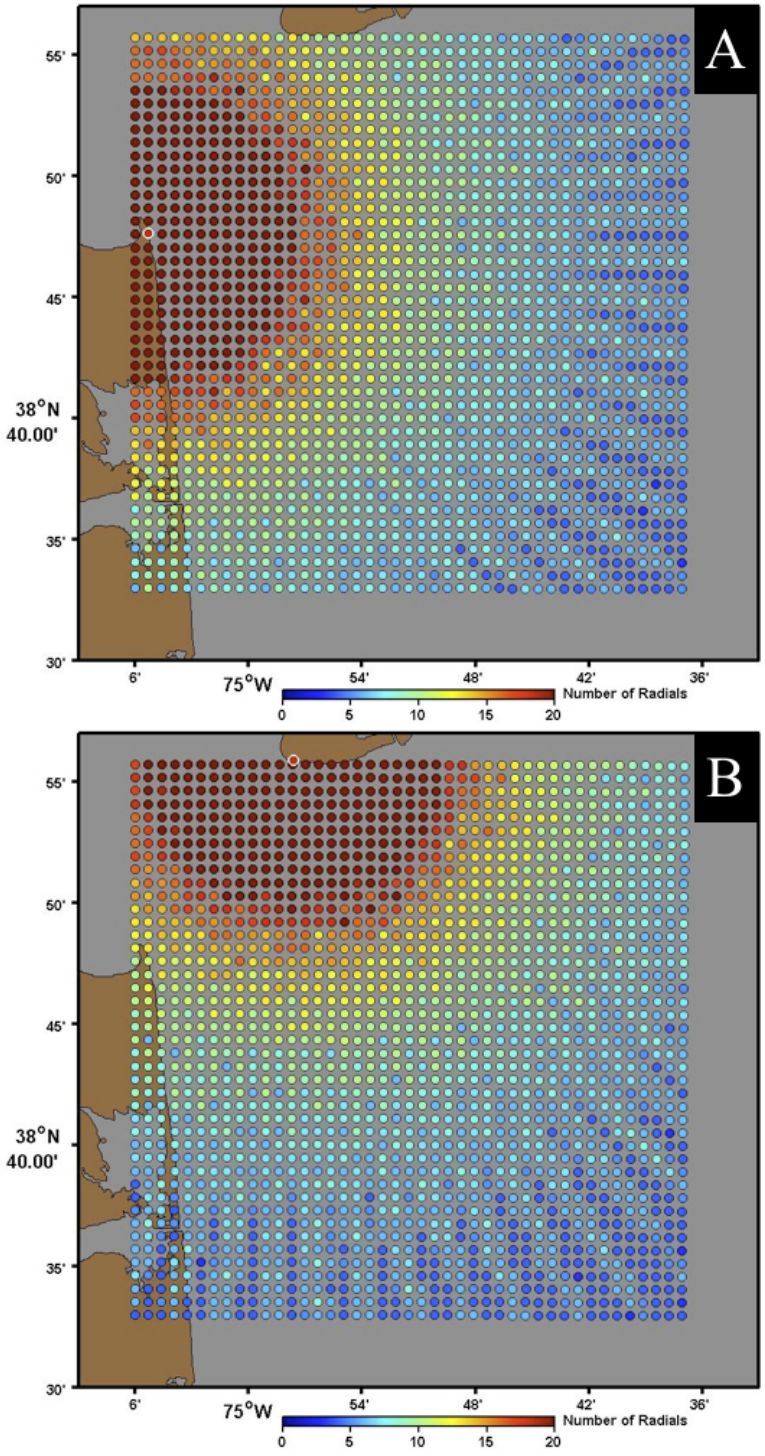

Figure B.1: Plot of totals grid with grid points colored by the number of radials present from Cape Henlopen (A) and Cape May (B). The minimum number of radials at any location from a single site is 3.

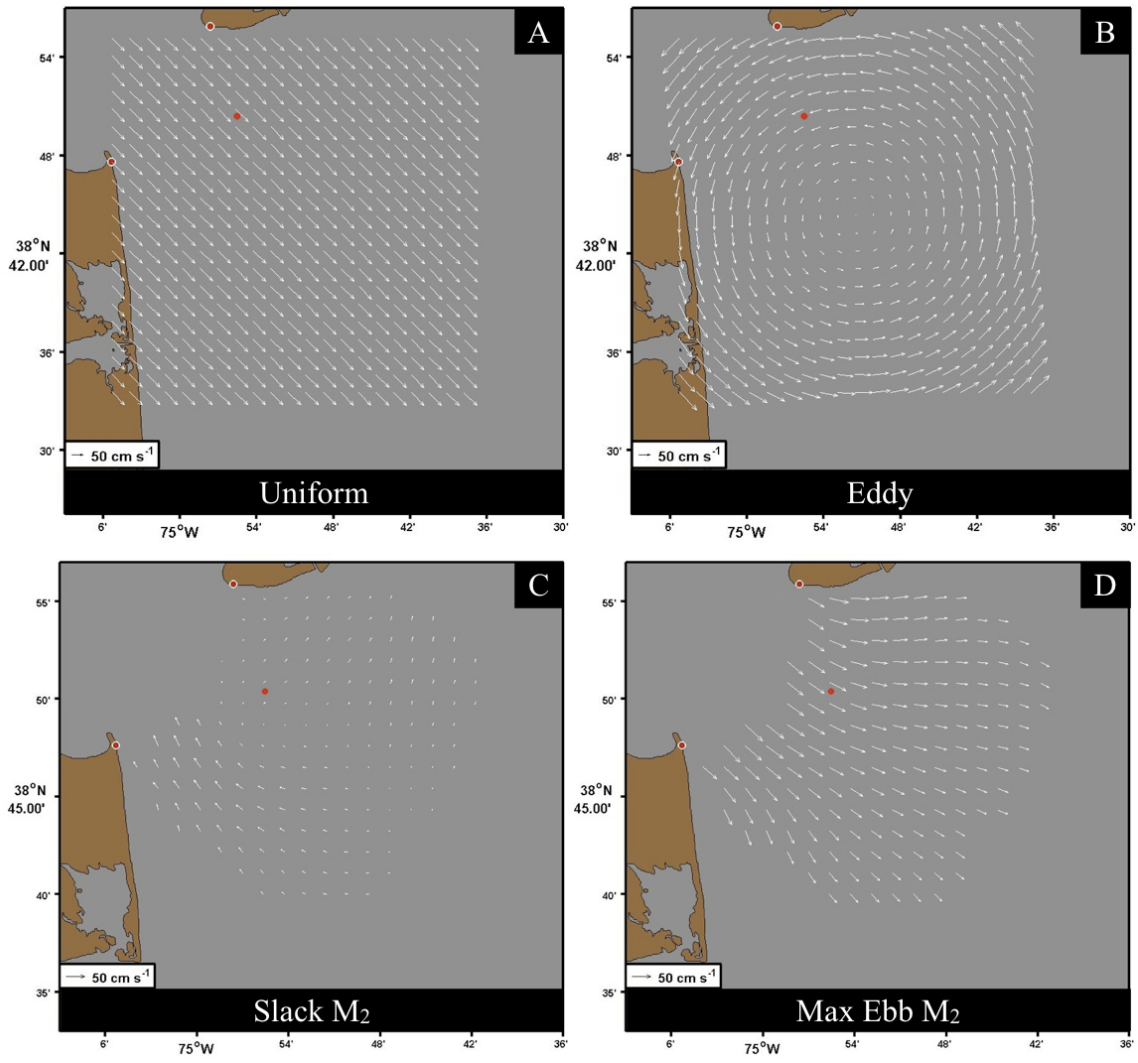

Figure B.2: (A) Uniform velocity field with all current vectors having a magnitude of 80 cm s^{-}1 and directed at 135 degrees clockwise from North. (B) Eddy velocity field. (C) Slack M2 tidal velocities from tidal fits to HF radar measurements. (D) Max ebb M2 tidal velocities from tidal fits to HF radar measurements.

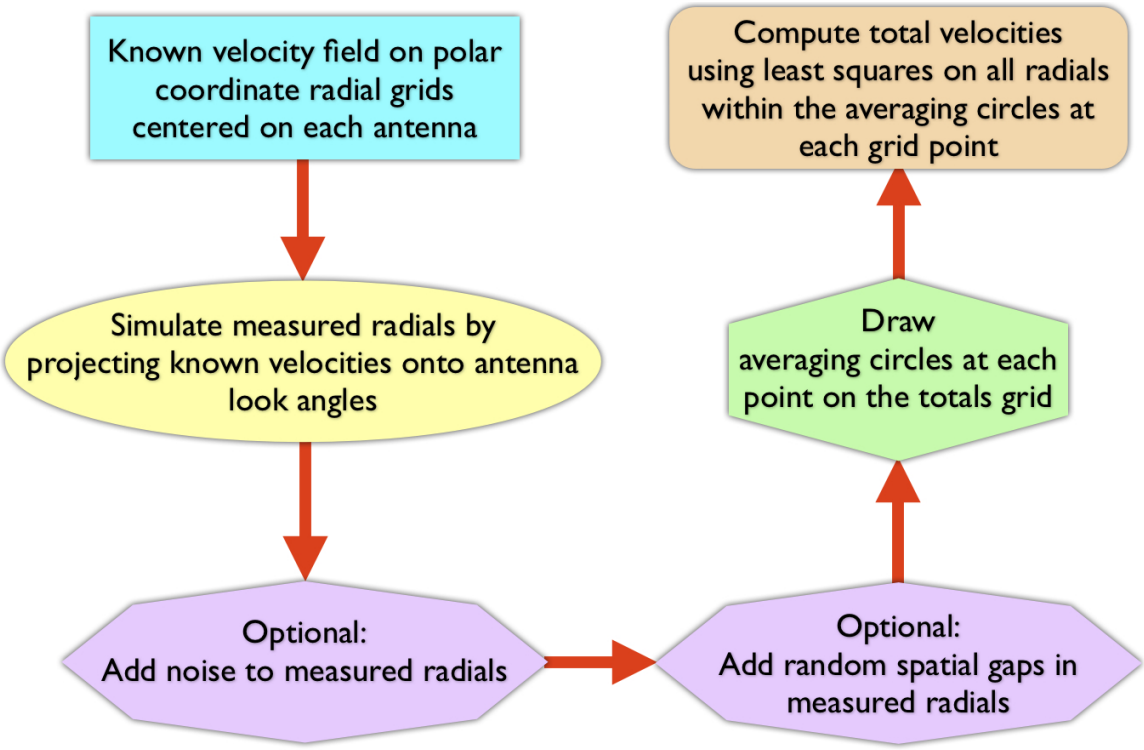

Figure B.3: Flow chart showing the processing steps within the HF radar simulator.

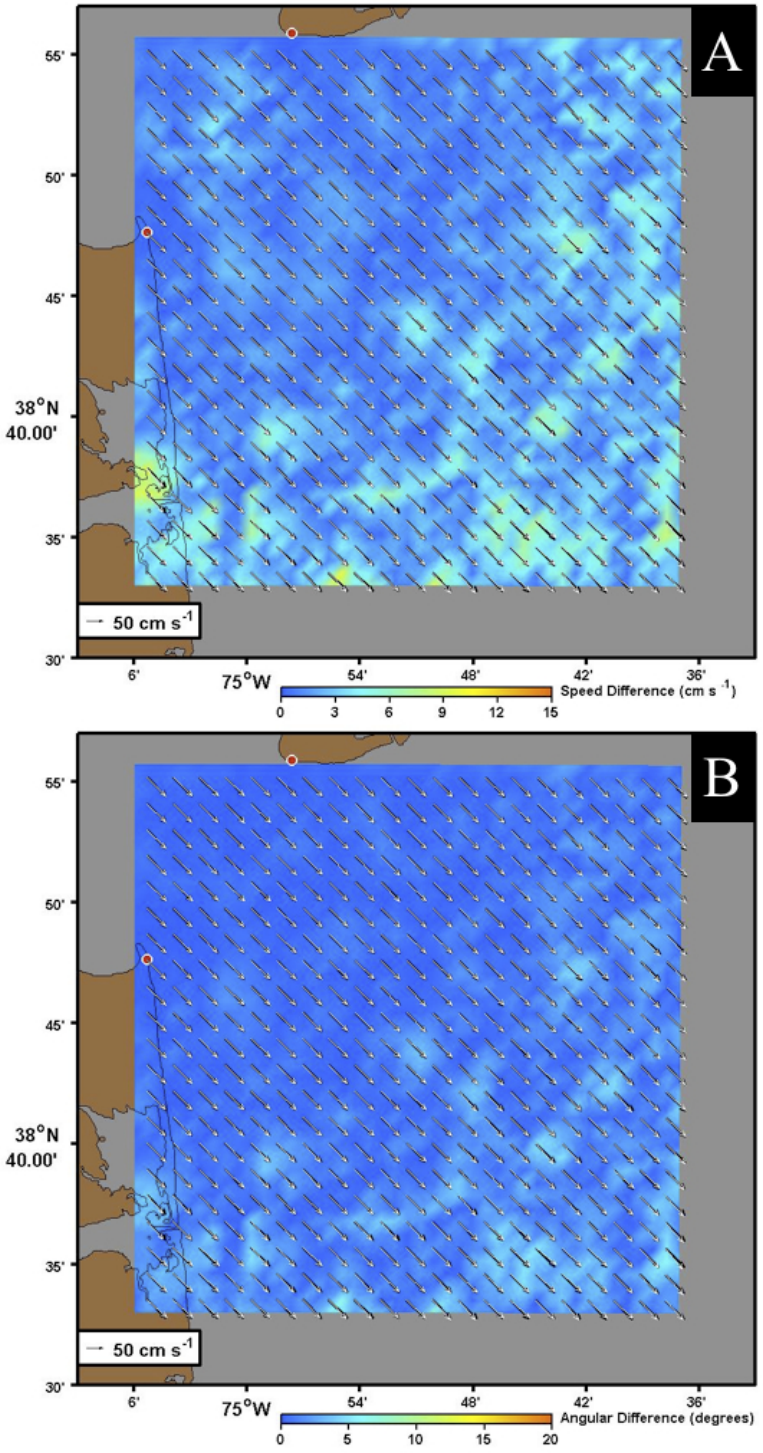

Figure B.4: Color contours of (A) velocity magnitude difference (in cm s⁻1), and (B) velocity direction difference (in degrees) for the steady, uniform flow case. The known (white) and simulated (black) total velocity vectors are also shown in each panel.

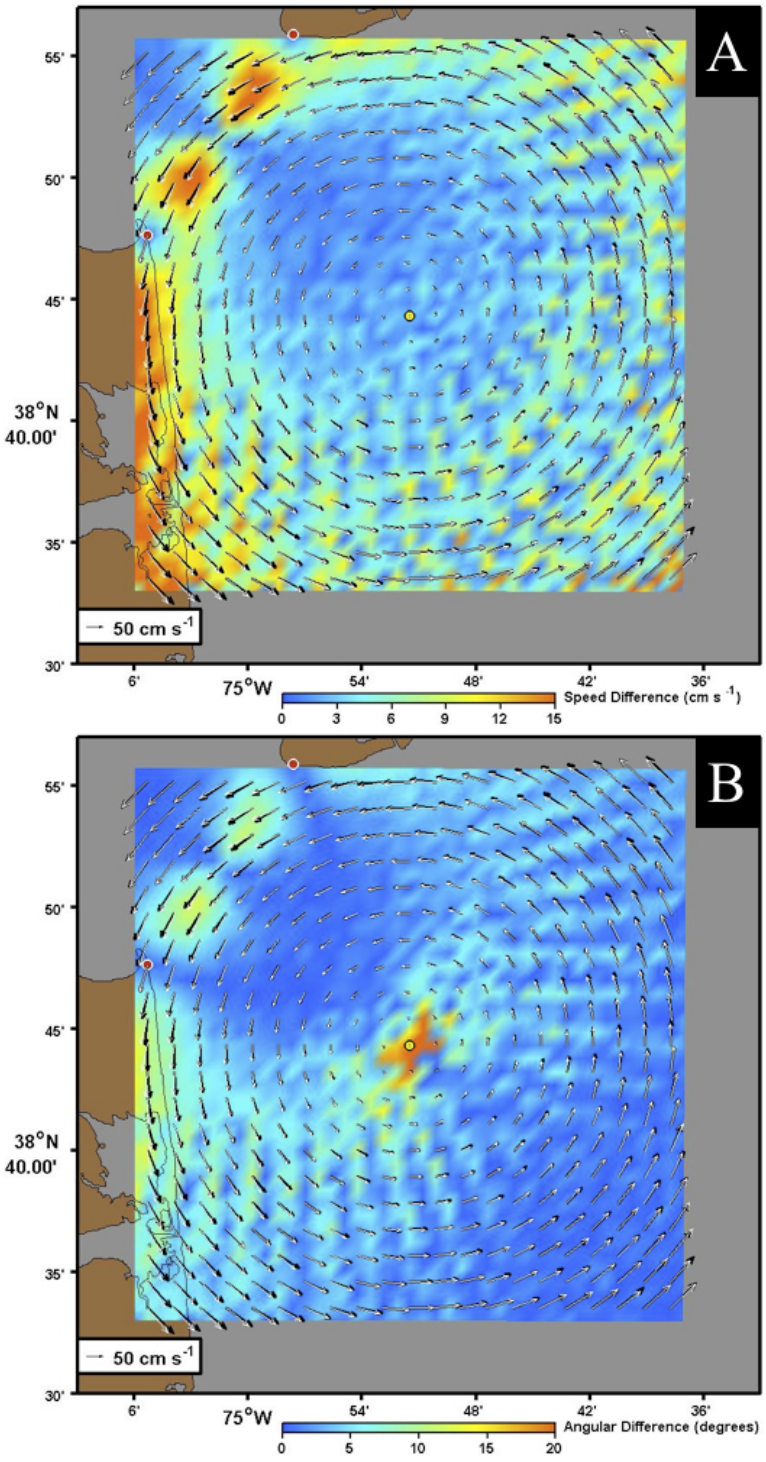

Figure B.5: Color contours of (A) velocity magnitude difference (in cm s^{-}1), and (B) velocity direction difference (in degrees) for the steady, eddy flow case. The known (white) and simulated (black) total velocity vectors are also shown in each panel.

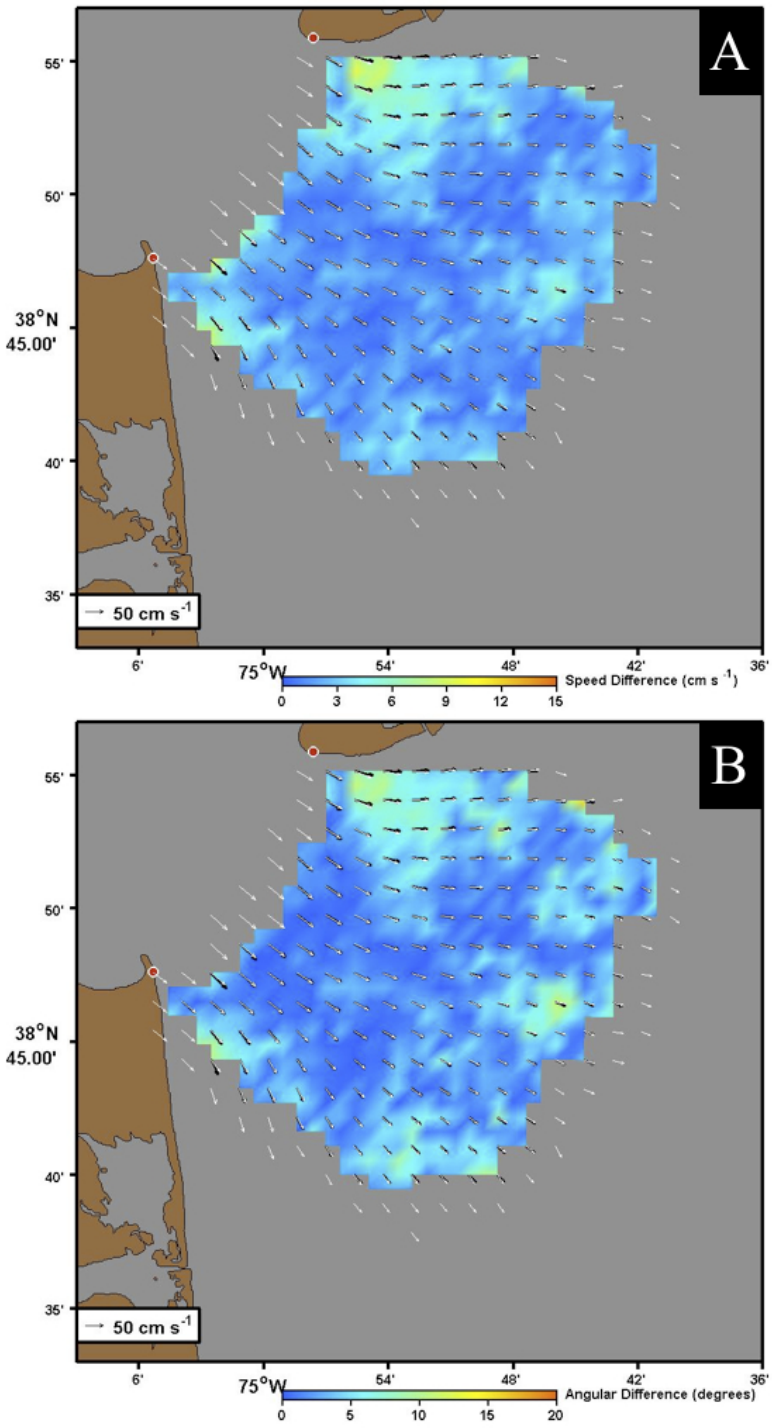

Figure B.6: Color contours of (A) velocity magnitude difference (in cm s^{-}1), and (B) velocity direction difference (in degrees) for the M2 tidal flow case. The known (white) and simulated (black) total velocity vectors are also shown in each panel.

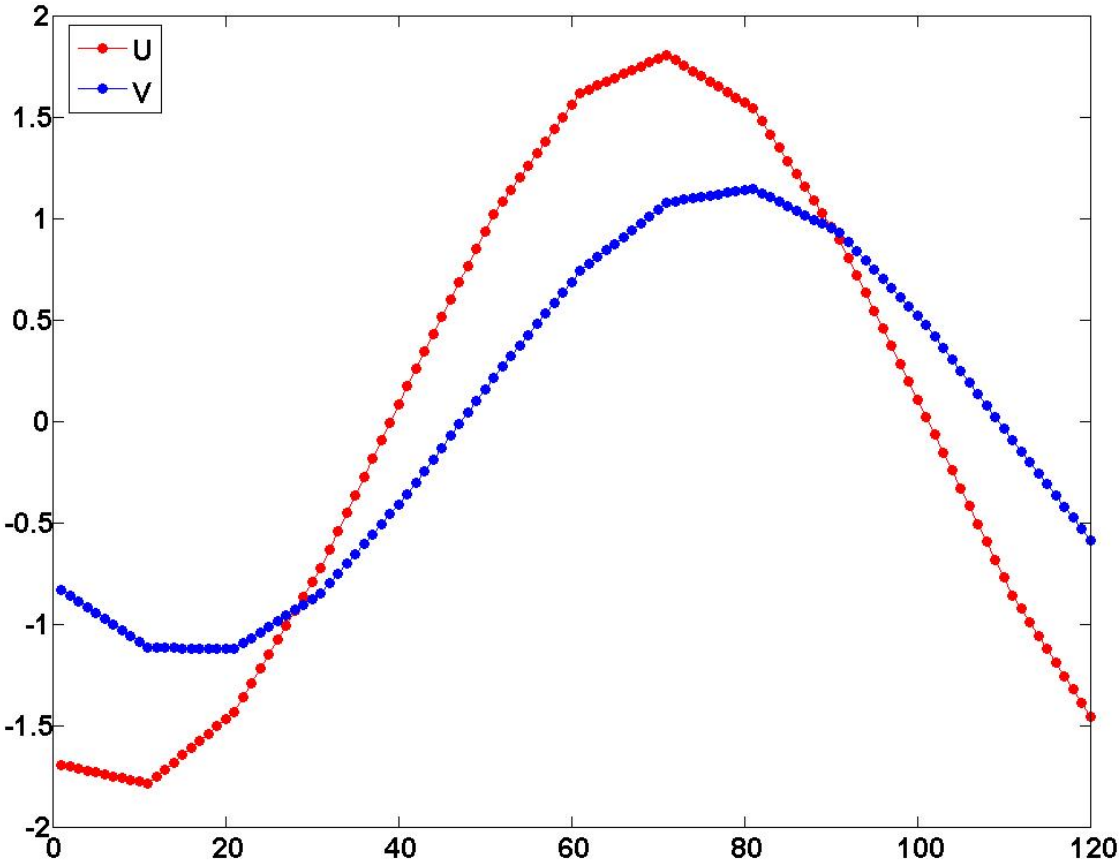

Figure B.7: U and V difference (known - simulated) of M2 tidal case at ADCP B deployment (Figure 2.2) over one tidal cycle. Y–axis is in cm $s^{-}1$ and x–axis is in 10 minute intervals.

Appendix C

LETTERS OF PERMISSION

ELSEVIER LICENSE
TERMS AND CONDITIONS

Apr 15, 2011

This is a License Agreement between Philip A Muscarella ("You") and Elsevier ("Elsevier") provided by Copyright Clearance Center ("CCC"). The license consists of your order details, the terms and conditions provided by Elsevier, and the payment terms and conditions.

All payments must be made in full to CCC. For payment instructions, please see information listed at the bottom of this form.

Supplier	Elsevier Limited The Boulevard,Langford Lane Kidlington,Oxford,OX5 1GB,UK
Registered Company Number	1982084
Customer name	Philip A Muscarella
Customer address	210 Robinson Hall Newark, DE 19716
License number	2650361227539
License date	Apr 15, 2011
Licensed content publisher	Elsevier
Licensed content publication	Estuarine, Coastal and Shelf Science
Licensed content title	Larval Transport on the Atlantic Continental Shelf of North America: a Review
Licensed content author	C. E. Epifanio, R. W. Garvine
Licensed content date	January 2001
Licensed content volume number	52
Licensed content issue number	1
Number of pages	27
Start Page	51
End Page	77
Type of Use	reuse in a thesis/dissertation
Portion	figures/tables/illustrations
Number of figures/tables/illustrations	1

Figure C.1: Letter of Permission for Dissertation Figure 6.1

Format	both print and electronic
Are you the author of this Elsevier article?	No
Will you be translating?	No
Order reference number	
Title of your thesis/dissertation	Circulation at the Delaware Bay Mouth from The Lagrangian and Eulerian Perspectives
Expected completion date	May 2011
Estimated size (number of pages)	175
Elsevier VAT number	GB 494 6272 12
Permissions price	0.00 USD
VAT/Local Sales Tax	0.0 USD / 0.0 GBP
Total	0.00 USD
Terms and Conditions	

INTRODUCTION

1. The publisher for this copyrighted material is Elsevier. By clicking "accept" in connection with completing this licensing transaction, you agree that the following terms and conditions apply to this transaction (along with the Billing and Payment terms and conditions established by Copyright Clearance Center, Inc. ("CCC"), at the time that you opened your Rightslink account and that are available at any time at http://myaccount.copyright.com).

GENERAL TERMS

2. Elsevier hereby grants you permission to reproduce the aforementioned material subject to the terms and conditions indicated.

3. Acknowledgement: If any part of the material to be used (for example, figures) has appeared in our publication with credit or acknowledgement to another source, permission must also be sought from that source. If such permission is not obtained then that material may not be included in your publication/copies. Suitable acknowledgement to the source must be made, either as a footnote or in a reference list at the end of your publication, as follows:

"Reprinted from Publication title, Vol /edition number, Author(s), Title of article / title of chapter, Pages No., Copyright (Year), with permission from Elsevier [OR APPLICABLE SOCIETY COPYRIGHT OWNER]." Also Lancet special credit - "Reprinted from The Lancet, Vol. number, Author(s), Title of article, Pages No., Copyright (Year), with permission from Elsevier."

4. Reproduction of this material is confined to the purpose and/or media for which permission is hereby given.

Figure C.1: continued

5. Altering/Modifying Material: Not Permitted. However figures and illustrations may be altered/adapted minimally to serve your work. Any other abbreviations, additions, deletions and/or any other alterations shall be made only with prior written authorization of Elsevier Ltd. (Please contact Elsevier at permissions@elsevier.com)

6. If the permission fee for the requested use of our material is waived in this instance, please be advised that your future requests for Elsevier materials may attract a fee.

7. Reservation of Rights: Publisher reserves all rights not specifically granted in the combination of (i) the license details provided by you and accepted in the course of this licensing transaction, (ii) these terms and conditions and (iii) CCC's Billing and Payment terms and conditions.

8. License Contingent Upon Payment: While you may exercise the rights licensed immediately upon issuance of the license at the end of the licensing process for the transaction, provided that you have disclosed complete and accurate details of your proposed use, no license is finally effective unless and until full payment is received from you (either by publisher or by CCC) as provided in CCC's Billing and Payment terms and conditions. If full payment is not received on a timely basis, then any license preliminarily granted shall be deemed automatically revoked and shall be void as if never granted. Further, in the event that you breach any of these terms and conditions or any of CCC's Billing and Payment terms and conditions, the license is automatically revoked and shall be void as if never granted. Use of materials as described in a revoked license, as well as any use of the materials beyond the scope of an unrevoked license, may constitute copyright infringement and publisher reserves the right to take any and all action to protect its copyright in the materials.

9. Warranties: Publisher makes no representations or warranties with respect to the licensed material.

10. Indemnity: You hereby indemnify and agree to hold harmless publisher and CCC, and their respective officers, directors, employees and agents, from and against any and all claims arising out of your use of the licensed material other than as specifically authorized pursuant to this license.

11. No Transfer of License: This license is personal to you and may not be sublicensed, assigned, or transferred by you to any other person without publisher's written permission.

12. No Amendment Except in Writing: This license may not be amended except in a writing signed by both parties (or, in the case of publisher, by CCC on publisher's behalf).

13. Objection to Contrary Terms: Publisher hereby objects to any terms contained in any purchase order, acknowledgment, check endorsement or other writing prepared by you, which terms are inconsistent with these terms and conditions or CCC's Billing and Payment terms and conditions. These terms and conditions, together with CCC's Billing and Payment terms and conditions (which are incorporated herein), comprise the entire agreement between you and publisher (and CCC) concerning this licensing transaction. In the event of any conflict between your obligations established by these terms and

Figure C.1: continued

conditions and those established by CCC's Billing and Payment terms and conditions, these terms and conditions shall control.

14. Revocation: Elsevier or Copyright Clearance Center may deny the permissions described in this License at their sole discretion, for any reason or no reason, with a full refund payable to you. Notice of such denial will be made using the contact information provided by you. Failure to receive such notice will not alter or invalidate the denial. In no event will Elsevier or Copyright Clearance Center be responsible or liable for any costs, expenses or damage incurred by you as a result of a denial of your permission request, other than a refund of the amount(s) paid by you to Elsevier and/or Copyright Clearance Center for denied permissions.

LIMITED LICENSE

The following terms and conditions apply only to specific license types:

15. **Translation**: This permission is granted for non-exclusive world **English** rights only unless your license was granted for translation rights. If you licensed translation rights you may only translate this content into the languages you requested. A professional translator must perform all translations and reproduce the content word for word preserving the integrity of the article. If this license is to re-use 1 or 2 figures then permission is granted for non-exclusive world rights in all languages.

16. **Website**: The following terms and conditions apply to electronic reserve and author websites:
Electronic reserve: If licensed material is to be posted to website, the web site is to be password-protected and made available only to bona fide students registered on a relevant course if:
This license was made in connection with a course,
This permission is granted for 1 year only. You may obtain a license for future website posting,
All content posted to the web site must maintain the copyright information line on the bottom of each image,
A hyper-text must be included to the Homepage of the journal from which you are licensing at http://www.sciencedirect.com/science/journal/xxxxx or the Elsevier homepage for books at http://www.elsevier.com , and
Central Storage: This license does not include permission for a scanned version of the material to be stored in a central repository such as that provided by Heron/XanEdu.

17. **Author website** for journals with the following additional clauses:

All content posted to the web site must maintain the copyright information line on the bottom of each image, and
he permission granted is limited to the personal version of your paper. You are not allowed to download and post the published electronic version of your article (whether PDF or HTML, proof or final version), nor may you scan the printed edition to create an electronic version,
A hyper-text must be included to the Homepage of the journal from which you are

Figure C.1: continued

licensing at http://www.sciencedirect.com/science/journal/xxxxx , As part of our normal production process, you will receive an e-mail notice when your article appears on Elsevier's online service ScienceDirect (www.sciencedirect.com). That e-mail will include the article's Digital Object Identifier (DOI). This number provides the electronic link to the published article and should be included in the posting of your personal version. We ask that you wait until you receive this e-mail and have the DOI to do any posting.
Central Storage: This license does not include permission for a scanned version of the material to be stored in a central repository such as that provided by Heron/XanEdu.

18. **Author website** for books with the following additional clauses:
Authors are permitted to place a brief summary of their work online only.
A hyper-text must be included to the Elsevier homepage at http://www.elsevier.com

All content posted to the web site must maintain the copyright information line on the bottom of each image
You are not allowed to download and post the published electronic version of your chapter, nor may you scan the printed edition to create an electronic version.
Central Storage: This license does not include permission for a scanned version of the material to be stored in a central repository such as that provided by Heron/XanEdu.

19. **Website** (regular and for author): A hyper-text must be included to the Homepage of the journal from which you are licensing at http://www.sciencedirect.com/science/journal/xxxxx. or for books to the Elsevier homepage at http://www.elsevier.com

20. **Thesis/Dissertation**: If your license is for use in a thesis/dissertation your thesis may be submitted to your institution in either print or electronic form. Should your thesis be published commercially, please reapply for permission. These requirements include permission for the Library and Archives of Canada to supply single copies, on demand, of the complete thesis and include permission for UMI to supply single copies, on demand, of the complete thesis. Should your thesis be published commercially, please reapply for permission.

21. **Other Conditions**:

v1.6

Gratis licenses (referencing $0 in the Total field) are free. Please retain this printable license for your reference. No payment is required.

If you would like to pay for this license now, please remit this license along with your payment made payable to "COPYRIGHT CLEARANCE CENTER" otherwise you will be invoiced within 48 hours of the license date. Payment should be in the form of a check or money order referencing your account number and this invoice number RLNK10970664.
Once you receive your invoice for this order, you may pay your invoice by credit card.

Figure C.1: continued

Please follow instructions provided at that time.

Make Payment To:
Copyright Clearance Center
Dept 001
P.O. Box 843006
Boston, MA 02284-3006

For suggestions or comments regarding this order, contact Rightslink Customer Support: customercare@copyright.com or +1-877-622-5543 (toll free in the US) or +1-978-646-2777.

Figure C.1: continued

From: Jo Davis <jdavis@sgmeet.com>
Subject: **ASLO Copyright Permission**
Date: April 15, 2011 4:49:33 PM EDT
To: pmuskee@UDel.Edu

To: Dr. Philip A Muscarella,

On behalf of the American Society of Limnology and Oceanography, we are happy to grant permission to use the figures from Limnology & Oceanography per your application below.

When reproducing the article/figure(s), please cite according to the references that follow:

All copyrighted works, whether displayed electronically or in print, should be properly acknowledged as follows:

"Copyright (Year) by the American Society of Limnology and Oceanography, Inc."

Once permission is granted to use an article or any part thereof of a work from L&O, the full citation must include:
1. Name(s) of the author(s);
2. Journal title (Limnology & Oceanography or L&O)
3. Publication date
4. Volume number
5. Issue number
6. Chapter or article name
7. Pages on which the articles, data, and/ or figure(s) appear

For your records, the American Society of Limnology and Oceanography is a nonprofit organization. (Taxpayer I.D. Number: 38-1710020)

If you have additional requests or have any questions in regard to this request, you can contact me directly via e-mail at jdavis@sgmeet.com.

Sincerely,

Jo Davis

Figure C.2: Letter of Permission for Dissertation Figure 5.4